NiTi: An *In-Situ* Investigation of Sintering from Elemental Powders

By

Daniel Robert Andrew Cluff

Submitted in partial fulfilment of the requirements

for the degree of Doctor of Philosophy

at

Dalhousie University

Halifax, Nova Scotia

October 2016

TABLE OF CONTENTS

LIST OF TABLES

LIST OF FIGURES

ABSTRACT

Ni-Ti powder mixtures mixed to 49 at% Ni : 51 at% Ti were made from high purity Ti – fine Ni (HP mixture), low purity Ti – fine Ni (LP mixture) high purity coarse (RA) Ti – fine Ni (RA mixture) and high purity Ti – coarse Ni (CNi mixture). They were analyzed during sintering using *in-situ* differential scanning calorimetry, *in-situ* neutron diffraction and microscopy. The temperature traces from the neutron diffraction experiment were compared to DSC traces for temperature verification. A detailed description of the procedure for the Rietveld refinements of neutron diffraction patterns obtained *in-situ* during the reactive sintering is presented. The determination of accurate U_{iso} values and lattice parameters from separate experiments was found to be critical to the successful refinement of minority phases. The phase fractions determined from the two sintering runs on the LP mixture were found to be in excellent agreement, with an uncertainty estimated at +/- 0.016 wt%.

Reaction between the Ni and Ti is not significant until the oxide layer surrounding the Ti particles dissolves at 600 °C. In all but the CNi mixture $Ti_2Ni(O)$ forms from 600 to 700 °C. Ni_3Ti grows in this temperature range solely in the LP mixture. The α-Ti to β-Ti(Ni) phase transformation begins at the eutectoid temperature (765 °C) and ends as late as 880 °C in the CNi mixture. It is thought the LP mixture undergoes a higher rate of reaction due to the influence of impurities (O, Fe and Ni), with an earlier and a higher total Ni_3Ti formation than the HP mixture during solid state sintering. The RA and CNi mixtures undergo TE-SHS commencing at or above 942 °C. Both DSC and in-situ neutron diffraction showed slower diffusion in the CNi mixture than in the RA mixture, resulting in a larger TE-SHS peak and specimens that slumped. During TE-SHS elemental Ti and Ni disappeared, with a corresponding surge in the fractions of all three intermetallic phases in the RA mixture, while in the CNi mixture Ni_3Ti disappeared. From 1100 to 1200 °C, the microstructure in all four mixtures became a stable mixture of NiTi with a small fraction of $Ti_2Ni(O)$.

Refinement of the O concentration in $Ti_2Ni(O)$ during sintering provided an understanding of the persistence of $Ti_2Ni(O)$. During the initial stages of sintering, $Ti_2Ni(O)$ with little or no O is formed. As the amount of this phase increases, its absolute O content also increases. In the later stages of sintering the absolute O content in $Ti_2Ni(O)$ remains the same even while $Ti_2Ni(O)$ decreases in phases fraction (consumed by NiTi), thus increasing the concentration of O in $Ti_2Ni(O)$. Oxygen raises the melting point of $Ti_2Ni(O)$ such that it is in equilibrium with NiTi at 1200 °C, despite a melting temperature of 984 °C for Ti_2Ni.

Also presented are lattice parameter values for all the phases in the Ni-Ti system as determined by Rietveld refinement on the *in-situ* neutron diffraction runs, including values for Ti_2Ni, Ni_3Ti and NiTi up 1200 °C. For the first time direct experimental evidence of the β-Ti(Ni)→Ti_2Ni + α-Ti eutectoid reaction is presented.

LIST OF ABBREVIATIONS AND SYMBOLS USED

SMA	Shape memory alloy
PM	Powder Metallurgy
DSC	Differential scanning calorimetry
XRD	X-ray diffraction
EDS	Energy dispersive spectroscopy
Ti	Titanium
TE-SHS	Thermal explosion mode of self-propagating high-temperature synthesis
Ni	Ni
β-Ti(Ni)	Body centered cubic titanium phase with Ni in solid solution
β-Ti	Body centered cubic titanium phase
α-Ti	Hexagonal close packed titanium phase
D_{50}	The median powder size of the cumulative powder size distribution
g	grams
ml	millilitres
$\rho_{relative}$	relative density
ND	Neutron diffraction
SEM	Scanning electron microscopy
PSD	Powder size distribution
MPa	Megapascal
°C	degrees Celsius
min	minutes
2-D	two dimension

Mo	Molybdenum
O	Oxygen
U_{iso}	atomic displacement parameter
R_{wp}	weighted profile R factor
B2	High temperature cubic phase of NiTi (austenite)
B19'	Low temperature monoclinic phase of NiTi (martensite)
wt%	weight percent
at%	atomic percent
Fe	Iron
A_s	Austenite start temperature
A_f	Austenite finish temperature
M_s	Martensite start temperature
M_f	Martensite finish temperature
B19	Low temperature phase of NiTi
Cu	Copper
V	Vanadium
SHS	Self-propagating high-temperature synthesis
PWP-SHS	Plane wave propagation mode of self-propagating high-temperature synthesis
SPS	Spark plasma sintering
HDH	Hydride-dehydride
Exo	exothermic
J	Joule
mW	milliwatt

λ	Wavelength
d	Interplanar spacing
θ	Bragg angle – angle of incidence of the probing beam on the crystal planes under consideration in diffraction
Å	Angstroms
CTE	Coefficient of thermal expansion
χ^2	Goodness of fit
γ	Face centered cubic iron phase
δ	High temperature body centered cubic iron phase
Al	Aluminum
Si	Silicon
QPA	Quantitative phase analysis
FE-SEM	Field emission scanning electron microscope
In	Indium
Sn	Tin
Zn	Zinc
Ag	Silver
Au	Gold
NRU	National research reactor
V	Vanadium
Mo	Molybdynum
T_{sample}	Sample temperature as measured by the thermocouple closest to the sample
$T_{control}$	Control temperature as measure by the furnace thermocouple
ΔT	T_{sample} - $T_{control}$

$\Delta T_{mixture}$	ΔT of a powder mixture
ΔT_{Mo}	ΔT of an empty molybdenum crucible
DT	Differential thermal
Ar	Argon
ICDD	International Centre for Diffraction Data
PDF	Powder diffraction file
GSAS	General Structure Analysis System – Rietveld software package
VESTA	Visualization for Electronic and Structural Analysis – software package
EXPGUI	Graphical user interface for GSAS
S_i	Rietveld scaling factor for the ith phase
w_i	Mass of the unit cell of the ith phase
a	Lattice parameter
c	Lattice parameter
s.u.	Standard uncertainty

ACKNOWLEDGEMENTS

CHAPTER 1

INTRODUCTION

1.1 INTRODUCTION

Shape memory alloys or smart materials are finding uses in ever increases markets. NiTi shape memory alloys (SMA) are among the most commonly used SMAs due to a good range of properties. It is corrosion resistant, biocompatible, shows good strain recovery and has high strength [1]. These properties have led to its adoption in a wide variety of industries. NiTi is used in the fashion industry as hingeless eyeglass frames and underwire in bras. Its use in the medical/dental industry includes both the use of tools (e.g. dental drill bits and *EndoFlex*^{TM} deflectable scissors by Surgical Innovations Ltd.) as well as stents and implants. Porous NiTi can be made to match the elastic modulus of bone to help prevent loosening between new bone growth and the implant [2]. Aerofit LLC. produces CryoFit NiTi couplings for joining aerospace tubing and recently NASA began flight testing a bendable wing using NiTi as the shape change material. NiTi has also been used in golf clubs, as actuators in the field of robotics and switches.

NiTi is however expensive to produce (typically vacuum induction melted and vacuum arc remelted) and difficult to machine [1] limiting the applications which use NiTi to ones with simple geometries. Powder metallurgy (PM) using elemental Ni and Ti powders could help reduce the costs through the production of near net shape parts (potentially complex geometries) and reduced material costs. It also allows for the production of functionally graded components (i.e. a location specific SMA response).

Blended elemental sintering occurs where pure Ni and Ti powders are mixed and reacted to form NiTi during sintering. While this has the potential for lower cost, the reactions during sintering are complex and not completely understood.

The present research focuses on producing shape memory NiTi intermetallic by way of sintering blended elemental Ni and Ti powders. In this chapter the Ni-Ti system is explored. This is followed by the concept of powder metallurgy, including powder production and press and sinter. This is followed by descriptions of the analytical techniques used in this investigation.

1.2   SHAPE MEMORY ALLOYS (SMA)

How SMA's work is not the focus of the present research, however the material being researched is an SMA. To that end what follows is a brief introduction to SMAs and how they work.

Shape memory alloys are metals which display the shape memory effect. This means that when loaded the metal deforms. Upon unloading, it maintains its deformed shape until a material dependent process is applied and the material recovers its original shape. Examples of this material dependent process are: application of heat for thermal SMAs [1] or application of a magnetic field for magnetic SMAs [3]. Materials which display the shape memory effect are capable of repeatedly recovering large deformations (up to 10%) [1,3]. Along with the shape memory effect, SMAs also typically display what is known as pseudo-elasticity. The behavior of a pseudo-elastic material is similar to

the shape memory effect except that the shape is recovered solely by unloading. Large recoverable deformations (up to 10%) can be obtained from pseudo-elastic materials.

What makes an SMA display either a shape memory effect or pseudo-elasticity is linked to the science behind the phenomena. A requisite for SMA behavior is that they produce a 'thermo-elastic' martensite [4]. This means that there is a reversible transformation between a high temperature, high symmetry (parent phase) and a low temperature, low symmetry phase (martensite) by either cooling (parent to martensite) or heating (martensite to parent) [4]. During cooling the transformation to lower crystal symmetries results in potentially large strains, however the martensite in SMAs is 'self-accommodating' [5]. In other words the large strains are accommodated by twinning, resulting in near zero volume change during the martensitic transformation. The twinned structure produces varying orientations of martensite, otherwise termed variants [1]. During loading the stress required to reorient or grow a martensite variant is less than that for slip or dislocation movement, implying no plastic deformation.

The difference between a material displaying a shape memory effect or pseudo elasticity is based on the phase present at operating temperatures. At temperatures where martensite is present the material shows a shape memory effect and the large recoverable strain is simply a reorientation of the variants. After unloading, the new orientation of the variants remain until the specimen is heated above the transformation tempreature, at which point the original orientation of the crystal lattice is returned due to lattice correspondence [1]. That is to say each martensite variant has a unique lattice transformation path when it returns to the parent phase allowing for shape recovery [1].

For a pseudo-elastic material the operating temperature is such that the parent phase is present. Under load the parent phase is destabilized and becomes what is known as 'stress induced martensite'. The parent phase transforms to martensite and a single martensite variant grows based on the loading direction. Thus it is the same mechanism that leads to recoverable strains for pseudo-elasticity as for the shape memory effect. Upon unloading the martensite returns to the parent phase.

Knowledge of the transformation temperature is important to ensure the desired behaviour (pseudo-elastic vs. pseudo-plastic) at operating temperatures. The transformation usually occurs over a range. Heating from the martensite phase the specimen begins to transform to austenite at what is termed the 'austenite start temperature' (A_s) and becomes fully austenite at the 'austenite finish temperature' (A_f). Similarly on cool down from the austenite phase, the martensitic phase transformation begins at the 'martensite start temperature' (M_s) with the material becoming fully martensitic at the 'martensite finish temperature' (M_f). Typically these temperatures are measured using a differential scanning calorimeter or electrical resistivity measurements. There is typically a hysterysis such that the M_s and M_f are below the A_f and A_s, respectively [6].

1.3 NI-TI SYSTEM

The Ni-Ti system produces three equilibrium intermetallic phases: Ti_2Ni, $NiTi$ and $TiNi_3$ (or Ni_3Ti). These phases are shown in the proceeding binary phase diagram (Figure 1-1) [7]. Other phases of interest in this investigation are α-Ti and β-Ti. In pure Ti the α-

Ti to β-Ti transition occurs at 882 ℃. With 5 at% Ni present this temperature drops and a Ti-rich eutectoid occurs at 765 ℃. The presence of Ni also lowers the melting point of β-Ti. At ~ 24 at% Ni and 942 ℃ there is a eutectic point. Heating past 942℃ the two phase region comprised of a solid solution of ~ 9 at% Ni in β-Ti and Ti₂Ni melts. At 984 ℃ a peritectic occurs resulting in Ti₂Ni → liquid + NiTi. The last point of interest is the NiTi – Ni₃Ti eutectic that occurs at 1118 ℃.
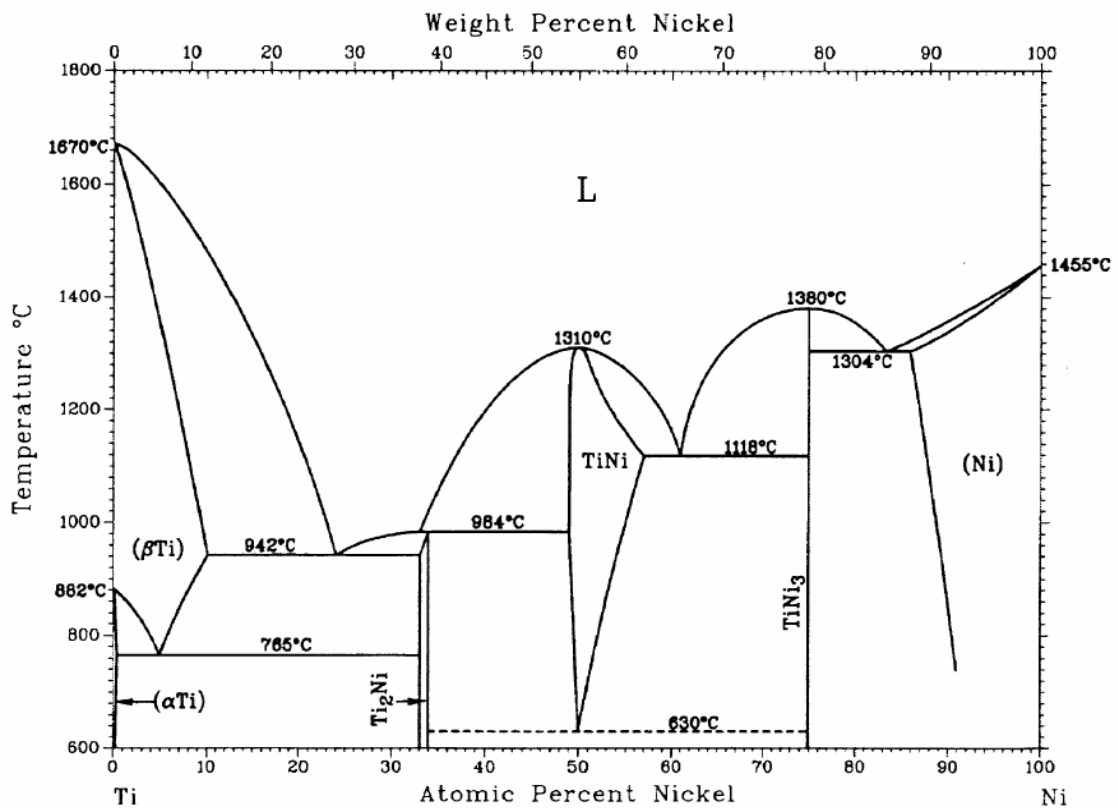
Figure 1-1   Ni-Ti binary phase diagram [7]

Figure 1-2 is a schematic of a potential phase progression in a 50 at% Ni Ni-Ti diffusion couple that is slowly heated to 1200 ℃ and held. It is intended to provide background into where and when the phases are expected to form. Initially the two species are pure (Figure 1-2 a)). As the temperature increases and diffusion of the two elements occurs,

5

the three equilibrium intermetallic phases set up at the interface. At the eutectoid temperature of 765 ℃ the α-Ti(Ni) – Ti$_2$Ni interface transforms to β-Ti(Ni). This transformation progresses inwards as the temperature increases and all of the α-Ti(Ni) has transformed to β-Ti(Ni) by 882 ℃. The β-Ti(Ni) - Ti$_2$Ni interface melts at 942 ℃. Note that this schematic assumes that the Ni content in β-Ti(Ni) approaches 9 at% Ni throughout the phase such that β-Ti(Ni) fully melts by 984 ℃. The liquid consumes more Ti$_2$Ni as the temperature is increased until 984 ℃. At 984 ℃ the last of the Ti$_2$Ni liquefies with a small amount becoming NiTi. The NiTi phase continues to grow at the expense of the liquid and Ni$_3$Ti. At 1118 ℃ the NiTi - Ni$_3$Ti interface melts. Eventually a homogeneous NiTi phase should form with a long enough hold time.
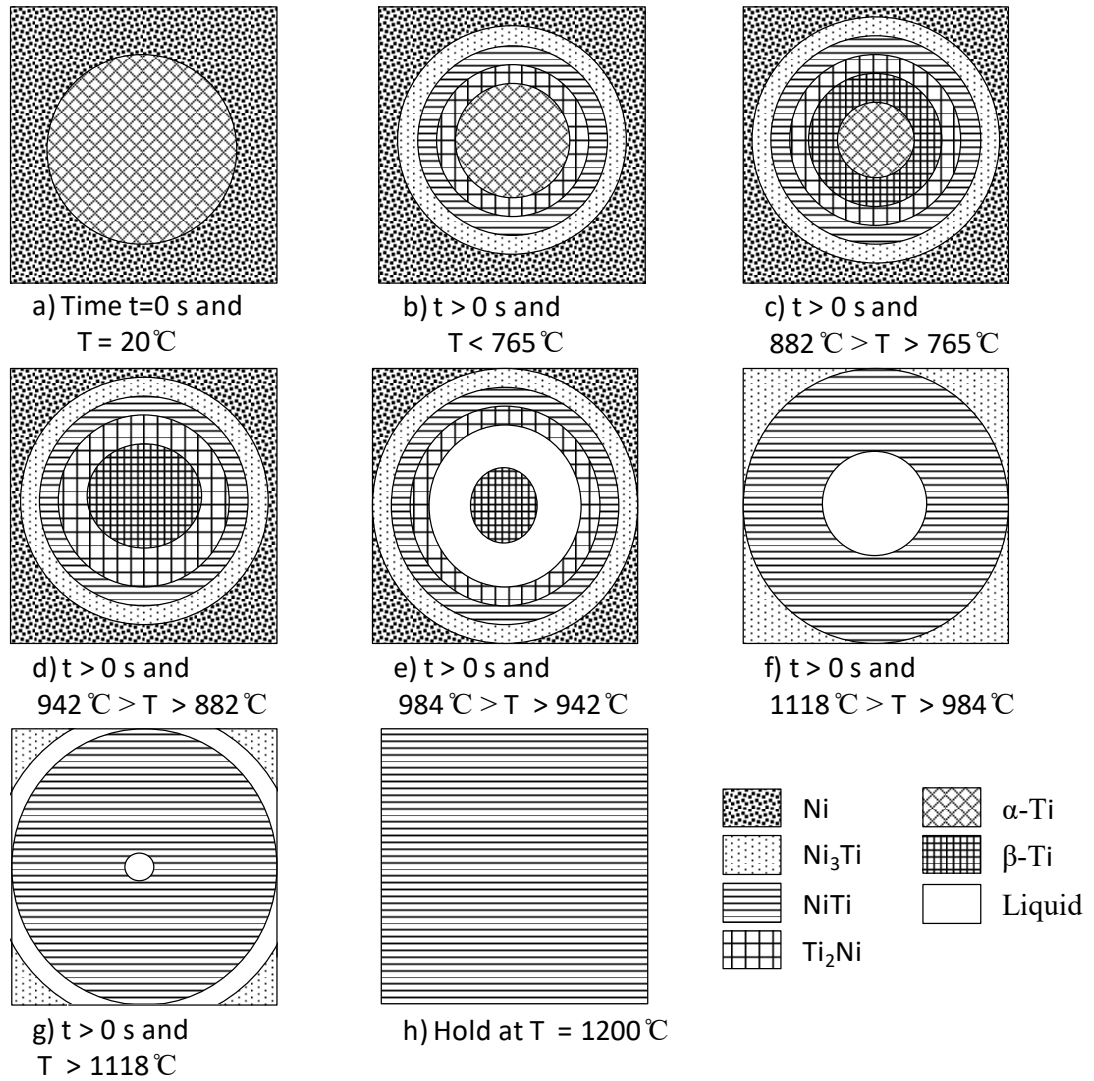
Figure 1-2   Phase progression schematic during heating to 1200 ℃ followed by a hold in an Ni-Ti diffusion couple.

In reality not all the above events take place exactly as outlined. Not all phases grow at the same rate and some may disappear sooner than noted above, altering the diffusion couple. For example if Ni_3Ti has been fully consumed by NiTi prior to 1118 °C the liquid associated with that eutectic will be not be present. It is also expected that liquid will migrate through capillary forces. What the schematic serves to highlight is that in a powder metallurgical system we expect the intermetallics to grow in layers at the

interfaces of the two elemental powders and if a eutectic or a eutectoid reaction takes place we know what phases were present.

Research into the rate of phase growth and diffusivities of Ni and Ti in the various phases has been conducted since the early '70s. Bastin and Rieck gained significant insight by studying various semi-infinite linear diffusion couples in the Ni-Ti system [8,9]. They investigated the growth of the intermetallic phases during holds at temperatures ranging from 650 to 940℃. Part one of their investigation [8] focused on the layer growth of the phases. The growth of β-Ti(Ni), Ti_2Ni and NiTi all showed growth that is diffusion controlled. Above 770℃ a very rapid growing layer of solid solution Ni in β-Ti(Ni) was observed. Enhanced diffusion by grain boundary diffusion at the α-Ti/β-Ti interface was found to occur up to 880℃ in the specimens using a lower purity Ti (99.5 wt% compared to 99.97 wt%). It was thought that the impurities at the grain boundaries stabilized the β phase. The growth rate for Ti_2Ni was found to be very slow in comparison to NiTi. Interestingly the growth rates of both Ti_2Ni and NiTi were lower when β-Ti was also present in the diffusion couple. Ni_3Ti was found to grow quickly at first but stabilized at a thickness of 20 μm. Above 800℃ its growth was independent of temperature.

From their data presented in part one [8] they were only capable of calculating the diffusion coefficients for β-Ti(Ni) and NiTi which are presented in a separate article (part two) [9]. The lack of concentration gradient in the Ti_2Ni phase and the non-parabolic growth of the $NiTi_3$ phase made calculating the diffusion coefficients for these phases impossible. The inter-diffusion coefficient for β-Ti was found to be an order of magnitude larger than for NiTi. By comparing the ratio of the Ni and Ti intrinsic

diffusion coefficients to the movement of the marker interface it was determined that Ni is by far the fastest diffusing element in the system. This is an important finding since an imbalance in diffusion rates will lead to a local buildup of vacancies [5] potentially resulting in porosity.

Maaza *et al.* [10] utilized neutron reflectometry to analyze the diffusion of Ni into Ti. Again it was found that the Ni diffused into the Ti layers. The speed with which Ni diffuses through Ti is discussed by Herzig *et al.* [11]. Ni diffuses 3 orders of magnitude faster than O and 6 orders of magnitude faster than Ti in α-Ti. Ni, Fe and Co impurities in Ti were found to enhance bulk self-diffusion of Ti but had little effect on grain boundary self-diffusion.

The intermetallic of interest in the Ni-Ti system is the shape memory alloy NiTi. NiTi converts from a high temperature austenite (B2 cubic crystal structure) to a martensite at low temperatures (ultimately a B19' monoclinic crystal structure). During the B2 to B19' phase transformation one of the following two phases can be an intermediate phase: the R-phase (it is trigonal) or an orthorhombic B19 phase [1]. This transition temperature is affected by Ni content, alloying additions and thermo-mechanical treatments. When Ni content is less than 54.1 wt% Tang *et al* [6] determined by thermodynamic modelling that the transformation occurs at 65 °C during non-equilibrium cooling conditions. For Ni contents higher than 54.1 wt% they determined the transformation temperature decreases at a rate of 180 °C per increase of 1.2 wt% Ni. Alloying additions can change the stability of the B19' phase resulting in a transformation sequence that includes one of the intermediate phases (e.g. B2→B19→B19' with additions of Cu). Ni-rich alloys can be

heat treated to precipitate out Ni_4Ti_3, removing Ni from NiTi and increasing the transformation temperature. The size and dispersion of the precipitates also affect the transformation temperature by restricting the distortion of the lattice. The transformation strains are the smallest for the R-phase (~1 %), increasing for B19 (~8 %) and are the largest for B19' (~10 %) [1]. While a fine dispersion of precipitates does not affect the R-phase (low transformation strain) it results in lowering the start of the B19' transformation (M_s). Cold work has a similar effect, lowering transformation temperatures due to a highly strained lattice.

1.4 POWDER METALLURGY (PM)

Powder Metallurgy (PM) is a manufacturing technology that produces near net shape parts requiring minimal machining and producing little material scrap. These two factors combine to realize cost savings in high production parts with complex shapes. The reduction in machining also means lower volume but difficult to machine parts such as tungsten carbide inserts are near impossible to manufacture any other way. Another advantage of powder metallurgy is the large diversity of materials with a controlled chemical homogeneity that can be utilized. Through powder metallurgy non-equilibrium chemistries can be produced resulting in finished parts with properties unobtainable by traditional manufacturing methods (e.g. Crucible Particle Metallurgy (CPM®) tool steels with high V contents) [12].

Powder consolidation into a green part occurs through compaction (e.g. die compaction, roll compaction or isostatic pressing) or injection molding (through the use of a binder).

The green part is then sintered to create a mechanically sound part. Depending on the application the final part can have a low relative density (e.g. filters) or be fully dense (e.g. automobile connecting rods). Additive manufacturing typically forgoes a green part and melts the powder into the final shape layer by layer.

At the core of the PM technology is the raw powder feedstock. A high green density typically results in a high final part density which is important for mechanical properties. The ability of a powder to compact is an inherent property of the powder and varies with powder chemistry (i.e. elemental or pre-alloyed) and powder production routes (influencing powder morphology and size). Poor powder compaction properties require higher forces and larger presses for high green densities. The choice of powder chemistry is typically chosen by the end use, where as there is more variability in the choice of production route.

1.4.1 *Powder production*

There are four main categories of powder production: mechanical, electrolytic, chemical and atomization. Each process works well for certain materials but not for others and yields specific powder properties. Table 1-1 lists the various techniques and some commonly used elements along with some of the morphologies produced. Only the powder production methods utilized to produce Ni or Ti will be discussed in more detail.

Table 1-1 Characteristics of various powder production routes (compiled from [12]).

Powder manufacturing Technique		Metals used	Possible Powder Morphologies	Powder Size Ranges
Mechanical	Machining	Metal that can be machined	curled, irregular	large powder
	Milling	Brittle Material, Ti (hydride-dehydride), Nb (hydride-dehydride), W	angular and irregular	medium powders, D_{50} 10 to 100 μm
	Mechanical Alloying	Typically soft precursor metals, hard to produce alloys	angular particles	medium powders, D_{50} 10 to 100 μm
Electrolytic		elemental powders only, Cu, Fe, Ag, Mn, Cr, Zn	dendritic, angular, sponge like	medium powders, D_{50} around 40 μm
Chemical	Decomposition of a solid	Fe, W, Mo, Cu	Internal porosity, rounded to irregular, spongy	Fine to medium powders, D_{50} 3 to 50
	Thermal Decomposition	Ni, Fe, Co, W	Spicky, sperical, round to spherical	Fine to medium powders, D_{50} 3 to 50
	Precipitation from a liquid	Cu, Ni, Co, Ta, Ti	irregular, cubic or sponge like	Fine to medium powders, D_{50} 1 to 70 μm
Atomization	Water atomized	Non reactive metals, Fe, stainless steels, Ni	rounded to irregular	medium to large powders, D_{50} 40 to 100 μm
	Gas atomized	Any metal or alloy that can be melted, Fe, Al ,Mg, Ti, Zn	ligmental to spherical, rounded	medium to large powders, D_{50} 12 to 180 μm
	Centrifugal atomization	Ti, Zr	spherical	medium to large powders, D_{50} 40 to 100 μm

A common method for producing fine Ni powder is thermal decomposition. This entails the decomposition of a precursory compound into a powder. Commonly termed "carbonyl vapour metallurgy", this process takes a metal and transforms it into a metal carbonyl liquid. It is then heated and the metal is recovered as a powder. The powder shape of the Ni is 'spiky' with a larger surface area. An important point here is that only elemental powders are produced.

Liquid metal atomization is another way in which Ni powders can be produced. Essentially a liquid metal stream is obliterated into fine drops which solidify. These processes are low to medium cost, high volume and provide good control over particle size and shape. Due to the low reactivity of Ni it can be either water atomized or gas atomized. In water atomization a stream of water is used to disrupt the flow of liquid metal resulting in irregular shaped powder particles. This is the cheapest atomization

route but the process tends to produce coarse particle sizes with relatively high oxide content. Gas atomization uses a large depressurization zone at the molten metal outlet to disrupt the metal producing a variety of powder shapes from ligmental to spherical. Gases ranging from air to inert atmospheres are used.

Ti is a very reactive metal making water or even air atomization an impractical production method. While inert gas atomization is used centrifugal atomization produces higher quality powders. Centrifugal atomization utilizes centrifugal forces to send flying droplets of molten metal. It produces perfectly spherical powders but cannot produce a fine powder size and has a low production volume making it more expensive. Mechanical production routes are also commonly utilized to produce Ti powders. Typically scraps from machining processes can be turned in to powders through milling. In this case, the Ti has to be made brittle. This is done by hydriding the Ti (i.e. it is milled as TiH_2) for milling and dehydriding post milling. This results in angular and irregular powder shape. However it is a common method to produce Ti powders with a smaller particle size. Direct production of pre-alloyed NiTi powder is possible through gas atomization [13–15] or centrifugal atomization [16] of the bulk alloy but is expensive.

1.4.2   *Powder characterization*

Important powder characteristics affecting powder compaction properties are its apparent density and its flow properties. The apparent density is a good indication of how well a powder compacts on its own with no external force exerted. The higher the apparent density, typically the easier it will be to achieve high green densities. Apparent density is usually measured using an Arnold meter. An Arnold meter consists of a block containing

a hole with a 20 cm³ hole drilled into it. A pipe filled with powder is passed over the hole twice. The mass of powder in the hole divided by the volume yields the AD of the powder. This gives density units of g/cm³.which can be converted into a % relative density by dividing by the elements nominal density.

The flow of the powder is an indication of how well powder particles will flow past themselves and is important when considering how a flowing powder will fill a die. This is measured with a flow meter and has units of g/s. A known mass of powder is placed in a funnel with a very specific geometry with respect to the slope of the walls and the funnel opening. The time required for all the powder to flow is recorded. There are multiple standards for flow meters. The appropriate flow meter depends on the flowability of the powders under investigation.

Apparent density and flowability are both dependent on powder size and shape. Some methods to determine powder size are sieving, laser particle size analyzer and microscopy. Irregularly shaped powders will yield different results depending on the method used. Microscopy is a good way to determine the shape of the powders.

Powder analysis helps to predict powder compaction behavior. In a press and sinter operation, once the loose powders fill the die they are compacted. At this stage the compaction pressure controls the "green body" density. The relationship is not linear however; at some point increased pressure will result in minimal increase in green density. Pressing beyond this point is considered to result in diminishing returns.

1.4.3   *PM and NiTi*

For some time (since the early 1980's [13,14,16–41]) investigations into the production of NiTi by means of powder metallurgy have been carried out. Some have concentrated on using pre-alloyed powders which show good homogeneity and lower impurity levels, but are expensive [14,16–18,23,24,28–31,38,41]. Despite the high degree of homogeneity and low impurity levels the pre-alloyed powders are not immune to the inclusion of Ti_2Ni or TiC as a secondary phases through the uptake of C and O during ingot production [14,23,28,29,31,42]. NiTi holds little O compared to Ti_2Ni [43] as such many of these researchers pin the persistence of the Ti_2Ni secondary phase on oxygen contamination which they claim stabilizes the Ti_2Ni phase. This phase is commonly referred to as an oxide and noted as Ti_4Ni_2O or $Ti_4Ni_2O_x$, however due the similarity in crystal structure between Ti_4Ni_2O and Ti_2Ni it is difficult to distinguish between the two [14,23,25,28,29,31,42,44].

Others have utilized less expensive elemental Ti and Ni powders in an attempt to form a homogeneous and sometimes dense NiTi during sintering [13,19–23,25–27,32–37,39,40,45]. Unlike pre-alloyed powders, homogenization through solid state sintering of elemental powders has proved more difficult. Studying the Ti-Ni binary phase diagram in Figure 1-1 provides the reason for the difficulties. The two 'intermediate' intermetallics Ti_2Ni and Ni_3Ti form during sintering and are more thermodynamically stable than NiTi, making them difficult to remove [19,21]. The formation of the intermetallic phases Ti_2Ni, NiTi and Ni_3Ti are highly exothermic, potentially leading to self-propagating high-temperature synthesis (SHS) [20,46]. In essence the heat evolved from the localized reaction of intermetallic formation can, under the right circumstances,

produce enough heat to maintain a rapid rate of reaction converting elemental Ni and Ti into intermetallics. SHS can be onset by heating until liquid is formed, termed the thermal explosion mode (TE-SHS), or by sparking one side of a compact at low temperatures, termed plane wave propagation mode (PWP-SHS) [46]. As will be discussed TE-SHS can occur to various extents during reactive solid state sintering if conditions are not monitored carefully. PWP-SHS will not be discussed further as it is outside the scope of the thesis.

Early work on conventional sintering of elemental powders found density and homogeneity to be competing factors [19–21]. During solid state sintering of Ni-Ti (as the compact homogenizes) Ni diffuses much more rapidly than Ti leading to Kirkendall porosity [19,20]. While the formation of liquid speeds up homogeneity, inter-diffusion (a necessary precursor for the formation of liquid) means a skeletal network of higher melting point phases has already formed. The liquid that forms is drawn off by capillary forces leaving behind large pores and causing swelling [19,20]. Morris and Morris [19] investigated the sintering of 75-150 μm Ni and 150 μm Ti. While no heating rate was provided, sintering up to 900 °C showed solid state diffusion. Sintering up to 950 °C showed some interdiffusion but also large new pores which were interpreted as first liquid formation. Significant melting was found to occur with a complete loss of shape when sintered to 1000 °C. However sintering to the latter temperature produced a material that 'appeared' well alloyed.

Employing a smaller Ti powder size (-45 μm) and three 99.9 % Ni powders (2-5 μm, -45 μm and -150 μm) Zhang *et al* [20] investigated the sintering behaviour of two Ni:Ti

ratios (at%): 51:49 and 48:52. Being aware of the large scale porosity caused by the liquid phase at the 942 °C Ti-rich eutectic, and wishing to avoid it, specimens were heated to only 900 °C. After 30 hours the coarse Ni powders showed poor homogenization while the -45 μm Ni mixture showed extensive homogenization after only 5 hours. As expected this result shows the increased rate of homogenization with smaller powder sizes. Heating straight to 1050 °C the -45 μm Ni mixture showed good homogeneity but large pores at the original titanium particle site due to Ti-rich liquid penetrating along the Ni particle boundaries. From these findings Zhang *et al* determined a best practice that included heating from 750 to 900 °C at 2 °C/min and holding for one hour. This was followed by heating to 1150 °C and holding for 30 minutes. The rate of the second ramp rate was found to be of no consequence. This latter sintering profile provided a homogeneous microstructure and a fine pore structure (still only 82 % dense) that was attributed to liquid phase sintering. However no proof for liquid formation is provided in the manuscript. Using the same sintering profile on the Ti-rich (48 Ni : 52 Ti) mixture showed larger pores than the Ni-rich mixture and a stable Ti_2Ni precipitate.

Hey and Jardine [21] investigated a 50:50 (at %) NiTi using equal sized 44 μm 99.9 % Ni and 99.5 % Ti powders. The powders were heated to temperatures ranging from 800 °C to 1000 °C at 5, 10 and 800 °C/min for various hold times. At 5 °C/min the largest barrier to homogenization was found to be Ni_3Ti. Heating at 10 °C/min both Ni_3Ti and Ti_2Ni were found alongside NiTi after holding for 6 hours at 1000 °C. Ti_2Ni was only found using EDAX as it was not seen in the XRD pattern (thought to be hidden by the B19' martensite peaks). Sintering at 800 °C/min was accomplished by placing a specimen in a furnace preheated to 900 °C. The specimen underwent severe shape

deformation with the top of the specimen looking like it had melted. The explanation provided by Hey and Jardine is that the heat liberated during intermetallic formation could not be dissipated rapidly enough to avoid significant melting leading to shape loss.

These early works provided some insight into the importance of powder sizes and heating rates on the sintering of elemental NiTi as well as the influence of liquid caused by the Ti-rich eutectic at 942 °C. Many later studies used two step heating procedures, lower sintering rates or sintered below the 942 °C eutectic in order to avoid large scale porosity caused by liquid formation [25,26,33–35,47,48]. Studies by Biswas [46] and later by Whitney *et al* [32,33] provided more understanding on the reactive sintering mechanism and how it was tied to liquid formation and TE-SHS. It was determined that the during solid state sintering the phase progression is as described in Chapter 1.3 up to 942 °C. The three intermetallics form as layers isolating the reactants. Between the 942 °C eutectic and the Ti_2Ni peritectic a Ti-rich liquid is formed and comes into contact with elemental Ni, igniting the TE-SHS reaction. Whitney *et al.* [32] showed that as soon as liquid is formed the TE-SHS is initiated. They were also able to tie the size of the exothermic peak associated with the TE to the amount of β-Ti (and hence solid state diffusion) that was in the microstructure. More solid state diffusion decreased the amount of β-Ti and therefore decreased the amount of TE-SHS. Larger TE-SHS events were tied to a greater degree of homogeneity and significant shape distortion due to more liquid present and higher internal temperatures [46]. The temperatures were high enough to melt the intermetallic network formed during initial solid state sintering [46].

From this new understanding the older investigations can be understood. The specimens heated straight to 1000 °C by Morris and Morris [19], or to 1050 °C by Zhang *et al* [20] underwent TE-SHS with little solid state sintering. The specimens held at 950 °C or lower prior to heat above 1000 °C underwent a muted TE-SHS reaction, one in which homogenization was more rapid but the heat evolved during intermetallic formation was insufficient to melt the preexisting intermetallic network of NiTi and Ni_3Ti. The rapid solid state intermetallic formation during heating to 900 °C at 800 °C/min by Hey and Jardine [21] likely induced local temperature rises above 942 °C leading to liquid and TE-SHS. Results by Corbin and Cluff [34] have shown that holding for 10 minutes at 900 °C with approximately the same size powder mixture as used by Zhang *et al* [20] in their two stage sintering profile is sufficient to eliminate all β-Ti. It is thought that despite Zhang's attempts at liquid phase sintering no liquid was indeed present.

Past attempts at producing a dense, homogeneous NiTi through the use of 'spark plasma sintering' (SPS) using elemental powders have been met with mixed success. In 2007 Majkic *et al* [49] used a modified SPS machine to concentrate current flow through the powder by electrically and thermally isolating the die wall from the punches and the powder. They produced a dense microstructure with minimal Ti_2Ni (< 3 vol%) after 30 min under a 7.7 MPa pressure and a constant 'nominal' current density of $2960KA/m^2$. A temperature of approximately 900 °C was measured inside one of the punches. More recently Novak *et al* [50] found that the surface heating affect in SPS produced a layered intermetallic structure similar to conventional sintering that was independent of heating rate. No hold time was given and the powders sizes used were 5-6x larger for Ni powders and up to 2x larger for the Ti powders compared to Majkic *et al*. The short hold times

used in SPS do not lend themselves to long range diffusional processes such as those found during the sintering of elemental powders to produce a homogeneous NiTi. As such most of the SPS investigations have centered on mechanically alloyed powders [2,51–54] or pre-alloyed NiTi powders [55–57] to increase homogenization of the powder prior to sintering. While this has proved beneficial all the references above show residual Ti_2Ni in the microstructure save Zhao *et al* [55] where no microstructural investigation was performed to determine the level of homogenization.

Over the years homogeneity has remained a struggle in sintering from elemental powders. However unlike the earlier reports discussing the difficulty of removing Ni_3Ti, Ti_2Ni has often been discussed as problematic due to the stabilizing effect of O [14,25,26,35,47,48,58]. Oxygen in the starting powders can lead to the formation of $Ti_4Ni_2O_x$ that is difficult to remove. Recently Frenzel *et al* [59] have suggested that the phase is not an oxide but a solid solution ($Ti_2Ni(O)$) based on previously reported ternary diagrams. This knowledge is by no means universal, with recent publications by Chen, Liss and Cao [60–62] showing *in-situ* evidence of a Ti_2Ni phase at temperatures above the 984 °C peritectic in Ni-rich NiTi alloys for which they offer no explanation. Little research has been performed on the Ti-Ni-O system in the 984 ºC plus temperature range with the low O quantities present in the NiTi sintered from elemental powders. To reduce contamination from oxygen some researchers have gone to the lengths of using a calcium reductant vapor [47,48]. Bertheville and Bidaux [48] have shown that using a calcium reductant vapor the residual $Ti_2Ni(O)$ phase was avoided and a single phase NiTi microstructure was produced.

1.5 TESTING METHODS

1.5.1 *Differential Scanning Calorimetry (DSC)*

A calorimeter is a thermal analysis instrument used to quantify the heat flow during a chemical reaction. Specifically, a DSC measures the difference in heat flow between a sample and a reference during a dynamic heating profile. It is important that sample and reference both undergo the same heating profile. There are two types of DSCs. The first is a power compensated DSC and the second is a heat flux DSC. In a power compensated DSC the sample and reference are heated in separate but identical chambers. The power required to maintain the same temperature in both the sample and the reference side is recorded. The heat flux DSC is what is used in the present research and will now be explained in more detail.

In a heat flux DSC both specimen and sample are in the same chamber. They sit on a conductive carrier which has the thermocouples attached directly to it. This eliminates sample-thermocouple interactions and ensures the output signal is less dependent on the thermal properties of the sample [63]. Through calibration the difference in temperature is converted to a heat flux. A change in the baseline indicates a transition or phase change taking place. From a DSC we can obtain heat capacities, latent heats as well as melting temperatures, glass transition temperatures etc…

Accurate evaluation of DSC traces takes experience and knowledge of the potential phase transformations within the specimen. An example of a DSC trace and how to evaluate it is shown in Figure 1-3. The trace belongs to an elemental powder metallurgy Ti specimen produced by an HDH process. In Figure 1-3a) there are three initial points of interest.

Point i looks like a dip in the baseline. In reality this is the start of the ramp and the deviation is due the lack of stability in the ramp rate. Point ii appears to be a small exothermic peak. This occurs around 460℃. This is likely some remaining TiH_2 decomposing into Ti and H_2. The main peak at iii is the α-Ti to β-Ti transition. This is seen more closely in Figure 1-3b). The evaluation of the peak starts at a point that has a stable baseline (around 870℃) and finishes at a point where the baseline becomes stable again (around 970℃). The onset temperature is defined as the intersection between the tangent to the baseline and the slope of the peak. This is seen at point iv in b) of Figure 1-3 and is measured as 884.2℃ (phase diagram lists 882℃). The enthalpy value is given as -60.89 J/g. The plots are 'exo' (exothermic) up indicating that the transformation is endothermic and an input of 60.89 J/g of energy is required to transform α-Ti to β-Ti.
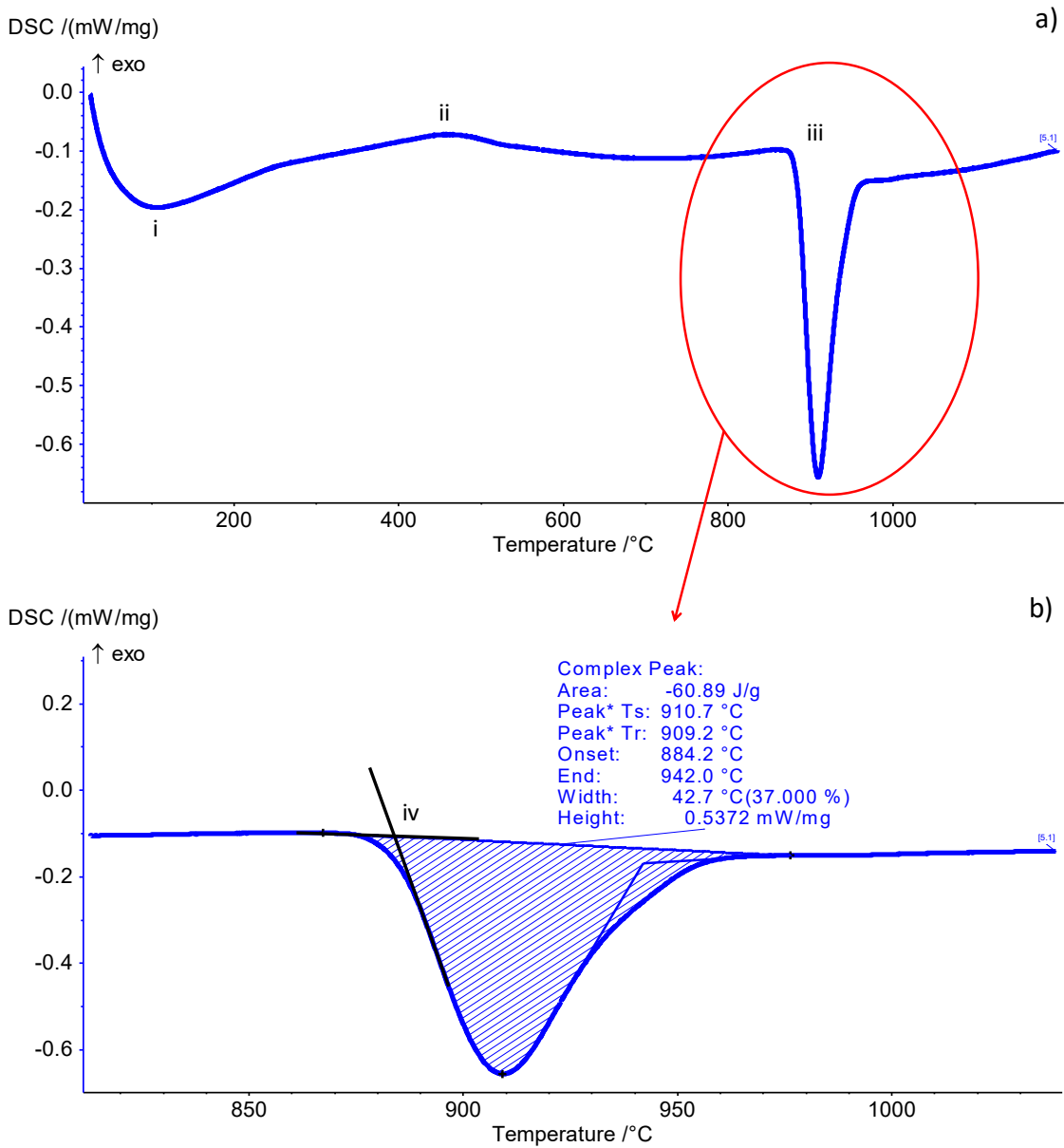
Figure 1-3   Example of a DSC trace and its analysis

In the realm of PM NiTi research a DSC is a common tool used to investigate the martensite ↔ austenite behaviour [1,14,20,22–25,27–30,64–80]. A DSC can determine the starting and finish temperatures of the transitions as well as the formations of any intermediate phases (if there are any). For this purpose a DSC operates between -150 and 150 °C. The use of DSC to investigate the sintering process at high temperatures is less

common. Biswas [46] used a differential thermal analyzer (equivalent to a non-calibrated heat flux DSC) in his investigation of TE-SHS. A DSC was a key tool in the two articles by Whitney, Corbin and Gorbet [32,33] on their investigation into the reactive sintering of NiTi and the TE-SHS event. They were able to link the onset of TE-SHS with the Ti-rich eutectic showing that the amount of β-Ti in the microstructure at the eutectic was related to the size as of the TE-SHS event. The decay of β-Ti (by Corbin and Cluff [34]) and the influence of Ni powder size (by Cluff and Corbin [35]) on the sintering of NiTi was studied using high temperature DSC. More recently Chen, Liss and Cao [61,62] studied the sintering of Ni rich NiTi using a DSC as a preliminary tool prior to performing *in-situ* Neutron diffraction. In an article by Goryczka and Van Humbeeck [75] high temperature DSC was used to evaluate the phase transformations and the sintering behaviour of NiTiCu. Unfortunately the authors mistook the TE-SHS peak as the allotropic α-Ti→β-Ti phase transformation. This serves to highlight that a good base knowledge of the system is required for accurate analysis of DSC traces.

1.5.2   *Diffraction: XRD and Neutron Diffraction*

Diffraction is a useful tool for probing the crystal structure of materials. Diffraction of solid state materials would not be possible if they did not have a crystal structure. Understanding the crystal structure is vital to understanding diffraction. Diffraction with neutrons provides unique opportunities to study processes in-situ. The increased knowledge from these studies can help direct industrial practices making them more efficient.

1.5.2.1 Diffraction and Bragg's Law

Diffraction is the word used to describe the phenomena associated with the interaction of a wave and an obstacle [81]. In crystal lattices, the diffraction pattern is due to phase relations of the outgoing waves (at least two or more) [82]. For two incoming waves with the same wavelength λ (i.e. monochromatic), a path difference between the two waves will lead to a difference in phases of the outgoing waves. Summing up the outgoing waves can lead to constructive or destructive interference. When the path length difference is equal to an integer value of the wavelength (i.e. $n\lambda$) constructive interference occurs. Otherwise the waves destructively interfere with one another, essentially cancelling each other out. This is the premise of Bragg's Law.

The validity of Bragg's law can be shown graphically using real space. Figure 1-4 shows a single crystal in real space with an incoming and reflected monochromatic beam. In the figure, the distance DA is the plane spacing d. The difference in path length between the upper and lower beam is BA+AC. From the geometry shown we can see that BA = AC = $d\sin\theta$. The path length difference is then twice $d\sin\theta$. With the requirement of constructive interference in the reflected beam, we see that the relationship between plane spacing, wavelength and incident angle becomes – Bragg's Law:

$$\boldsymbol{n\lambda} = 2d \sin \theta \tag{1-1}$$
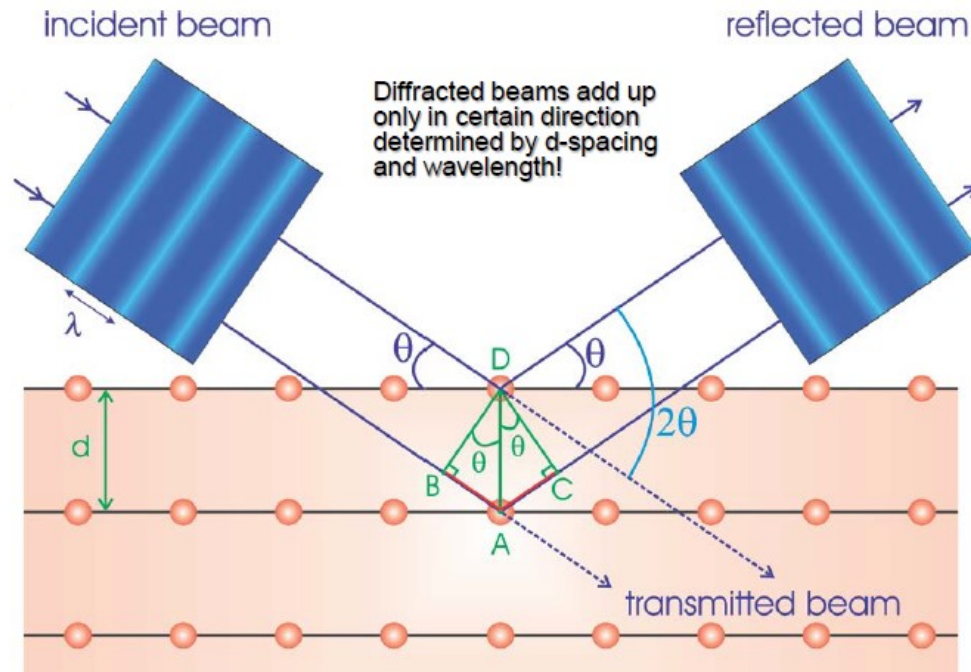
Figure 1-4   Diffraction of a monochromatic wave from a single crystal (from [82]).

From this result we can see that for a given lattice spacing there is a maximum wavelength that can be used. Since by definition $\sin\theta \leq 1$, we must have $\lambda \leq 2d$ [82]. For typical crystalline materials $d \approx 3$ Å or less which means that a wavelength larger than 6 Å will not be able to meet the diffraction condition outlined by Bragg's Law [82].

1.5.2.2 Powder Diffraction and Intensity Calculations

In diffraction the two variables we can control are incident beam wavelength - λ and the incident angle-θ. If we can control these, we reduce Bragg's law to only one variable d. Figure 1-5 shows a schematic of an experimental diffractometer setup. Radiation leaves the source at point 'S' and travels through a slit at point 'A'. This slit serves to define and collimate the beam incident on the specimen sitting at point 'C'. The beam is diffracted

by the specimen and due to the slit at point 'F' forms a convergent beam which strikes the detector at point 'G'. The slit at point 'B' collimates and defines the diffracted beam. It also serves the purpose of reducing the area to the small triangle above the specimen in which the radiation scattering off the molecules in the atmosphere will make it to the detector. The angle between the incoming radiation and the diffracted beam is 2θ.
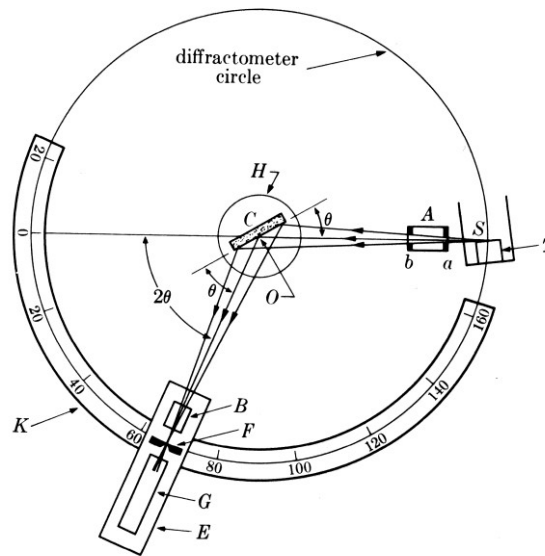
Figure 1-5   Schematic of a diffractometer (from [82]).

The result of a powder diffraction experiment is a diffraction pattern. A diffraction pattern of an NiTi shape memory alloy can be seen in Figure 1-6. Important information from a diffraction pattern is the peak location and peak intensities. These two pieces of information can identify an unknown sample by comparing it to a database of diffraction patterns of known materials. It is not uncommon for a shift in the lattice parameter to occur due to thermal expansion or lattice strain (e.g. from mechanical loading or due to alloying). In this instance using the peak location the plane spacing can be calculated.

Further if the material and the plane index (e.g. the first peak in Figure 1-6 is a 110 peak) is known, we can calculate the new lattice parameter and evaluate either the temperature of the specimen or the level of strain.
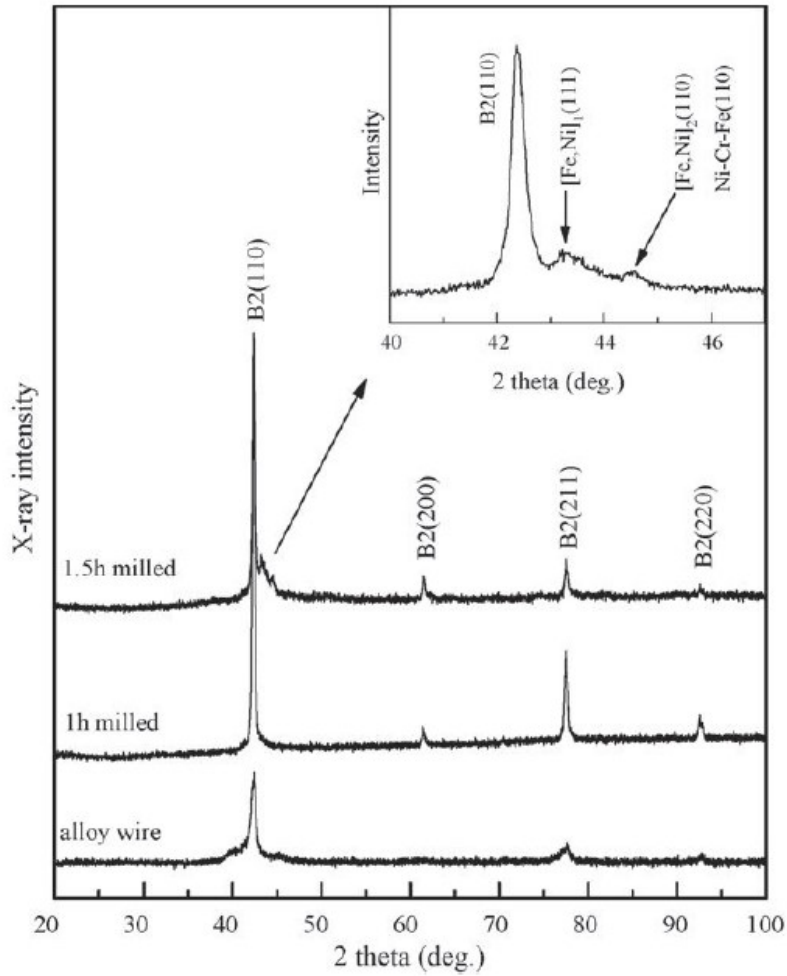
Figure 1-6   **Diffraction pattern from a Ni rich NiTi shape memory alloy (from [15]).**

The intensity of an (hkl) peak, $I(\theta)$ can be calculated by (modified from [83]):

$$I(\theta) = I_0 P(\theta) L(\theta) |F^2| M(hkl) DW(hkl) \tag{1-2}$$

28

This equation is mainly for x-rays but with a few modifications can be used for neutrons as well [82]. What the equation means is that starting with an initial intensity of I_0 the intensity observed is altered based on the remaining terms. The polarization factor $P(\theta)$ relates to the electric field of the x-rays. When the x-rays are diffracted changes in direction depend on the scattering angle. This alters the intensity measured by the detector [83]. The Lorentz factor, $L(\theta)$, applies to both neutrons and x-rays. It is a geometrical factor causing a reduction in intensity because the detector can only measure a fraction of the diffracted signal from the specimen. This effect is magnified at higher angles. The Lorentz factor is one reason for a reduced measured intensity at higher scattering angles. The structure factor $|F^2|$ is a function of scattering element and crystal structure. It is comprised of two functions as follows [82,83]:

$$F = \sum_j f_j e^{2\pi i (h x_j + k y_j + l z_j)} \tag{1-3}$$

Here the first function, f_j is the scattering amplitude and it addresses the phase differences due to path length differences that arise from waves scattering off different locations of the j atom in the (hkl) plane (much like off two planes only much smaller distances). Similar to the plane analogy it is affected by both wavelength and scattering angle, decreasing in value at higher diffraction angles for a constant wavelength. For x-rays which scatter off the electron cloud, this function is related to the atomic number Z. Larger Z atoms scatter more intensely than smaller Z atoms. In contrast neutrons scatter off an atom's nucleus. This factor is therefore related the apparent size of the atom to neutrons, its atomic scattering length b_j. Unlike for x-rays the value of b_j is not related to the size of the atom.

The second term, $e^{2\pi i(hx_j+ky_j+lz_j)}$, takes into account scattering off all the atoms in the unit cell. The atom positions are given by the fractional atomic Cartesian coordinates (x_j, y_j, z_j) [82]. This function is the same whether x-rays or neutrons are used. Atoms that do not lie on the (hkl) plane can cause destructive interference with the x-rays scattered from the plane itself. This can result in 0 scattered intensity (sets the structure factor to 0) for some planes even though they are oriented at their Bragg angle.

The $M(hkl)$ term is the plane multiplicity. It follows that if 8 planes have the same spacing compared to 1 there is 8 times more chance that one will be correctly oriented and so the intensity will be eight time higher. The final term, $DW(hkl)$ is the Debye-Waller term. This term is related to atom vibrations. At higher temperatures increased atom vibrations about the average position decrease the peak intensity. This effect increases with wavelength such that peak intensity decreases more at higher wavelengths. $DW(hkl)$

The Debye-Waller effect accounts for the loss in intensity but temperature affects the pattern in another way as well: thermal expansion. Except for materials with a zero coefficient of thermal expansion (CTE), materials typically undergo volume changes when the temperature changes. This bulk volume change is due to changes in the volume occupied by the individual atom as its vibrational energy changes. This changes lattice parameters. Metals which have a positive CTE will expand meaning lattice parameters will increase. This will show up on the diffraction pattern as a shift to lower angles. In fact diffraction is one way to measure CTE [84,85].

1.5.2.3 Rietveld Refinement.

Determining structural information from powder diffraction was difficult due to the loss of information from randomly oriented grains and more importantly from the overlap of independent diffraction peaks [86]. Prior to the method described by H. M. Rietveld [86] the powder diffraction patterns were analyzed by integrating the areas under the peaks. This meant however that when peaks overlapped they were often treated as a single peak, with a significant amount of information lost. The Rietveld method was originally proposed to overcome the issue of overlapping peaks in single wavelength powder neutron diffraction [87].

The Rietveld method is what is termed whole pattern fitting. For a given initial crystal structure and wavelength Rietveld calculated the intensity vs 2θ using an equation similar, but more involved than equation 1-2. Additions to the intensity equation included profile peak shape fit parameters (relate to the instrument being used) and preferred orientation among others. Through a least squares refinement algorithm the variables (which include but are not limited to lattice parameters, atomic positions, atom occupancy) are refined until the equation 'fits' the experimental pattern. In this way the overlapping peaks are treated as two separate peaks that summed to one peak instead of being treated as a single peak greatly enhancing the information one can obtain from a powder diffraction pattern.

Over the years, the Rietveld method was expanded to include time of flight neutron powder diffractometers, conventional x-ray diffractometers, as well as x-rays from synchrotron sources [87]. In 1988 Bish and Howard [88] described the process of using

the Rietveld method for quantitative phase analysis without the need for calibration or internal standards, assuming the sample is wholly crystalline. For samples with amorphous phases, the amounts of the amorphous phases could be determined using an internal standard. Some of the benefits of the Rietveld method over the relative intensity ratio method is that it can account for preferred orientation, does not need standard intensities for each phase present, determination of precise cell parameters and approximate chemical compositions [88].

The pattern is calculated in absolute units and then scaled to the observed pattern. The intensity at point i of a pattern is calculated as follows ([89,90]):

$$y_i^{calc} = y_{b_i} + y_{d_i} + \sum_p S_p |F_{p,i}|^2 \Gamma_{p,i} K_{p,i} \qquad (1\text{-}4)$$

The values of y_{b_i} and y_{d_i} are the contributions of the background and diffuse scattering respectively. S_p is the scale factor for the contribution of phase p to the total intensity value at point i. The structure factor for a particular reflection of phase p at point i is given by $|F_{p,i}|^2$. $\Gamma_{p,i}$ is the profile peak shape function for phase p and $K_{p,i}$ is the product of various geometric and other correction factors. These factors include phase multiplicity, Lorentz-polarization, preferred orientation and absorption as well as an extinction correction. The Debye-Waller factor from equation 1-2 is included in the structure factor in equation 1-4.

The fitting of the calculated pattern is performed by minimizing the mismatch between the observed (y_i^{obs}) pattern and the calculated pattern (y_i^{calc}) using a weighting function (w_i) as follows [91]:

$$S_y = \Sigma_i w_i (y_i^{obs} - y_i^{calc})^2 \qquad (1\text{-}5)$$

In this case where the observed data is based on counts (of intensity), the errors are purely statistical therefore the smallest uncertainties to the fit parameters are produced using $w_i = 1/\sigma^2[y_i^{obs}]$, where $\sigma^2[y_i^{obs}] = y_i^{obs}$ [91].

Determining the quality of fit is a difficult task. Two of the most common discrepancy values are the weighted profile R-factor (R_{wp}) and a related statistical value, the goodness of fit: χ^2 [87,91,92]. R_{wp} is calculated using the following equation:

$$R_{wp} = \frac{\Sigma_i w_i (y_i^{obs} - y_i^{calc})^2}{\Sigma_i w_i (y_i^{obs})^2} \qquad (1\text{-}6)$$

A typical value for R_{wp} is ~ 10 % for x-rays to a few percent for time of flight neutron diffraction (R_{wp} depends on background noise level) [92] . The goodness of fit is a function of the R_{wp} and the 'best possible' value of R_{wp} termed R_{exp}. The equation for goodness of fit is:

$$\chi^2 = (R_{wp}/R_{exp})^2 = (1/N) \Sigma_i w_i (y_i^{obs} - y_i^{calc})^2 \qquad (1\text{-}7)$$

N in equation 1-7 is the number of observations less the number of parameters being refined. Ideally the value of χ^2 would be 1 [91].

While being the best available these two discrepancy indexes suffer from being an unreliable method for determination of the absolute quality of a fit [91]. High background noise can lead to artificially low values for R_{wp} while high R_{wp} values may mean a poor background fit, but an accurate model and hence fit to the peaks. One problem with χ^2 is that an increase in the quality of data (longer count times and more data points) results in larger values of χ^2. As such a good fit to a pattern with long count times may have a larger χ^2 value than a poor fit to a pattern with shorter count times. The result of this is that these discrepancy indexes are more useful during refinement than an absolute measure of the quality of fit. Both indexes should be getting smaller with each iteration during the refinement. If they are increasing the refinement procedure is going in the wrong direction. The most reliable way of determining the quality of fit is through visual inspection of the experimental data points with the calculated pattern overlaid [87,91–94].

A good fit is indicative of good precision in the refinement data but does not necessarily mean the refinement is accurate. There can be bias due to experimental set up or an incorrectly applied model that can affect the accuracy of the results. Determination of the accuracy is difficult but biases in the data can be minimized by proper experimental setup and the use of proper models.

Obtaining good quality Rietveld analyses takes great care from the experimental procedure to the model selection. To reduce bias due to experimental setup the diffractometer should be properly aligned and a standard should be run to determine the zero of the machine (and possibly the wavelength). Care must be taken when choosing

which model to use, for example peaks from single wavelength x-rays have a different shape than those from time of flight neutrons and may require a different peak shape function. The refinement process uses non-linear least squares minimization and requires initial guesses to parameters to be reasonably close to avoid false minima. As this document is not meant to teach how to perform Rietveld analysis the interested reader is referred to the literature for guidelines on Rietveld refinement [91,92,95,96]. The Rietveld Round Robin articles by the International Union of Crystallography Commision on Powder Diffraction provides a good analysis of common errors that can result in poor refinements [87,93,94,97].

1.5.2.4 Neutron Diffraction

Using reactor based sources or spallation source neutrons are expensive and they generate fluxes at levels x-ray tubes did in the 1940's [98]. So this begs the question: why use neutrons? The answer lies in the fact that it is a neutral particle that has a magnetic dipole moment. Being neutral, neutrons are able to penetrate deep into matter because they are unaffected by the electron cloud of an atom. Instead, neutrons interact with matter by nuclear forces which are approximately 100 000x smaller than the center to center distance between two atoms [90]. This allows for the use of elaborate experimental equipment to be used such as furnaces, cryostats and pressure vessels greatly increasing the ability to perform in-situ measurements [85]. Also, interacting with the nucleus means that the scattering ability is not related to number of electrons present in the atoms. Figure 1-7 shows a plot of neutron and x-ray scattering amplitudes. Note how the x-ray amplitudes increase with increasing atomic number where as for neutrons the scattering

ability is unpredictable but remains on the same order of magnitude. This highlights that atoms scatter x-rays better than neutrons. With lower scattering amplitudes and lower fluxes from neutron sources, getting a clean pattern with sufficient intensity takes much more time than on an x-ray diffractometer.
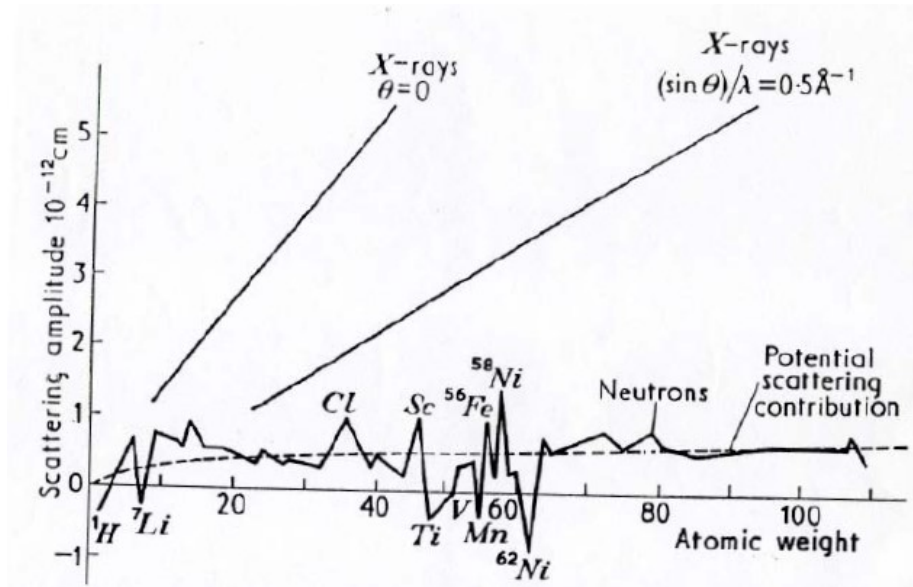
Figure 1-7   Scattering ability of elements to neutrons and x-rays [99]

Another important result of the difference in scattering amplitudes is that light atoms like O scatter as well or better than heavier atoms like Ti or Ni. Therefore scattering from planes with O present can occur with greater intensity. These planes are thus less likely to be confused with background noise. A pertinent example is the scattering of Ti_4Ni_2O (Figure 1-8). The diffraction patterns have been calculated using VESTA [100] and RIETAN-FP [101] based on the crystal structure given by Mueller and Knott [102] and Takeuchi *et al.* [103]. While there are no new peaks in the ND pattern compared to the XRD pattern there is a big change in the relative intensities due to the increased

36

scattering amplitude of O with respect to Ti and Ni. This can be used to great advantage in the determination of crystallographic structural information in phases with light elements.
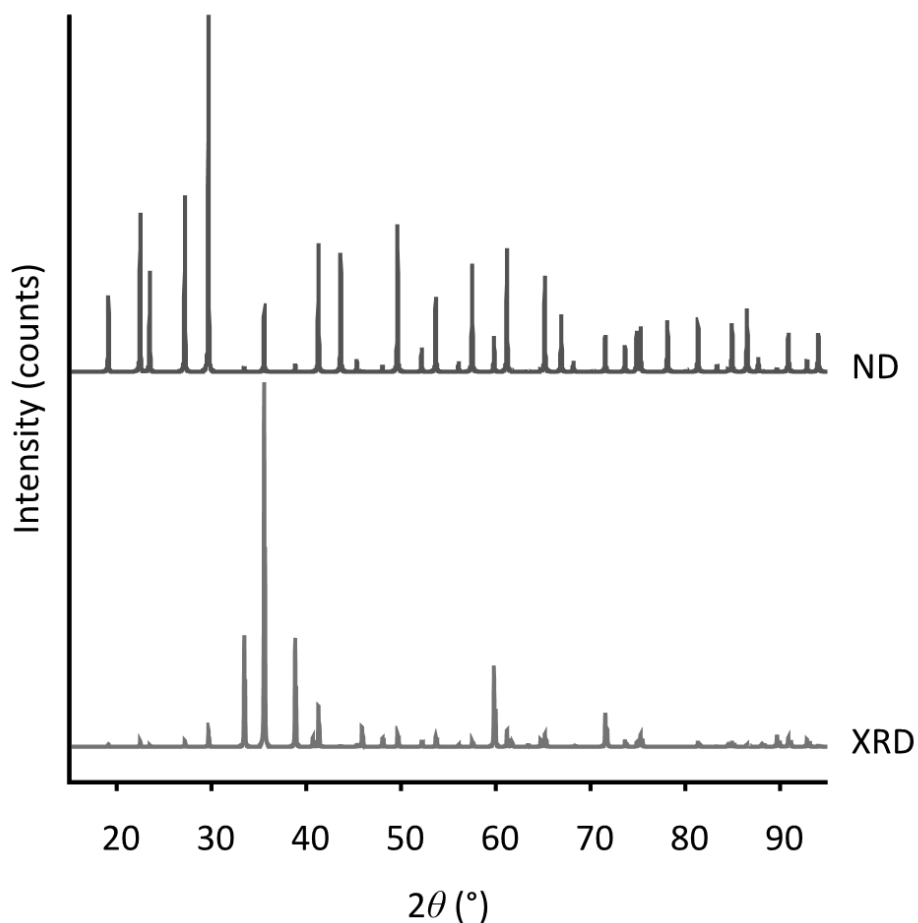
Figure 1-8   Difference in the calculated diffraction patterns of Ti$_4$Ni$_2$O produced by neutron diffraction (ND) and x-ray diffraction (XRD). Both traces are based off a constant wavelength of 1.33 Å.

Less important to the present discussion but a very important advantage of neutrons is that they have a magnetic dipole moment. Neutrons can help determine the magnetic moments of atoms and how they align in a magnetic structure.

1.5.2.5 Prior Neutron Diffraction in-situ experimental work

Of particular interest is the ability of performing in-situ experiments – namely in-situ sintering experiments. The ability of neutron diffraction to yield structural and compositional information in-situ can provide valuable insight into the transient phases and interdiffusion during sintering [85]. Wu *et al.* [104] utilized in-situ neutron diffraction to study the synthesis of Ti_3SiC_2 from powdered precursor. They were able to determine the intermediate products formed that led to Ti_3SiC_2 formation. With the data obtained, they could determine at what temperatures the intermediate phases formed and get a first approximation of reaction kinetics. Further work by Wu *et al.* [105] was performed on the Ti_3SiC_2 ceramic. This time with a layered structure of 3Ti/SiC/C. During heat up the three phases remained separated. Once α-Ti transformed to β-Ti, intermediate phases of TiC_x and $Ti_5Si_3C_x$ began to form. This interesting result would be difficult to obtain ex-situ. In situ neutron diffraction work on the TiAlC system to form Ti_3AlC_2 by $Ti/Al_4C_3/C$ was later performed by Wu and Kisi [106]. This work shows a similarity to their previous work in that the formation of intermediate phases (of which TiC_x is again one) only began once α-Ti transformed to β-Ti. The three previous studies were on relatively slow reactions relying on solid state diffusion. Riley *et al.* [107] utilized a high flux neutron diffractometer to obtain patterns every 0.9 s while observing the self-propagating high-temperature synthesis (SHS) of Ti_5Si_3. Due to the speeds with which SHS reactions take place, it is difficult to obtain much information on the processes involved. Riley *et al.* were able to determine that Ti_5Si_3 is formed directly from the elemental powders with no observable alternative intermetallics. Ex-situ measurements would have possibly shown some intermediate phases that would have

been produced during the cool down stage. It was found that the SHS was preceded by the α →β transformation. Riley *et al.* theorize that it is the interdiffusion initiated in the β phase that onsets SHS.

Turriff [85] used in-situ neutron diffraction to study the transient liquid phase sintering (TLPS) of Cu and Ni. His work shows how different sintering characteristics occur between TLPS and solid state sintering (SSS). In SSS sintering, interdiffusion was much slower, increasing the time required to get a homogeneous alloy. In situ neutron diffraction was able to pick up the point at which the Cu melted. This event was characterized by the disappearance of Cu peaks. During an isothermal hold above the melting point of Cu a new peak emerged. This peak was due to isothermal solidification by way of Cu - Ni interdiffusion. Eventually the Ni peak and the new peak merged indicating a homogeneous alloy. Turriff also used the Al_2O_3 holder as an internal temperature reference. The shift in 2θ due to the temperature increase was correlated by way of known CTE values for a better approximation of sample temperature.

More recently Whitfield *et al.* [108] utilized in-situ neutron diffraction to study the sintering of a metal injection molded stainless steel. In-situ neutron diffraction allowed them to analyse the phases present during sintering profiles that mimicked ones used in industry. In order to achieve better densification the steel is typically heated to the two phase γ + δ region. The δ- phase forms in pores and grain boundaries and speeds up shrinkage. The problem is that it remains in the microstructure upon cooling. The δ-phase being a weak phase degrades the final product. Through in-situ neutron diffraction the authors were able to determine and suggest a sintering regime which allowed

sufficient δ to form for shrinkage purposes but reduced the amount of δ- phase in the final product.

Although not a sintering problem, Kasprzak *et al.* [109] investigated the solidification of a hyper-eutectic Al-Si cast alloy. In-situ neutron diffraction detected the Si phase, both primary and eutectic, and the Al phase during the Al-Si eutectic nucleation. Also seen in the diffraction patterns was the presence of a Si peak near the liquidus temperatures. What is more, in-situ diffraction detected peaks associated with α-Al at around 660 ºC far above the eutectic temperature of 570 ºC. These peaks had disappeared by 625 ºC. Their findings from in-situ neutron diffraction corresponded well with what was predicted by Fact-Sage.

Recently, several *in-situ* neutron diffraction experiments investigating intermetallic phase progression during reactive sintering of NiTi have been published [60–62,110]. Chen, Liss and Cao investigated the production of a Ni-rich NiTi (51 at% Ni: 49 at% Ti) through reactive sintering with both Ti and TiH_2 powders [61,62], as well as the effect of hold temperature (880, 950 and 1100°C) on the sintering of mixtures of elemental Ni and Ti powders having the same Ni rich composition [60]. Their results indicate that the intermetallic phases (Ti_2Ni, NiTi, Ni_4Ti_3 and Ni_3Ti) grow at the expense of the elemental Ti and Ni phases, with the continued growth of NiTi due to the decomposition of the other intermetallic phases present. Ti_2Ni was observed in the diffraction patterns at 1100°C, 116°C above its melting temperature. Upon cooling, a eutectoid decomposition NiTi → Ni_3Ti + Ti_2Ni was observed, resulting in a heterogeneous final microstructure. Quantitative Phase Analysis (QPA) of the diffraction data was performed using the

Rietveld technique, but it was incomplete as Ti was treated as a single phase despite the allotropic α-Ti → β-Ti phase transformation, which impacts the phase evolution. The authors provided few details of the procedure followed for their Rietveld refinement. TE-SHS was not observed due to their choice of powder size and heating rates. The effects of powder purity and powder size were beyond the scope of their investigation.

From these studies it is clear that in-situ work can provide information otherwise unattainable by other methods. To be able to perform high temperature in-situ diffraction is greatly facilitated by the use of neutrons for the large sampling size (avoid significant contributions from a surface oxide layer) and the ability to tightly control the atmosphere.

CHAPTER 2
SCOPE AND OBJECTIVES

Sintering NiTi from elemental powders is a promising way to make complex SMA parts at lower costs. Despite the many years of research into the subject there is still lacking a full understanding of the phase progression or reaction sequence and therefore what an optimium sintering procedure looks like. This is mainly due to the way in which the majority of sintering investigations have taken place. Typically a sintering profile/treatment is proposed based on the knowledge gleaned from post sintering results. The present investigation uses seven different elemental powder mixtures, multiple *in-situ* experimental techniques and microscopy (SEM and optical) to clarify much of the unknown surrounding the sintering of NiTi from elemental powders. The four powders were chosen to provide differences in powder purity and powder size. The major analysis techniques utilized in this study are *in-situ* differential scanning calorimetry (DSC), *in-situ* neutron diffraction and microscopy (both SEM and optical). *In-situ* techniques such as DSC or neutron diffraction have the ability to provide information on the microstructure that is more concrete than post sintered microscopy analysis (although the latter is still very useful). Like all techniques, they must be used in concert to be able to understand the full picture. DSC can show the TE-SHS peak and at what temperature it occurs but it cannot show what phases are present immediately post combustion. In-situ neutron diffraction has this capability. It is an exciting opportunity to be able to capture the phase progression through solid state sintering and combustion with this technique.

The objectives are to determine the differences in phase progression during sintering based on titanium powder purity, titanium powder size and nickel powder size. *In-situ*

differential scanning calorimetry will be used to qualitatively assess levels of intermetallic formation and TE-SHS (if it occurs). Rietveld analysis on the *in-situ* neutron diffraction experiments will provide quantitative phase fractions throughout the sintering procedure. Through the combination of these two techniques and microstructural analysis a better understanding of the sintering process will be gained. *In-situ* information on the phase progression during TE-SHS, currently unavailable in the literature, is another positive benefit.

The negative impact of small levels of oxygen contamination have been recognized in the prior literature both in terms of preventing complete NiTi phase homogeneity and degrading mechanical properties and SMA performance. However, the details of how oxygen contamination influences the sintering process has not been studied. *In-situ* neutron diffraction and Rietveld analysis will be used to track the growth of and oxygen concentration in the $Ti_2Ni(O)$ phase during sintering, answering the questions of its origin and stability within the microstructure. Determining the role of oxygen contamination on phase progression and final homogeneity will also allow an informed decision of the importance of oxygen content on processability.

In addition, Rietveld analysis on the elemental powders and powder mixtures provides important crystallographic information. Lattice parameters for β-Ti(Ni) as well as the Ni-Ti intermetallic phases (Ti_2Ni, NiTi and Ni_3Ti) will be reported up to 1200 °C for the first time.

CHAPTER 3
EXPERIMENTAL PROCEDURE

3.1   MATERIALS

Three titanium and two nickel commercially available powders were used. Sources for the Ti powder include Alfa Aesar and Reading Alloys. The Ni powders were acquired from Alfa Aesar and Vale-Inco. A list of the powders used along with the nominal powder size and lot numbers are listed in Table 3-1. Different purity Ti powders of the same size were chosen to investigate the difference purity has on sintering, while the coarse powders allowed the effect of powder size on sintering to be investigated. The coarse powders were also chosen to slow down the kinetics, making it easier to observe phase progression and the thermal explosion mode of self-propagating high-temperature synthesis.

Table 3-1   List of Powders utilized

Supplier	Powder	Powder size (μm)	Lot
Alfa Aesar	Titanium 99.99 wt% -325 mesh	-45	K03X001
Alfa Aesar	Titanium 99.5 wt% -325 mesh	-45	C23X019
Reading Alloys	CP scrap Ti -170 +200 mesh	75-90	ES019-5-1
Vale-Inco	123 Nickel powder	3-7	3403517
Alfa Aesar	Nickel -150 +200 mesh 99.8 wt%	75-106	G14X064

3.1.1   *Ti powders*

The different Ti powders were chosen based on purity and particle size. Both -325 mesh powders obtained from Alfa Aesar were hydride-dehydride (HDH), however the source

of Ti prior to HDH is unknown. The first had a purity of 99.99 wt% Ti (metals basis) and the second a purity of 99.5 wt% Ti (metals basis). Much of the O contamination of Ti powders comes from the surface oxide. Both -325 mesh Ti powders were sieved to -400 + 500 (25-38 μm) mesh to ensure similar powder size distributions and to reduce the O contamination. The coarse Ti powders purchased from Reading Alloys are produced by HDH using machining scrap as a feedstock. The as-received powder size is -125 +325 mesh. This is further refined for this investigation by sieving to -170 +200 (75-90 μm). The sieved fractions of the 99.99 wt% Ti, the 99.5 wt% Ti and the coarse Ti will hereafter be referred to as HP Ti, LP Ti and RA Ti, respectively.

3.1.2   Ni Powders

The Ni powders acquired from Vale-Inco were produced by thermal decomposition via carbonyl vapor metallurgy. The coarse Ni powder was purchased from Alfa Aesar. It was purchased as -150 +200 mesh (75-106 μm) and has not been further sieved. Its production route is unkown. The Inco 123 Ni and the coarse Ni will hereafter be referred to as F Ni and C Ni, respectively.

3.1.3   Powder mixtures

Seven different powder mixtures were prepared from the elemental powders. These are listed in Table 3-2. The composition of 49 at% Ni with the balance Ti (equivalent to 54.08 wt% Ni : 45.92 wt% Ti) used to study the sintering of NiTi from elemental powders was chosen based on previous studies and would be described in the SMA field as Ti rich NiTi [34,35] so that a martensitic NiTi at room temperature is produced. The

95Ti/5Ni mixture, Ti_2Ni mixture and the Ni_3Ti mixture were required for the analysis of neutron diffraction data from the HP mixture, LP mixture, RA mixture and the CNi mixture. The required mass of each powder is placed in a jar that is then dry mixed for two hours on a ball mill. Die wall lubrication was used, no wax was admixed into the powder.

Table 3-2   List of powder mixtures under investigation

Mixture name	Ni		Ti	
	at% (wt%)	Powder	at% (wt%)	Powder
HP mixture	49 (54.08)	F Ni	51 (45.92)	HP Ti
LP mixture	49 (54.08)	F Ni	51 (45.92)	LP Ti
RA mixture	49 (54.08)	F Ni	51 (45.92)	RA Ti
CNi mixture	49 (54.08)	C Ni	51 (45.92)	HP Ti
95Ti/5Ni mixture	5 (6.1)	F Ni	95 (93.9)	HP Ti
Ti_2Ni mixture	33 (37.64)	F Ni	66 (62.36)	HP Ti
Ni_3Ti mixture	75 (78.62)	F Ni	25 (21.38)	HP Ti

3.2   POWDER CHARACTERIZATION

The following is a description of the techniques used to analyze the elemental powders (HP Ti, LP Ti, RA Ti, F Ni and C Ni) and/or powder mixtures. Powder flowability was not measured as all but the coarse powders could be termed 'non-flowing'.

3.2.1   *Apparent density*

Apparent density (AD) was measured using an Arnold meter. An Arnold meter consists of a block with a hole drilled into it and a massing paper underneath the hole. The hole

has an overall volume of 20 cm^3 [111]. A pipe filled with powder sits on the block. The pipe was passed over the hole twice filling the hole with powder. The block was lifted off and the powder is massed. The mass divided by the density give the AD of the powder. The apparent density was performed on both the elemental powders (HP Ti, LP Ti, RA Ti, F Ni and C Ni) and the powder mixtures. The only exception was the CNi mixture as there was not enough powder.

3.2.2   *Powder size analysis*

Powder size analysis was performed with a Malvern 2600 droplet and particle laser sizing analyzer. It has a measurement range of 1 to 1800 μm. A small mass of powders (~ 2 g) was mixed with distilled water. The mixture passes in front of a helium neon laser. The powders diffract the laser and the extent to which the beam diffracts is related to the powder size. The results were tabulated by a computer. Only the elemental powders were tested for powder size analysis. The C Ni was too heavy to yield accurate results.

3.2.3   *Microscopy*

A Hitachi S-4700 field emission scanning electron microscope (FE-SEM) was used to analyze the morphology of the HP Ti, LP Ti, RA Ti, F Ni and C Ni powders. Loose powders were sprinkled on carbon paste gluing the powders to a mount. Once dried, the mount with the stuck powders was placed in the SEM.

3.2.4   *Chemical analysis*

Chemical analyses on the HP Ti, LP Ti, RA Ti, F Ni and C Ni powders were performed. Hydrogen (on a LECO RH-404), carbon (on a LECO CS-444), oxygen (on a LECO TC-436), and nitrogen (on a LECO TC-436) analyses were performed at ATI Wah Chang (Albany, Or). Inductively coupled plasma optical emission spectroscopy (ICP_OES) analyses were carried out at the Minerals Engineering Center (Dalhousie University, Halifax, NS) to determine the metallic contaminants.

3.2.5   *Compaction curves*

Powder compaction properties were determined for the HP mixture, LP mixture and the RA mixture. First the die wall was lubricated with Lico wax C with acetone as a solvent. Once the acetone had evaporated the surplus wax was wiped from the die. To determine the powder compaction curves a 12.5 mm diameter die with a volume of 0.79 ml was filled with powder. The powder was compacted to a pressure of 200 MPa, 400 MPa, 600 MPa or 850 MPa on a Carver hand press. Following removal from the die the diameter was measured with Vernier calipers (at a resolution of 0.01 mm) at three different locations and the thickness was measured with a micrometer (a 0.001mm resolution) in five different locations to determine the compacted volume. The mass was measured and subsequently the green density of the compact was calculated. Each powder mixture was compacted twice.

3.3   Differential Scanning Calorimetry (DSC)

DSC was performed on a Netzsch 404 F1 Pegasus DSC. The DSC used a platinum furnace capable of a maximum temperature of 1500 °C. It was calibrated using the melting of In, Sn, Zn, Al, Ag and Au by comparing the measured onset temperatures and melting endotherms to the known values. Calibration was verified periodically by running a Au standard. Alumina crucibles were utilized on both the sample and the reference. Discoloration of the crucibles was observed, however previous investigations have shown that oxygen contamination from the atmosphere is more of a concern than from the alumina crucibles.

3.3.1   *Sample preparation and procedure*

DSC specimens were prepared by compacting the powder in a single action compaction die with a diameter of 4.82 mm using die wall lubrication. Typically the specimens were pressed to 850 MPa. Prior to a DSC run the specimen was massed on a Metler-Toledo classic balance with a resolution of 0.01 mg. The diameter and thickness of the specimen were measured with Vernier calipers (resolution of 0.01 mm) and recorded. Specimens varied in mass from ~ 40 to 80 mg and in thickness from 0.4 to 0.8 mm. The specimens were placed as close to the center of the crucible as possible and placed on the sample side of the measuring head. The furnace was lowered and the chamber was evacuated to a pressure of 10^{-5} mbar followed by back filling with 99.999% argon. A dynamic purge of 75 ml/min with 99.999 % argon was used.

For quantitative DSC runs a 'correction file', using an empty crucible on both the sample side and the reference side, was run prior to performing a sample run. The sample was then run using the exact same crucible. The software subtracted the heat flow of the crucible from the 'correction file' from the heat flow in the sample run thus eliminating any thermal effects of the crucible from the final DSC signal.

3.4   MICROSCOPY AND ENERGY DISPERSIVE SPECTROSCOPY (EDS)

For microscopy, specimens were mounted in conductive bakelite (graphite flakes) or in a non-conductive epoxy resin. If mounted in resin carbon paint or tape was used to ground the sample and prevent charging when using the scanning electron microscope. Where noted the microscopic images were etched using Kroll's Reagent.

Optical microscopy was performed on a Zeiss Axiotech 100 reflected light microscope. The microscope contains 5x, 10x, 20x, 50x and 100x objectives for magnifications of 50x to 1000x. Each objective was calibrated for scale using a slide with a laser etched grating.

The same Hitachi S-4700 FE-SEM was used for microstructural analysis as for powder morphology. The EDS detector was attached to the FE-SEM. The detector was a silicon drift detector that had fast count times. The EDS detector was calibrated using Ti_2Ni, Ni_3Ti samples prepared from the Ti_2Ni mixture and the Ni_3Ti mixture. When using EDS the SEM was set to 15 kV and 15 μA to ensure accurate results.

3.5 NEUTRON DIFFRACTION

3.5.1 *Specimen preparation*

Pellets for neutron diffraction were prepared by uniaxially compacting powder in a 6.35 mm diameter floating die at a pressure of 620 MPa, resulting in pellets that ranged from 7.5 to10 mm in length. Die wall lubrication with Lico wax C was used during pressing.

3.5.2 *Experimental Setup*

The Neutron Diffraction (ND) experiments were performed during two visits to the Canadian Neutron Beam Centre located in the NRU reactor of Canadian Nuclear Laboratories, Canada. Sintering was carried out in a top-loading vacuum furnace ($\sim 10^{-6} - 10^{-7}$ mbar) on the C2 powder diffractometer. A monochromatic neutron beam with a nominal wavelength of 1.33 Å, generated using the (531) reflection of a silicon single crystal monochromator, was directed at three to four powder pellets stacked end to end and contained in a Mo (1st visit) or V (2nd visit) crucible. The inside walls of all the crucibles used were coated with a thin layer of yttria paint (*Y Aerosol*, ZYP Coatings Inc.) to prevent the samples from reacting with the crucible. Two thermocouples were used in the experiments. A control thermocouple located outside the crucible was used to control the furnace temperature ($T_{CONTROL}$), while a sample thermocouple, located inside the crucible and in close proximity to the pellets, measured the sample temperature (T_{SAMPLE}). Both the control and sample thermocouple temperatures were logged during the experiments. The furnace temperature was controlled based on the feedback from the external control thermocouple rather than the internal thermocouple, because the latter

reacts strongly to large thermal events occurring in the samples during heating (i.e. melting or thermal explosion, as Ni-Ti is prone to do), leading to sharp variations in the feedback to the furnace controller which would in turn lead to poor temperature control. The diffracted neutrons entered an 800-element detector bank covering a scattering angle range of 80° *2θ,* from 15° to 95°*2θ* at a resolution of 0.1°. Pictures and schematics of the experimental setup are presented in Figure 3-1.
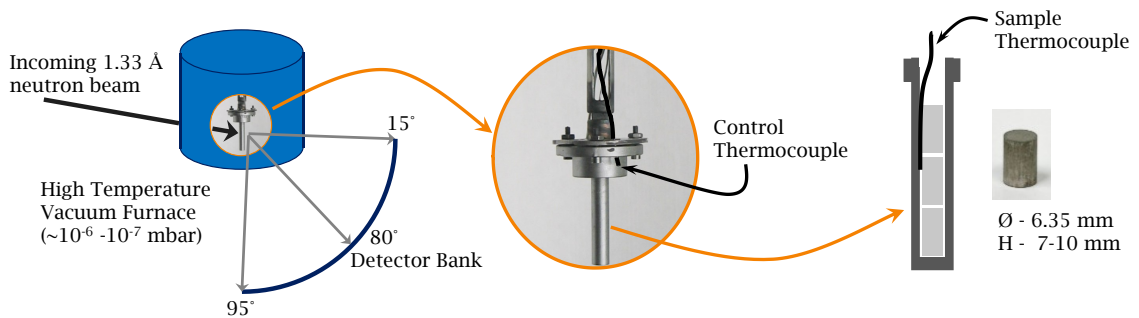
Figure 3-1   Schematic of the experimental setup

3.5.3   *Sintering and data collection*

Two *in-situ* ND sintering profiles were used on the 49 at% Ni mixtures. The first involved heating at 18°C/min to 500°C, then heat to 1000°C at 2°C/min, hold 4 hr at 1000°C and furnace-cool (referred to as *RS1000*). This thermal profile was exclusively used on the LP mixture. The second thermal profile (termed *RS1200*) was used on all four 49 at% Ni mixtures. It involved heating at 18°C/min to 500°C, then heating to 1200°C at 2°C/min, holding 15 min at 1200°C and furnace cooled.

The diffraction patterns from *in-situ* reactive sintering of the elemental powder mixtures are complicated due to the presence of multiple phases (i.e. Ti_2Ni, $NiTi$ and Ni_3Ti), the α-

Ti to β-Ti phase transformation, and the fact that the starting pure Ti and Ni evolve into solid solutions due to inter-diffusion. All these events occur at elevated temperatures at which crystallographic information is not readily available in the literature. Therefore, to aid in the analysis, four more ND runs were performed to obtain a baseline for each of the component phases:

1) Heat an empty Mo crucible to 1200°C at 2°C/min, hold 15 min at 1200°C, then furnace cool (*Mo1200*). These measurements provided a baseline for the diffraction patterns as well as the temperature profile.

2) Heat two elemental Ti pellets and two elemental Ni pellets together in the same V crucible to a peak temperature of 1000°C at 2°C/min with various holds during heat-up and cool-down (*El Ni/El Ti*). The Ni and Ti pellets were separated by an yttria-painted V foil to prevent them reacting.

3) Heat the 95Ti/5Ni mixture in a V crucible (*95Ti/5Ni*). This experiment was used to better understand the 765°C eutectoid transformation and the effect of Ni on β-Ti(Ni). The specimens were heated to 1000°C at 5°C/min, with holds at several temperatures above and below 765°C and at the peak temperature.

4) Heat two pellets of the Ti_2Ni mixture and two pellets of the Ni_3Ti mixture in the same V crucible to 950°C at a heating rate of 2°C/min (*Ti₂Ni/Ni₃Ti*). The two phases were separated by a yttria-painted V foil. The Ti_2Ni mixture and Ni_3Ti mixture pellets were the only pellets presintered at Dalhousie University prior to the ND experiments.

An overview of the neutron diffraction experiments is presented in Table 3-3.

Table 3-3   Overview of the neutron diffraction experiments

ND run	Pellets	Sintering	sintering profile	Crucible
HP mixture	4x HP mixture	*in-situ* reactive	500 to 1200 °C @ 2 kpm	Mo
LP mixture (RS1000)	4x LP mixture	*in-situ* reactive	500 to 1000 °C @ 2 kpm hold 4 hours	Mo
LP mixture (RS1200)	4x LP mixture	*in-situ* reactive	500 to 1200 °C @ 2 kpm	Mo
RA mixture	3x RA mixture	*in-situ* reactive	500 to 1200 °C @ 2 kpm	Mo
CNi mixture	3x CNi mixture	*in-situ* reactive	500 to 1200 °C @ 2 kpm	Mo
Mo1200	empty		500 to 1200 °C @ 2 kpm	Mo
El Ni/El Ti	2x F Ni - 2x HP Ti	*in-situ*	heat to 1000 °C @ 2 kpm with holds	V
95Ti/5Ni	4x 95Ti/5Ni mixture	*in-situ* reactive	heat to 1000 °C @ 5 kpm with holds	V
Ti2Ni/Ni3Ti	2x Ti2Ni - 2x Ni3Ti	pre-sintered	heat to 950 °C @ 2 kpm	V

Diffraction patterns were acquired at room temperature prior to heating, during the 2°C/min ramps, during the temperature holds, and during cooling. The neutron flux from the reactor varied with time. To ensure consistent counting statistics across all the diffraction patterns for a given sample, each acquisition continued until a fixed number of neutrons impinged on the sample, as determined by a low efficiency neutron detector placed between the incident neutron beam and the specimen. When the number of neutrons entering the low efficiency detector reached a pre-set value, the diffraction pattern was recorded. The pre-set value used, resulted in an acquisition time of ~2.5 minutes per pattern, corresponding to a temperature range of ~5°C for each pattern during a ramp.

The neutron diffraction experiments resulted in a vast amount of data. The methods of analysis are presented and discussed in Chapter 4.

CHAPTER 4
RESULTS AND DISCUSSIONS

4.1 POWDER CHARACTERIZATION

4.1.1 *Elemental powders*

SEM images of the elemental powders are shown in Figure 4-1. The morphologies of the three Ti (Figure 4-1 a-c) powders are very similar, showing flat faced angular particles typical of an HDH Ti powder. The LP and HP Ti powders are close in size (the goal behind sieving them) appearing with an almost identical powder size distribution. They are significantly smaller than the RA Ti powder. Table 4-1 lists the D_{50} (representing the median powder size of the cumulative powder size distribution) of the sieved elemental powders used as measured by laser particle analysis. At 101.5 µm the D_{50} of the RA Ti is larger than the mesh size used in sieving. The D_{50} of the HP Ti is 7.5 µm larger than the D_{50} for the LP Ti (36 µm vs. 28.5 µm).There is a larger disparity between the size of the F Ni powder (Figure 4-1 d) and the C Ni powder (Figure 4-1 e). The F Ni powder has a D_{50} of 10.5 µm but holds together well due to 'spikey' nature of the powders common to the carbonyl process. The C Ni powder shows an uneven surface but the particles are essentially spherical. The C Ni was too heavy for the Malvern to properly analyze, however based on SEM analysis the C Ni has an average diameter just below 100 µm.
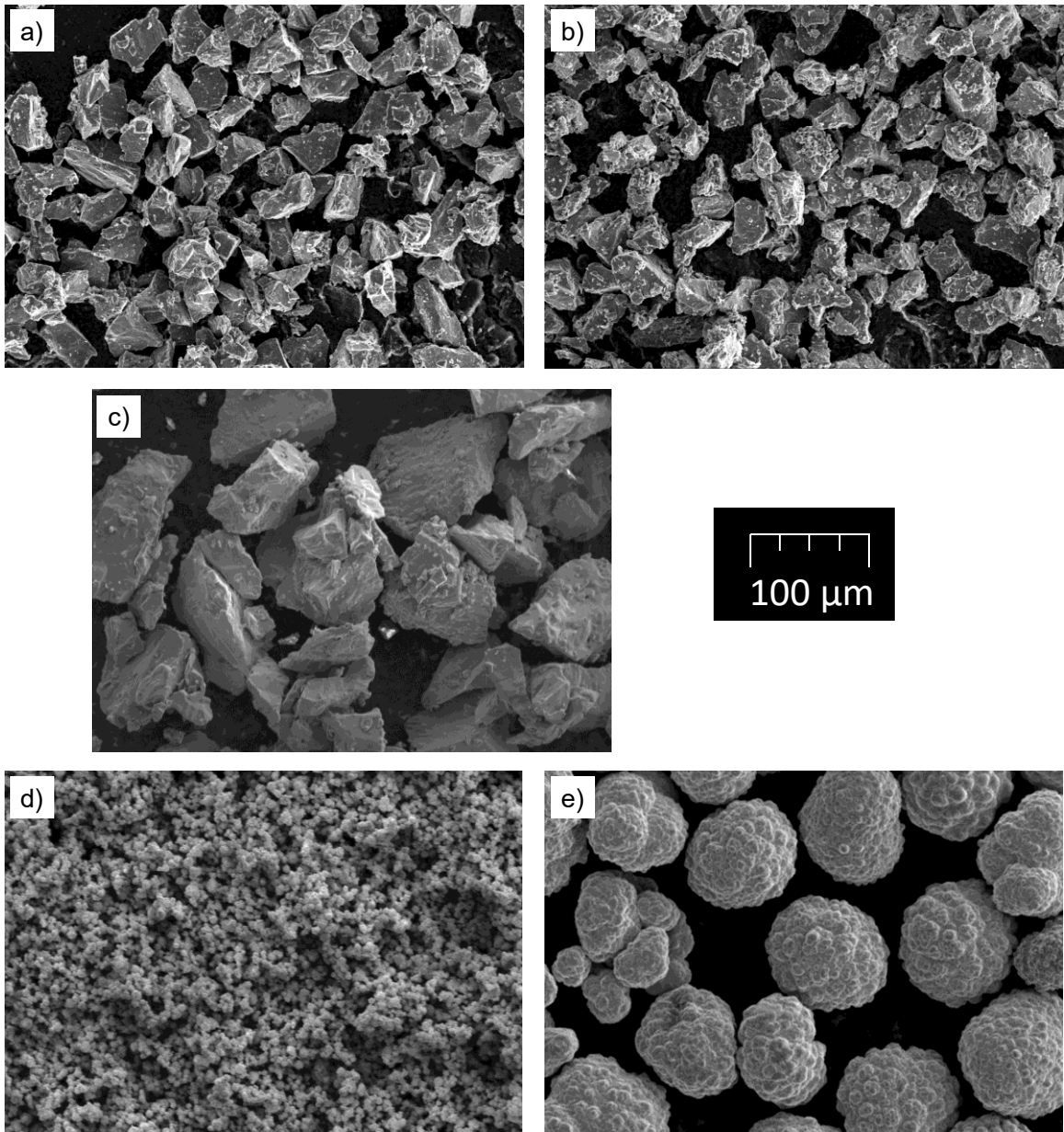
Figure 4-1   Elemental powder morphology from SEM micrographs of: a) LP Ti, b) HP Ti, c) RA Ti, d) F Ni and 3) C Ni

Apparent density values for the sieved elemental powders are also given in Table 4-1, along with % relative (or % theoretical) density based on theoretical densities of 8.9 and 4.51 g/ml for Ni and Ti, respectively. Of the Ti powders the RA CP Ti has the highest apparent density. Then the HP Ti followed closely by the LP Ti. . This is an expected

result since it is common for larger powders to have higher apparent densities. The fine

Ni powders have a very low apparent density. This can be explained by their size and

production route. Ni powders produced by thermal decomposition are generally 'spiky'

and have a high surface area. The coarse Ni powders have a high apparent density. This is

due to their size but also their near spherical morphology.

Table 4-1   **Elemental powder size (D_{50}) and apparent density (in g/ml and relative density – $\rho_{relative}$)**

	Powders				
	LP Ti	HP Ti	RA Ti	F Ni	C Ni
D_{50} (µm)	28.5	36.0	101.5	10.5	N/A
g/ml	1.32	1.40	1.68	2.39	4.46
$\rho_{relative}$ (%)	29.2	31.0	37.4	26.9	50.1

The full powder size distribution (PSD) for the three Ti powders and the F Ni powder is

presented graphically in Figure 4-2. All three Ti powders have narrow distributions, a

consequence of sieving. The LP and HP Ti powder distributions are close together with

the HP Ti powder being slightly larger. The LP Ti powder distribution broadens out at the

low end of the powder size. Indicating more of the fines could have been sieved out. The

SEM images infer powder size distributions closer than what is measured using the

Malvern. This is likely due to the difficulty in measuring oblong/not spherical particles

accurately. As expected from the SEM images and the D_{50} the RA Ti PSD is shifted

significantly to larger sizes than the two smaller Ti powders. The F Ni powder has a

broad PSD. This is a consequence of not sieving and the 'spiky' nature of the powder

which can cause agglomeration of multiple particles.
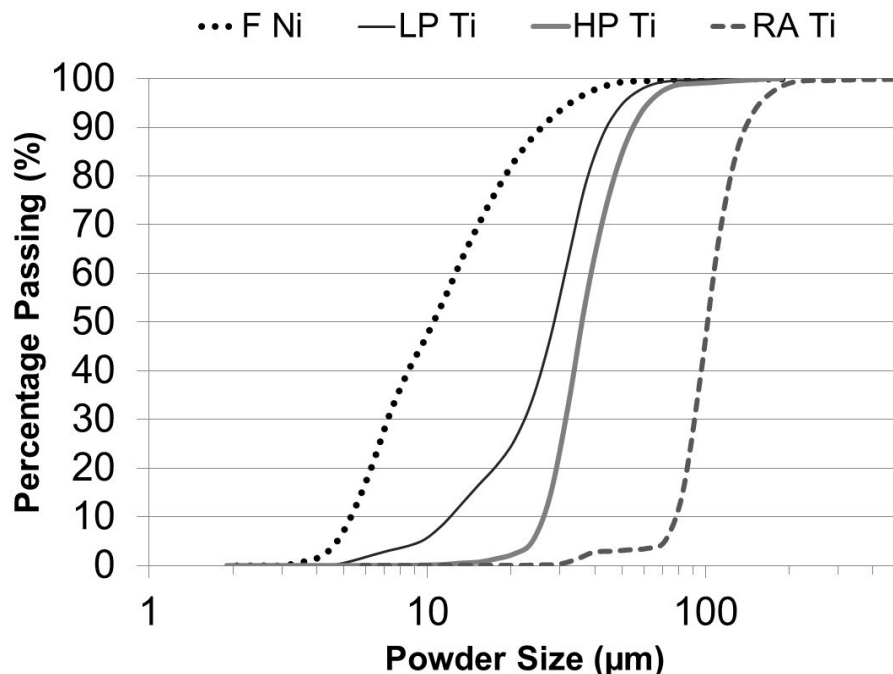
Figure 4-2   **Powder size distribution of the sieved elemental powders. C Ni was too heavy to accurately determine a PSD using the Malvern Master Particle Sizer**

The results of the chemical analysis on the elemental powders are listed in Table 4-2. The RA Ti has the lowest oxygen content followed by the AA HP Ti and then the AA LP Ti powders. Based on the ASTM designation the RA Ti is a grade 1. The hydrogen content of the LP and HP Ti powders is higher than the acceptable limit for any of the ASTM designations for commercially pure (CP) Ti (grades 1 to 4). The excess hydrogen is likely due to the powders not being fully de-hydrided during powder production. Discounting the hydrogen, the HP Ti is grade 3 while the LP Ti does not fit into any designation (too much oxygen). The LP Ti has 6.5 times more Fe and 3.5 times more Ni than the HP Ti. For the other metallic elements, this ratio falls between 1.5 and 2. The F Ni contains more oxygen and C than the C Ni powders, the latter a by-product of the carbonyl process. Otherwise the two Ni powders have similar levels of contaminants.

Table 4-2   Chemical analysis of the elemental powders

in wt%	LP Ti	HP Ti	RA Ti	F Ni	C Ni
H	0.0330	0.0250	0.0130	0.0070	0.0099
C	0.0140	0.0040	0.0080	0.0730	0.0060
O	0.7000	0.2700	0.1630	0.1300	0.0970
N	0.0230	0.0120	0.0180	0.0030	0.0088
Al	0.0133	0.0083	<10	0.0017	0.0045
Fe	0.0534	0.0077	0.0391	0.0079	0.0140
Mg	0.0044	0.0018	0.0004	0.0040	0.0048
Na	0.0126	0.0078	0.1219	0.0818	0.0744
Ni	0.0142	0.0036	<10	N/A	N/A

Based on the elemental powder characterization the LP Ti and the HP Ti have similar sizes but vary in their purity levels. The HP Ti and the RA Ti vary in their powder size but have similar purity levels.

4.1.2 *Powder Mixtures*

The apparent density results of the elemental pure powders as well as the powder blends are listed in Table 4-3. The % relative (or % theoretical) density used for the powder mixtures was calculated using the rule of mixtures with 49 at% Ni (54.08 wt%) based on theoretical densities of 8.9 and 4.51 g/ml for Ni and Ti, respectively. The CNi mixture could not be measured due to insufficient powders. Similar to the case of elemental powders the RA mixture has the largest apparent density followed by the HP mixture and closely behind that the LP mixture. In all three powder mixtures the apparent density has been lowered compared to the elemental Ti powders apparent densities.

Table 4-3   Powder mixture apparent density (in g/ml and relative density – $\rho_{relative}$)

	Powders			
	LP Mixture	HP mixture	RA mixture	CNi mixture
g/ml	1.80	1.84	2.25	N/A
$\rho_{relative}$ (%)	26.2	26.7	36.2	N/A

The LP, HP and RA mixtures were compacted over a range of pressures. A graph showing the relative densities of the three mixtures is presented in Figure 4-3. All three powders behave in a similar manner. The RA CP blend shows a slightly higher relative density at lower compaction pressures potentially owing to its higher apparent density. The LP mixture and the HP mixture show very little difference through the range of compaction pressures.
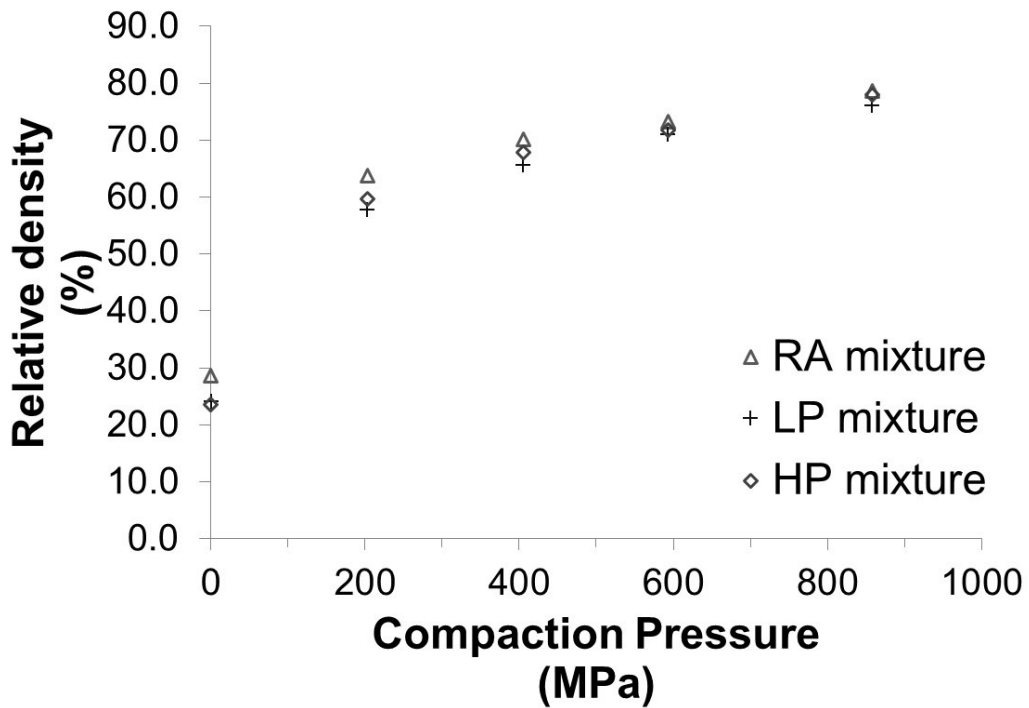
Figure 4-3   Compaction curve for the RA, LP and HP mixture

The green microstructures of the two mixtures pressed at 860 MPa are presented in Figure 4-4. The dark gray phase is Ti and the light gray phase is Ni. From the micrographs the much larger scale of the RA mixture and the CNi mixtures over the LP and HP mixtures is evident. The Ti and Ni sizes, pore distributions, morphologies, and dimensions are similar between the LP and HP mixtures, thus any differences in sintering behavior in these two samples are thought to be due the difference in Ti powder purities. The RA mixture and the CNi mixture will have significantly longer diffusion distances and different volume to surface area ratios changing the ability and speed at which Ti and Ni diffuse therefore affecting intermetallic formation.
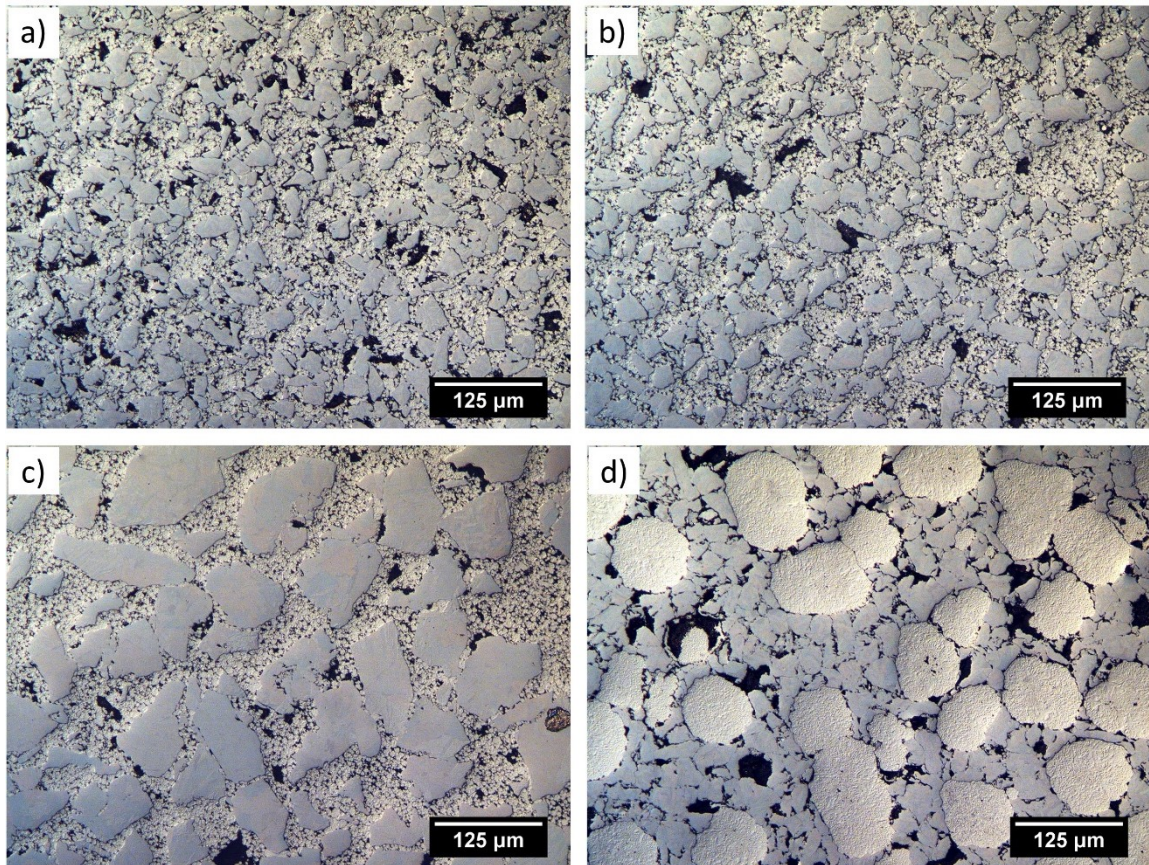
Figure 4-4   **Green microstructures for the LP mixture (a), HP mixture (b), RA mixture (c) and CNi mixture (d)**

4.2   NEUTRON DIFFRACTION TEMPERATURE VERIFICATION

To establish confidence in the sample temperature measured during the neutron diffraction experiments, the reverse eutectoid transformation (α-Ti + Ti$_2$Ni$\rightarrow\beta$-Ti) and the thermal explosion mode of self-propagating high-temperature synthesis (TE-SHS) were used as internal standards. The reverse eutectoid transformation occurs at 765 °C [7] in the α-Ti – Ti$_2$Ni interfacial layers resulting in the formation of β-Ti. TE-SHS occurs due to the incipient melting of the β-Ti – Ti$_2$Ni interface [32] at the Ti-rich eutectic. This generally occurs at 942 °C but can occur later if the quantity of liquid is not sufficient to onset self-propagation [33]. Both the reverse eutectoid reaction and TE-SHS are affected by the extent of solid state diffusion therefore some experiments may only show one event for temperature verification. Further discussions on the effect of solid state diffusion is provided later in this chapter.

For the molybdenum crucibles, differential thermal (DT) traces were produced by plotting $\Delta T_{Mixture} - \Delta T_{Mo}$ vs $T_{CONTROL}$, where $\Delta T = T_{SAMPLE}$-$T_{CONTROL}$, thereby accounting for the behaviour of the crucible. For samples contained in V crucibles (T_{SAMPLE}-$T_{CONTROL}$)$_{Mixture}$ was plotted vs $T_{CONTROL}$, since no separate experiments were performed with a V crucible alone.

The resulting differential thermal traces for *RS1000* and *RS1200* heating profiles of the LP mixture, as well as an LP mixture Differential Scattering Calorimetry (DSC) trace are presented in Figure 4-5. For the LP mixture only the reverse eutectoid reaction is used for temperature verification as heating the LP mixture at 2 °C/min does not result in a TE-SHS event. There is good agreement (less than 3°C difference in onset temperatures)

62

between the calibrated DSC trace and the ND 'DTA' traces, confirming the accuracy of the temperature measurement.
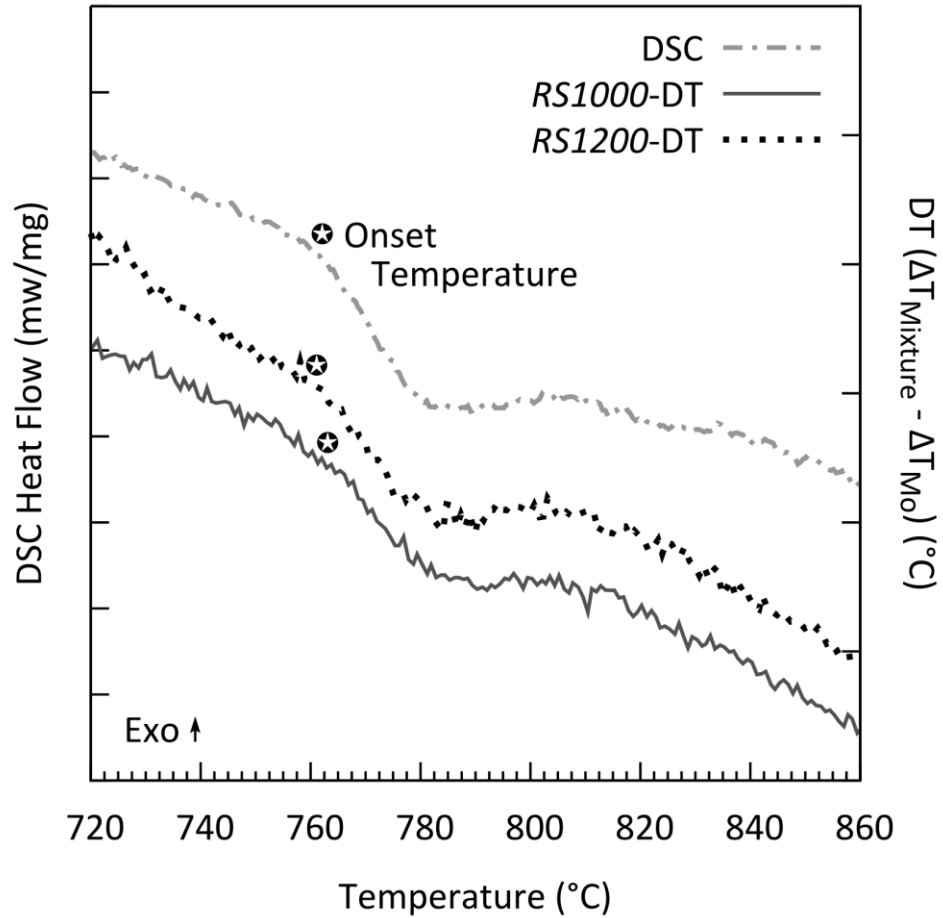
Figure 4-5   *LP mixture* **temperature verification: neutron Differential Thermal (DT) traces for *RS1000* and *RS1200* vs DSC trace**

Similar to the LP mixture the HP mixture does not show a TE SHS event when heated at 2 °C/min. The DT trace and the DSC trace of the HP mixture show reverse eutectoid onset temperatures within 2 °C (Figure 4-6). This provides further confirmation of the temperature accuracy in the Mo crucible ND experiments.
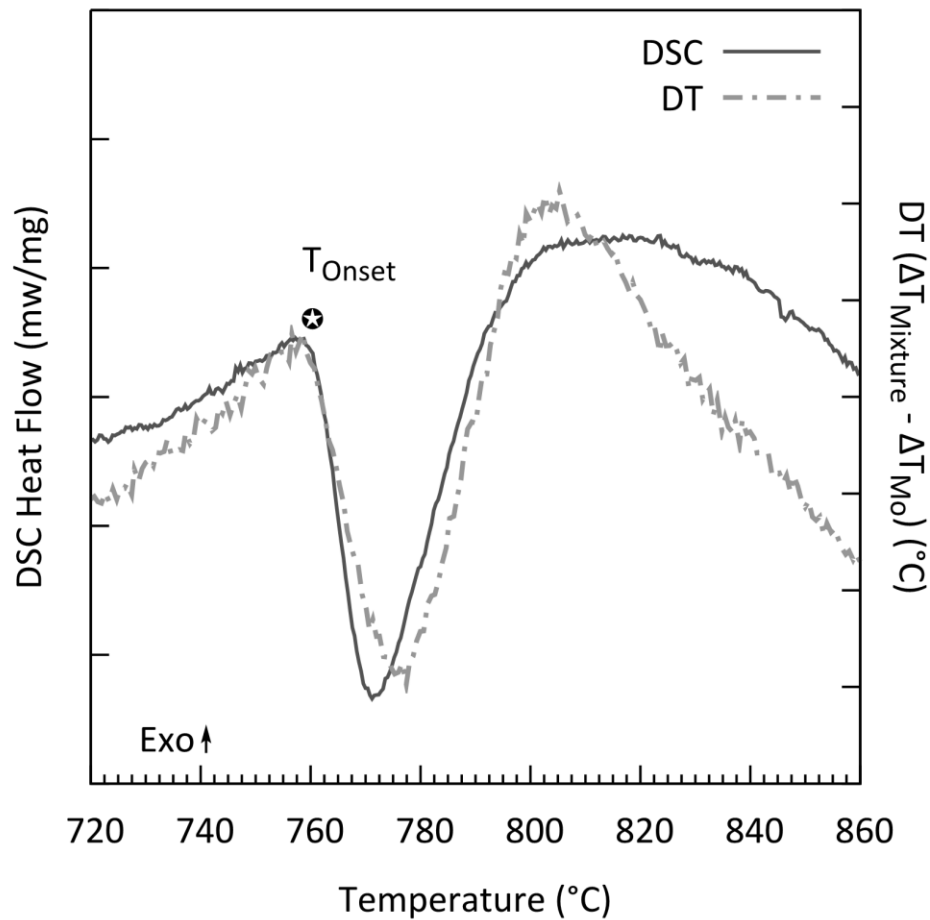
Figure 4-6   *HP mixture* **temperature verification: neutron Differential Thermal (DT) traces vs DSC trace**

The RA mixture undergoes both a reverse eutectoid and TE-SHS (Figure 4-7). This allows for temperature verification over a broader range of temperatures. The reverse eutectoid shows good agreement at the lower temperatures with an ND DT onset of 759 °C vs 758 °C for the DSC trace. The high temperature agreement is equally as good with an onset of 942 °C vs 944 °C for the ND DT trace and DSC trace respectively. The DT trace also provides a measure of sample heating due to TE-SHS. The sample was heated by approximately 63 °C above the nominal furnace temperature of 947 °C.
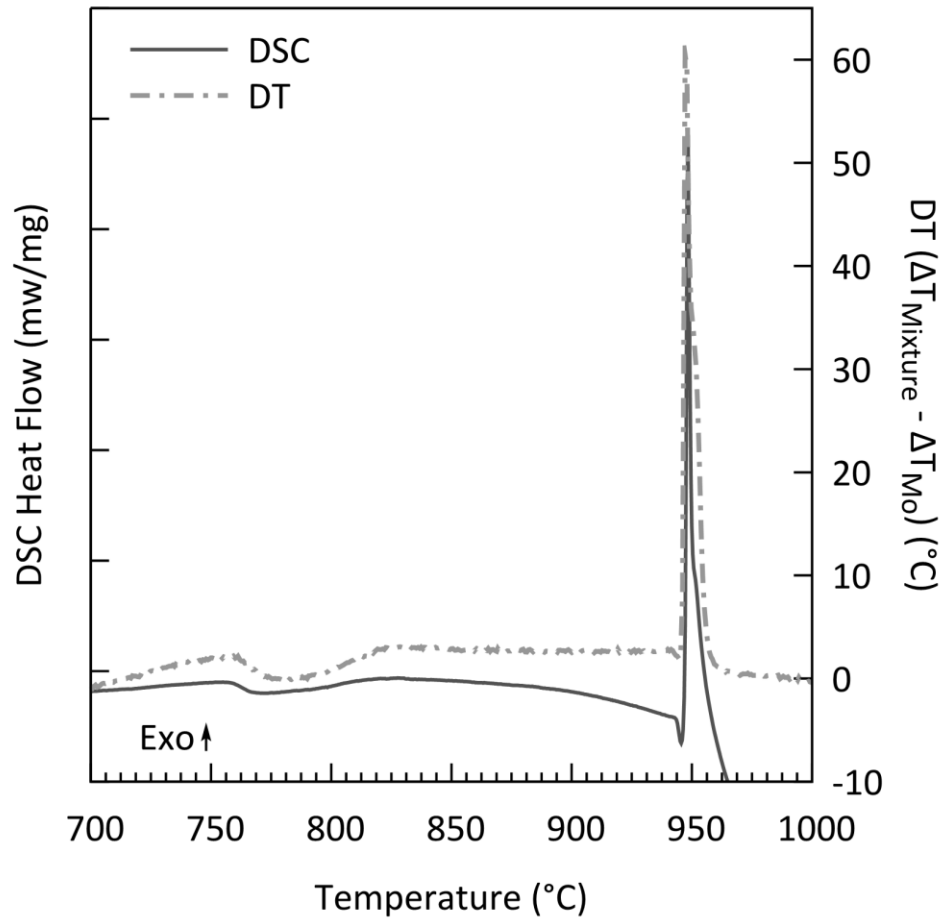
Figure 4-7 *RA mixture* **temperature verification: neutron Differential Thermal (DT) traces vs DSC trace**

The CNi mixture undergoes a minimal reverse eutectoid reaction but a significant TE-SHS reaction (Figure 4-8). Only the TE-SHS peak is evaluated for accuracy. The TE-SHS onset temperature of the ND DT sample was 955 °C while the DSC recorded an onset of 954 °C. Prior work with the CNi mixture indicated significant melting. To avoid liquid thermocouple interaction the thermocouple was raised from the middle of the sample to the top of the sample. Thus once significant melting occurs it is expected that the specimen will slump increasing the distance between sample and thermocouple and reducing the temperature accuracy. The heating of the specimen due to TE-SHS is more

65

significant in the CNi mixture than the RA mixture with a sample temperature increase of approximately 143 °C over the nominal furnace temperature of 958 °C. This value is thought to be low due to the aforementioned issue with the thermocouple.
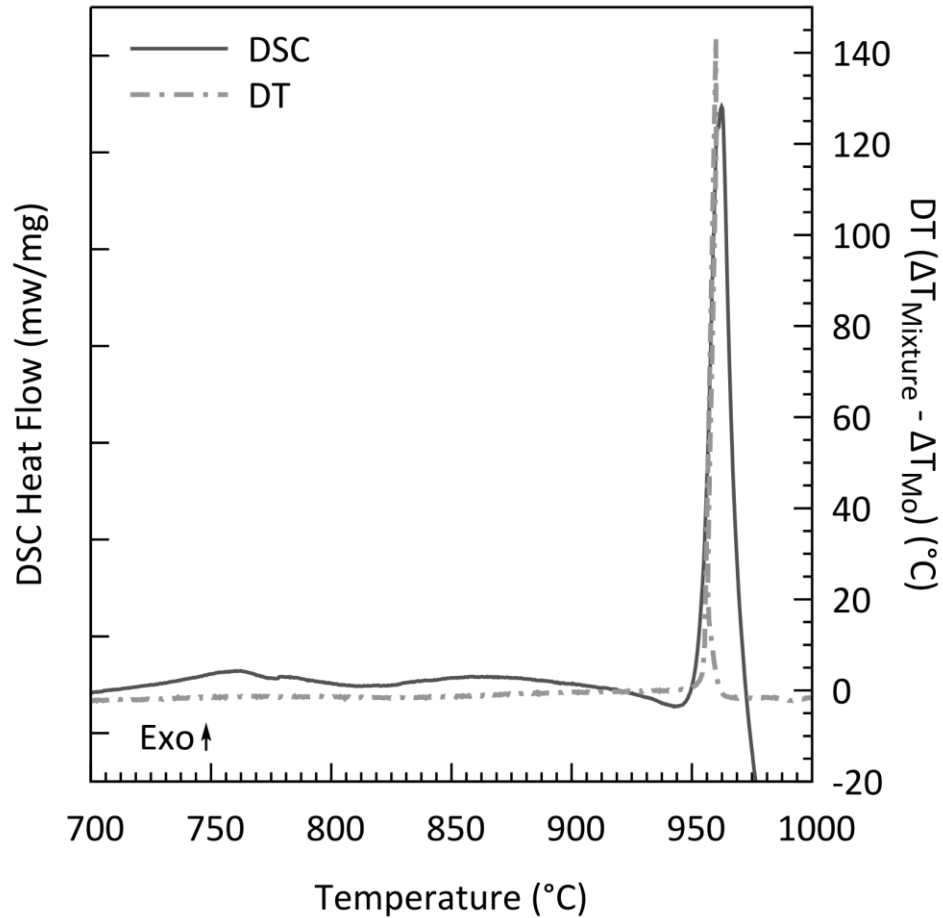
Figure 4-8   *CNi mixture* **temperature verification: neutron Differential Thermal (DT) traces vs DSC trace**

The five ND experiments using Mo crucibles all showed very good agreement in the onset temperatures measured using a calibrated DSC and the ND DT traces. The intrinsic thermal events in the samples allowed for the determination of temperature accuracy at approximately 760 °C and 950 °C.

Three experiments were conducted using vanadium crucibles. The *Ti₂Ni/Ni₃Ti* experiment had no thermal event that could be used to verify the temperature. The holds in *El Ni/El Ti* near thermal events make comparison with DSC traces very difficult. Only the ND DT onset temperature of reverse eutectoid reaction in the *95Ti/5Ni* experiment was compared to the DSC trace. There was too little Ni in the *95Ti/5Ni* sample to undergo a TE-SHS reaction. While slightly higher than in the Mo crucibles there was still good agreement between the onset temperatures of the reverse eutectoid reaction with a positive shift of 5 °C in the ND DT trace. The significantly higher onset temperatures in the *95Ti/5Ni* sample are thought to be due to the long 750 °C hold. The long hold is thought to allow Ti_2Ni to grow in size reducing the α-Ti to Ti_2Ni interface area to Ti_2Ni volume ratio. This slows down the reverse eutectoid reaction which takes place at the α-Ti - Ti_2Ni interface.

Based on the results of the Mo crucible it is expected the results of the *95Ti/5Ni* experiment are representative of all three V crucible experiments.
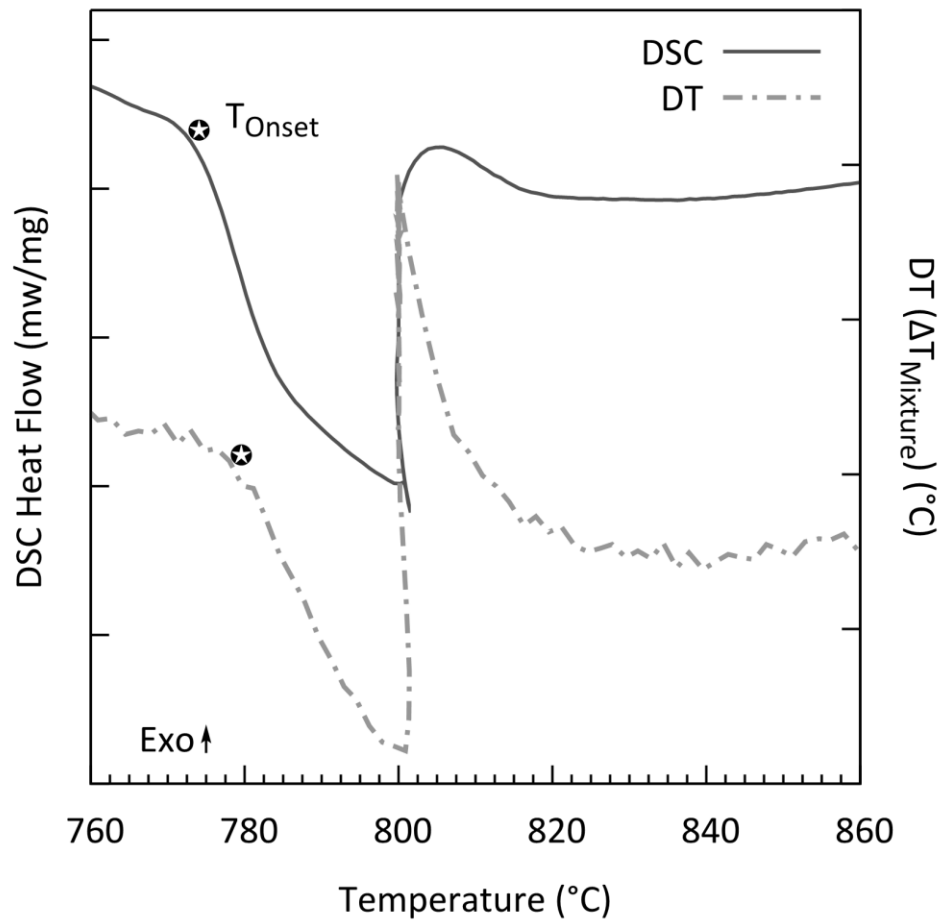
Figure 4-9   **Vanadium crucible temperature verification: neutron Differential Thermal (DT) traces vs DSC trace for _95Ti/5Ni_**

4.3   PAPER 1: INVESTIGATING THE INFLUENCE OF TI POWDER PURITY ON PHASE EVOLUTION DURING NITI SINTERING USING IN SITU-NEUTRON DIFFRACTION

Authors: Dan Cluff, Stephen F. Corbin and Michael A. Gharghouri

Status of the paper: the paper has been submitted to _Intermetallics_ and is currently in the review process.

My contribution: I designed the experimental plan in collaboration with Dr. Stephen Corbin and Dr. Michael Gharghouri (neutron work only). All the specimen preparation and experimental work was performed by me with the exception of the powder size analysis and chemical composition (reported in 4.1), as well as the neutron diffraction where I assisted Dr. Michael Gharghouri at Chalk River Laboratories. I performed all of the data analysis and wrote the first draft of the manuscript. The current state of the manuscript is a result of editing and proof reading by all three authors.

Notes on editing for the thesis: To improve the flow of the thesis elements that repeat, what is discussed elsewhere have been removed. This includes the Introduction and the Acknowledgements. Portions of the Materials and Methods have been edited out, keeping only the information regarding powders used, naming conventions and sintering profiles discussed in the manuscript.

4.3.1 *Abstract*

The influence of Ti powder purity on phase evolution during the reactive sintering of elemental Ni and Ti powders to form NiTi was studied using differential scanning calorimetry (DSC) and in-situ neutron diffraction. Reaction between the Ni and Ti is not significant until 600 °C. From 600 to 700 °C, Ti_2Ni forms in mixtures made from high (HP) and low purity (LP) Ti powder. The Ni_3Ti phase also grows in this temperature range in the LP mixture. The most significant phase evolution takes place between 700 and 920 °C. The α to β phase transformation in (Ti) begins at the eutectoid temperature (765 °C) and ends at 820 °C. The highest growth rates for all three intermetallic phases, including NiTi, and the decay rate of the elemental Ni occur in this temperature range. At

approximately 1000 °C, all reactants are consumed and homogenisation occurs, with NiTi continuing to grow at the expense of the other intermetallic phases. The Ti rich intermetallic phase persists above its melting point, due to the formation of a solid-solution with oxygen (i.e. $Ti_2Ni(O)$). From 1100 to 1200 °C, the microstructure becomes a stable mixture of NiTi with a small fraction of $Ti_2Ni(O)$. The phase evolution is similar in the LP and HP mixtures. However, the rate of reaction is higher in the LP mixture due to the influence of impurities (O, Fe and Ni) on the diffusivities in the many phases involved.

4.3.2 *Materials and Methods (edited)*

One Ni powder (F Ni) and two Ti powders (LP Ti and HP Ti) were used. The elemental powders were mixed to a composition of 51 at% Ti - 49 at% Ni, resulting in 2 different powder mixtures: an LP Ti - F Ni mixture (*LP mixture*) and an HP Ti - F Ni mixture (*HP mixture*). The mixtures were subsequently dry milled for 2 hours in a glass jar.

Specimens for DSC were prepared by uniaxially compacting the powders into 4.76-mm diameter discs using a die. Compaction pressures of 430 and 860 MPa were used. Sintering of the powder compacts was performed in a Netzsch 404 F1 high temperature differential scanning calorimeter under a high purity Ar atmosphere. Three thermal profiles were used: (1) heating to 1050 °C at 20 °C/min, (2) heating to 940 °C at 20 °C/min and (3) heating to 500 °C at 20 °C/min, followed by heating to 1200 °C at 2 °C/min. Cooling from peak temperature was performed at 40 °C/min in all cases. The three temperature profiles were applied to a variety of compaction pressure/powder

mixture combinations. These profiles were used in order to determine the influence of heating rate and peak temperature on sintering behaviour.

Pellets for neutron diffraction were prepared by uniaxially compacting 1 g of powder in a 6.35 mm diameter die at a pressure of 620 MPa, resulting in pellets approximately 7.5 mm in length. The specimens were sintered by heating at 18°C/min to 500°C, followed by heating to 1200°C at 2°C/min, and then cooling to room temperature (*RS1200*).

4.3.3 *Results and Discussion*

4.3.3.1 DSC

4.3.3.1.1 Sintering at 20 °C/min

Elemental LP Ti and HP Ti powders as well as the LP and HP mixtures were pressed to 860 MPa and sintered in the DSC by heating up to 1050 °C at 20 °C/min. The resulting DSC heat-up traces are shown in Figure 4-10. For the elemental powders, the trace is flat up to approximately 880 °C, upon which an endothermic event takes place (see inset Figure 4-10). This endothermic event corresponds to the α-Ti $\rightarrow$ β-Ti allotropic phase transition. The onset of this transition occurs at 876 °C and 883 °C in the LP Ti and HP Ti powders, respectively. Transition temperatures obtained from the DSC are considered to have an uncertainty on the order of 2°C. The endothermic peak in the DSC trace spans a broader temperature range in the LP Ti powder than in the HP Ti powder. The transformation end temperatures are approximately 1050 °C and 950 °C in the LP and HP powders, respectively. The compositional differences between the two elemental powders (mainly oxygen, iron, nickel and aluminum) are most likely at the root of the differences

in the α-Ti $\rightarrow$ β-Ti phase transition behavior evident in Figure 4-10. The lower start temperature in the LP Ti powder is due to the higher concentrations of Ni and Fe, both of which are β-Ti stabilizers, while the higher end temperature is due to the alpha stabilizing effects of Al and O. The HP Ti powder shows a much sharper and narrower peak due to higher chemical purity. The LP and HP mixtures behave similarly to the elemental Ti powders until approximately 600 °C, at which point the traces start shifting upward in the exothermic direction. The trace of the HP mixture increases slowly until approximately 725 °C, at which point it starts to increase more rapidly. In this same interval, the trace of the LP mixture increases steadily at a much greater rate than in the HP mixture. An endothermic peak occurs in both powders at ~765 °C due to the reverse eutectoid reaction α-Ti(Ni) + Ti_2Ni $\rightarrow$ β-Ti(Ni) [32]. After the endothermic peak associated with this transformation, the trace of the LP mixture drifts downward steadily (endothermically) until about 942 °C, while the trace of the HP mixture is flat. For both specimens, at around 942 °C, a small endothermic peak precedes a larger exothermic peak. This exothermic peak is approximately 7 times larger for the HP mixture than for the LP mixture.
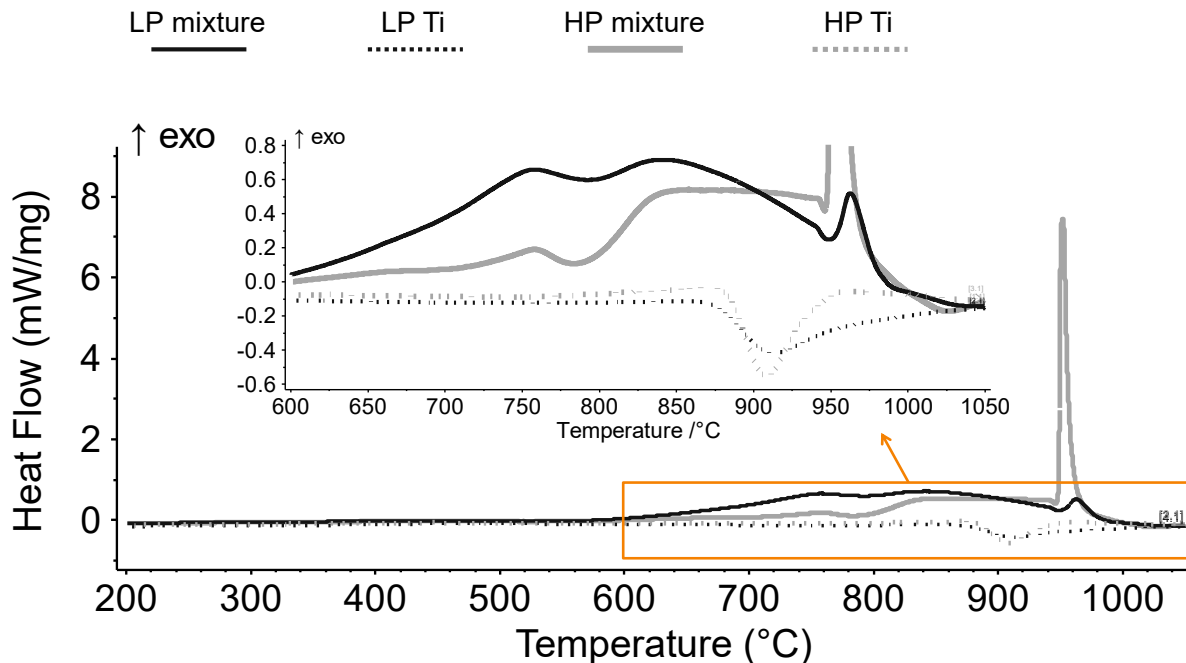
Figure 4-10 DSC heat up traces of the powder mixtures and the elemental Ti powders pressed at 860 MPa and heated to 1050 °C at 20 °C/min.

The differences between the DSC traces of the mixtures are largely attributable to the differences in the chemical compositions of the starting elemental Ti powders. Specifically, the exothermic shift in the DSC trace starting at 600 °C is likely due to the formation of intermetallic phases (Ti_2Ni, $NiTi$, and Ni_3Ti). The greater exothermic shift observed for the LP mixture up to ~750 °C indicates increased intermetallic phase formation compared to the HP mixture. The endothermic peak associated with the reverse eutectoid transformation (starting at 765 °C) occurs concurrently with the exothermic formation of the intermetallic phases. This peak is broader and shallower for the LP mixture than for the HP mixture, since less α-Ti(Ni) is available to take part due to the enhanced formation of intermetallic phases prior to 765 °C. With further heating, any unalloyed α-Ti remaining in the sample gradually transforms to β-Ti(Ni) up to 880 °C,

with continued growth of the intermetallic phases occurring in parallel. The traces of the LP and HP mixtures from 825 to 940 °C are different because the microstructural changes that occur depend on the purity of the Ti powder.

To investigate this phase progression further, LP and HP mixtures pressed to 430 MPa were heated in the DSC to 940 °C at 20 °C/min and immediately cooled to room temperature (see heating and cooling traces in Figure 4-11). The heating traces are similar to those of Figure 4-10, as expected. During cooling, the exothermic peak which has an onset at approximately 730 °C is due to the eutectoid transformation β-Ti(Ni) → α-Ti(Ni) + Ti$_2$Ni. The magnitude of this peak is a direct measure of how much β-Ti(Ni) remained unreacted at the end of the heating stage. The enthalpies of these peaks were found to be 1.9 and 9 J/g for the LP and HP mixtures, respectively. According to previous work, these values correspond to β-Ti(Ni) fractions of 3 and 14 wt% for the LP and HP mixtures, respectively [32], that were present at the end of heating. These results show that the rate of consumption of β-Ti(Ni) during heating due to the growth of intermetallic phases is slower in the HP mixture. Optical micrographs of the specimens cooled from 940 °C are shown in Figure 4-12. In these images, Regions I correspond to areas that were β-Ti(Ni) above 765 °C but underwent the eutectoid reaction during cooling from 940 °C. Consistent with the DSC results, a higher fraction of eutectoid is evident in the HP mixture. SEM-EDS analysis was used to confirm that Regions II consist of a layer of Ti$_2$Ni (surrounding Regions I) and a layer of NiTi (surrounding Regions III). Regions III correspond to Ni$_3$Ti and Ni. Previous work [112] has shown that changing the pressing pressure does not affect the trends observed in the DSC traces; however, a lower pressing pressure reduces the extent of solid state sintering more in the HP mixture than in the LP

mixture, which may increase the difference between the LP and HP mixtures with respect to the amount of β-Ti remaining at the end of heating compared to specimens pressed at 860 MPa.
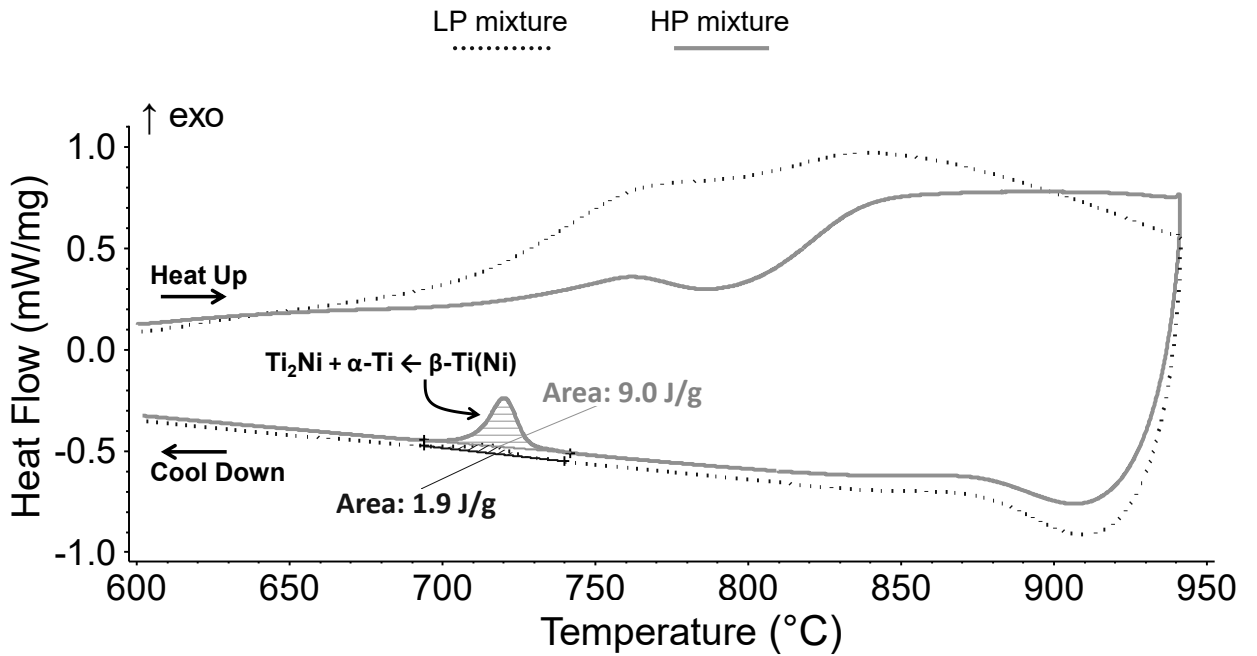
Figure 4-11   **DSC trace of the powder mixtures pressed at 430 MPa and heated to 940 °C at 20 °C/min.**
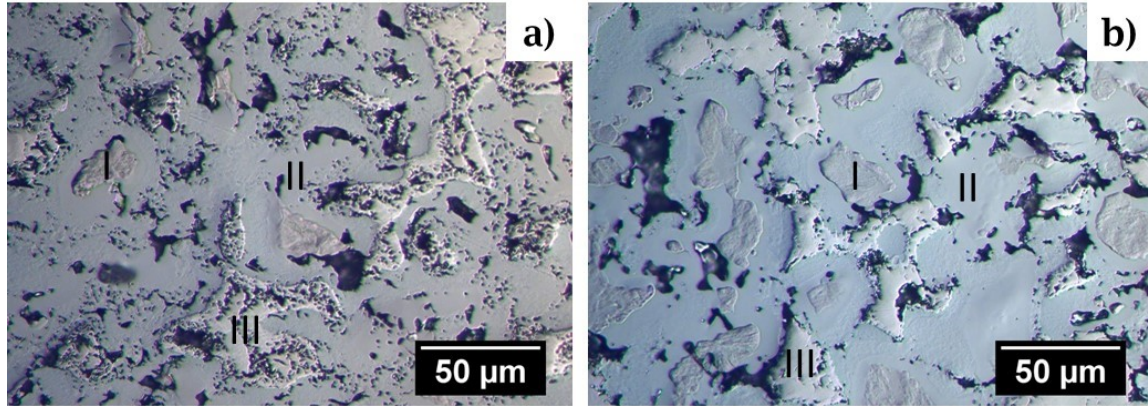
Figure 4-12   Optical micrographs of (a) the LP mixture and (b) the HP mixture pressed at 430 MPa, after heating to 940 °C at 20 °C/min. Region I – former sites of β-Ti(Ni), Region II- Ti2Ni and NiTi, Region III- Ni3Ti and (Ni).

Referring again to Figure 4-10, upon further heating above 940 °C, both powder mixtures exhibit a small endothermic dip starting at 942 °C, which is caused by melting of the β-Ti(Ni)-Ti$_2$Ni interface. This melting event leads to intimate contact between Ni and Ti atoms, resulting in the exothermic peak caused by the thermal explosion mode of self-propagating high temperature synthesis (TE-SHS) [33]. The magnitude of the exothermic TE-SHS event is significantly higher in the HP mixture. Biswas [46] concluded that the peak sample temperature reached due to TE-SHS varies with the amount of solid state diffusion and intermetallic phase formation that occurs prior to the TE-SHS event. Whitney *et al.* [32] have correlated the enthalpy of the TE-SHS exothermic event to the amount of β-Ti(Ni) present at the eutectic temperature. The higher the amount of β-Ti(Ni), the more energy is released during the TE-SHS event. The results of the present investigation are consistent with the findings of Biswas and Whitney *et al*: there is less eutectoid (Regions I) in the LP mixture than in the HP mixture (Figure 4-12), resulting in the smaller TE-SHS peak recorded for the LP mixture.

For the powder mixtures and heating profile used in the present investigation, the sample temperatures were not high enough to melt the interconnecting network of intermetallic phases, resulting in the porous and heterogeneous microstructures shown in Figure 4-13. The HP mixture has more and larger pores than the LP mixture, consistent with the larger exothermic TE-SHS peak measured in the DSC trace for the HP mixture (Figure 4-10). The higher porosity in the HP mixture is also consistent with the evidence of a higher quantity of β-Ti(Ni) available to melt prior to TE-SHS presented in Figure 4-11 and Figure 4-12.

Figure 4-13   Micrographs of the LP mixture (a - optical, b - SEM) and HP mixture (c - optical, d – SEM) after pressing at 860 MPa and heating to 1050 °C at 20 °C/min.

In the micrographs of Figure 4-13, the areas labelled Region I are Ti_2Ni. Regions IIa and IIb are both NiTi. Region IIa has less Ni (EDS indicates 49 to 50 at%) and is martensite at room temperature whereas Region IIb is richer in Ni (approximately 53 at% according to EDS) and is austenite. Region III is Ni_3Ti and region IV is Ni. The porosity presents a duplex nature: there are larger rounded pores surrounded by the Ti-rich phases (i.e. Regions I and IIa) and smaller, irregularly shaped pores with much higher surface area to volume ratios surrounded by Ni-rich phases (Regions IIb and III). The larger rounded pores are thought to be the result of the Ti-rich liquid phase being drawn off (drawn into finer pores due to capillary forces) during TE-SHS. The smaller pores are likely the result of solid state diffusion, which occurs due to an imbalance in the diffusion of the two elemental species (Kirkendall porosity): Ni diffuses much more rapidly into Ti than Ti diffuses into Ni [8,9]. Comparing the pores between the Ni particles in the green state (Figure 4-4) with the long irregular pores associated with solid state diffusion in Figure 4-13, it is suggested that the solid state pores are produced due to Ni using the inter-particle space as a diffusion pathway. There remain small isolated pores in the Ni, and surrounding the long irregular pores. These isolated pores originate from inside a Ni particle, again due to the diffusional imbalance of the elemental species. This small-scale porosity is far more apparent in the LP Ti mixture, again consistent with the increased solid state diffusion occurring in the LP Ti mixture compared to the HP Ti mixture.

4.3.3.1.2 Sintering at 2 °C/min

The previous section notes that TE-SHS must be avoided to produce a dense NiTi part with good dimensional stability. To this end, specimens were heated to 500 °C at 20 °C per minute (the temperature range over which the DSC trace is flat), then to 1200 °C at 2

°C/min. It was predicted that the slower heating rate would allow enough time for the powder mixtures to be free of any β-Ti(Ni) by 942 °C, thus avoiding melting and the TE-SHS event. The DSC traces recorded while heating to 1200 °C at 2 °C/min are not shown as only a small melting event at the eutectic temperature (942 °C) in the HP mixture was detected (an enthalpy of less than 1 J/g was determined). As expected at this slower heating rate, neither powder mixture showed the exothermic peak associated with TE-SHS. Figure 4-14 shows the scale of porosity in the two mixtures after sintering under this thermal profile. The LP mixture shows lower porosity levels than the HP mixture. Higher magnification images of the microstructures (Figure 4-15) reveal two important characteristics. The pore structure associated with solid state diffusion in the 20 °C/min heating rate experiments is again visible here. Also, two phases are left after the sintering treatment: a small amount of Ti_2Ni (I) scattered within region II (NiTi). Consequently this thermal profile produces a more homogeneous material than the 1050 °C, 20 °C/min profile.
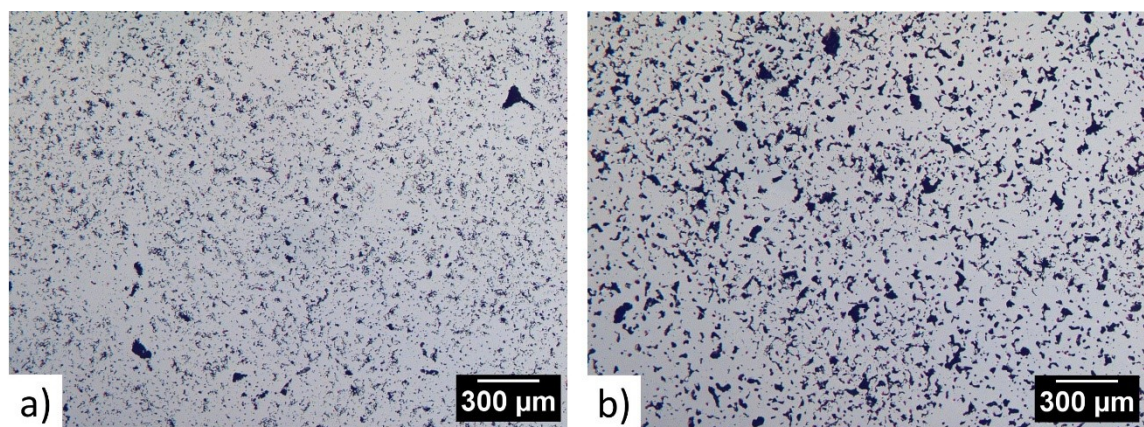
Figure 4-14   **Optical micrographs of the powder mixtures (a - LP mixture, b - HP mixture) after pressing at 860 MPa and heating to 1200 °C at 2 °C/min.**
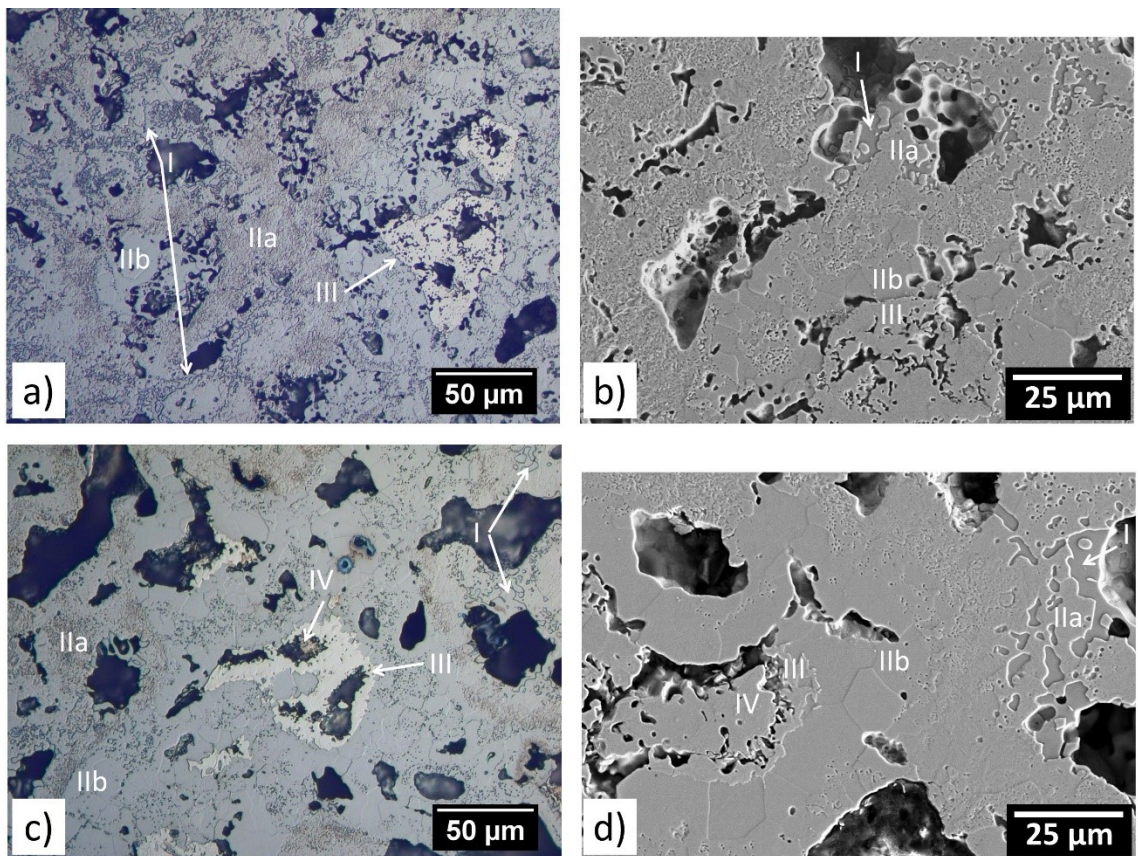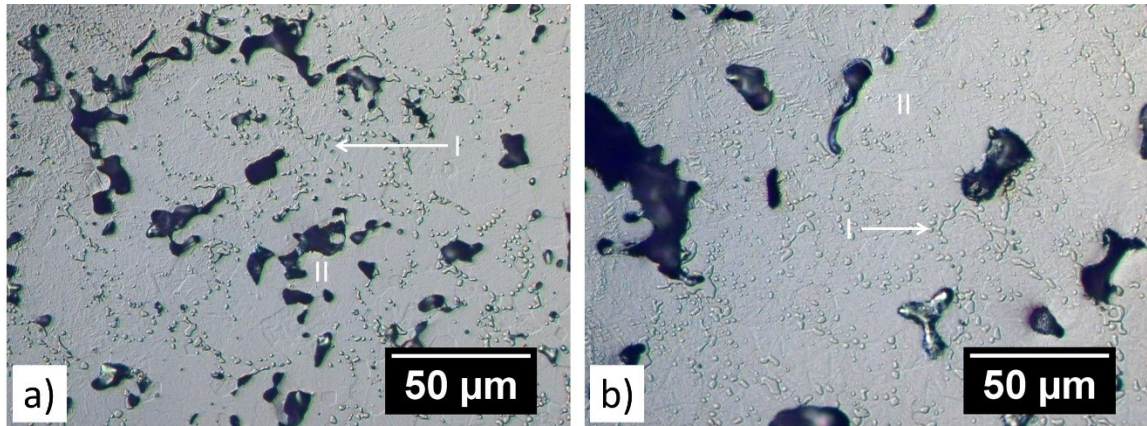
Figure 4-15   Optical micrographs of (a) the LP mixture and (b) the HP mixture after pressing at 860 MPa and heating to 1200 °C at 2 °C/min.

The more uniform pore distribution in the LP mixture is due to the lack of melting at the eutectic temperature, since the larger pores due to a drawn off liquid are not present. Unlike the LP mixture, much of the porosity in the HP mixture heated at 20 °C/min is due to liquid drawn off during the TE-SHS event. While TE-SHS was avoided, a small melting peak was observed. The liquid produced pores that, while still larger than in the LP mixture, are smaller and less rounded than those produced during TE-SHS. Zhang *et al.* [20] performed sintering trials which showed that a hold longer than 15 minutes at 1150 °C following a slow heat-up does little to increase density. This result implies that holding at 1200 °C will have little effect on the densities obtained for the LP and HP mixtures.

The presence of Ti_2Ni in the final product is expected, based on previous work and thermodynamic considerations. The powder mixtures contained 49 at% Ni, a composition just inside the Ti_2Ni + NiTi two-phase region of the phase diagram. Many other studies on NiTi [22,23,26,29] have shown that it is very difficult to completely remove the Ti_2Ni phase: it is typically assumed that the interstitial oxygen forms a stable Ti_4Ni_2O phase

whose crystal structure is very similar to that of Ti_2Ni. Bertheville *et al.* [25] confirmed the presence of Ti_4Ni_2O instead of residual Ti_2Ni at room temperature in their work by performing cell refinement on the XRD pattern they obtained. EDS performed on the specimens in the present investigation provides qualitative evidence of a much higher oxygen content in the Ti_2Ni phase than the phases surrounding it (see Figure 4-16 for the results from the LP mixture).
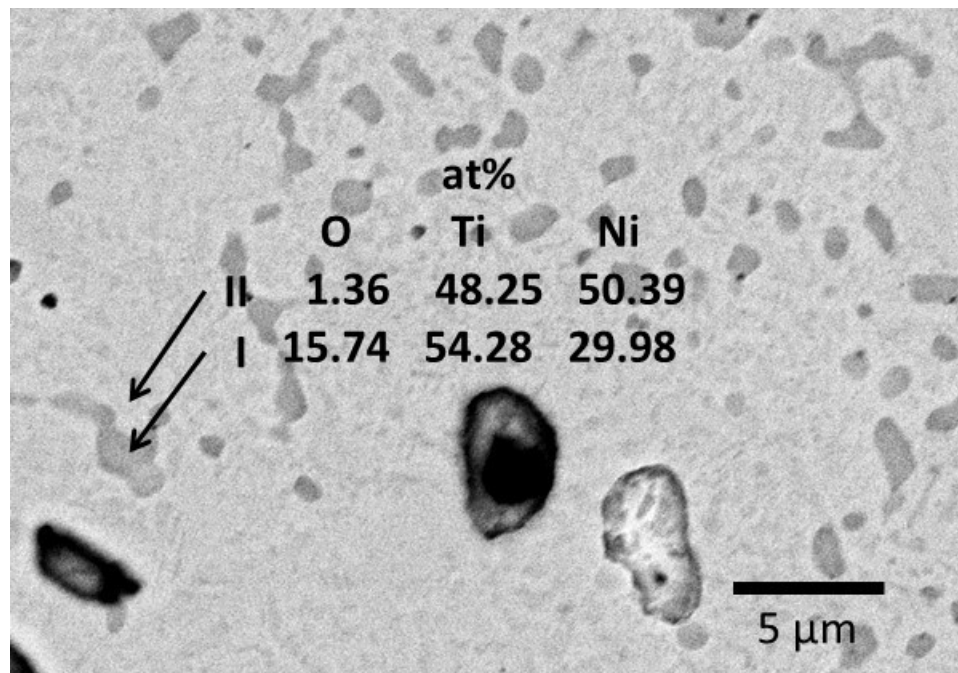
Figure 4-16 **Backscatter SEM image showing EDS results on the two phases present in the LP Ti mixture after DSC in situ sintering at 2 °C/min to 1200 °C. (I-Ti2Ni(O); II-NiTi)**

Given that both powder mixtures were subjected to the same heating profile and that the green microstructures (with respect to diffusion distances and the amount and shape of inter-particle pores) are also similar, the difference in the rate of intermetallic phase formation is thought to be mostly due to the differences in the chemical purities of the

elemental Ti powders. While DSC, complemented with post microstructural analysis, provides many useful insights, it does not provide information on the formation of the three intermetallic compounds (the products of the sintering process) and the consumption of the (Ti) and (Ni) phases (the reactants in the sintering process). This limitation is particularly evident for the slower heating rate of 2 °C/min, for which the DSC traces do not reveal any significant thermal events. In-situ neutron diffraction provides complementary information regarding start and stop temperatures for phase transitions, the crystal structures of the various phases present, quantitative measurements of the changes in the quantities of the various phases, and phase compositions.

4.3.3.2 Neutron Diffraction

The neutron diffraction data obtained from the in-situ experiments are presented as film plots for the LP and the HP mixtures in Figure 4-17 and Figure 4-18, respectively. Each horizontal line in a film plot corresponds to the complete diffraction pattern for a single temperature, with the neutron count for a given scattering angle displayed as a 256-level grayscale pixel, with black corresponding to the highest count. Peaks associated with the Mo crucibles have been removed from the figures for clarity.
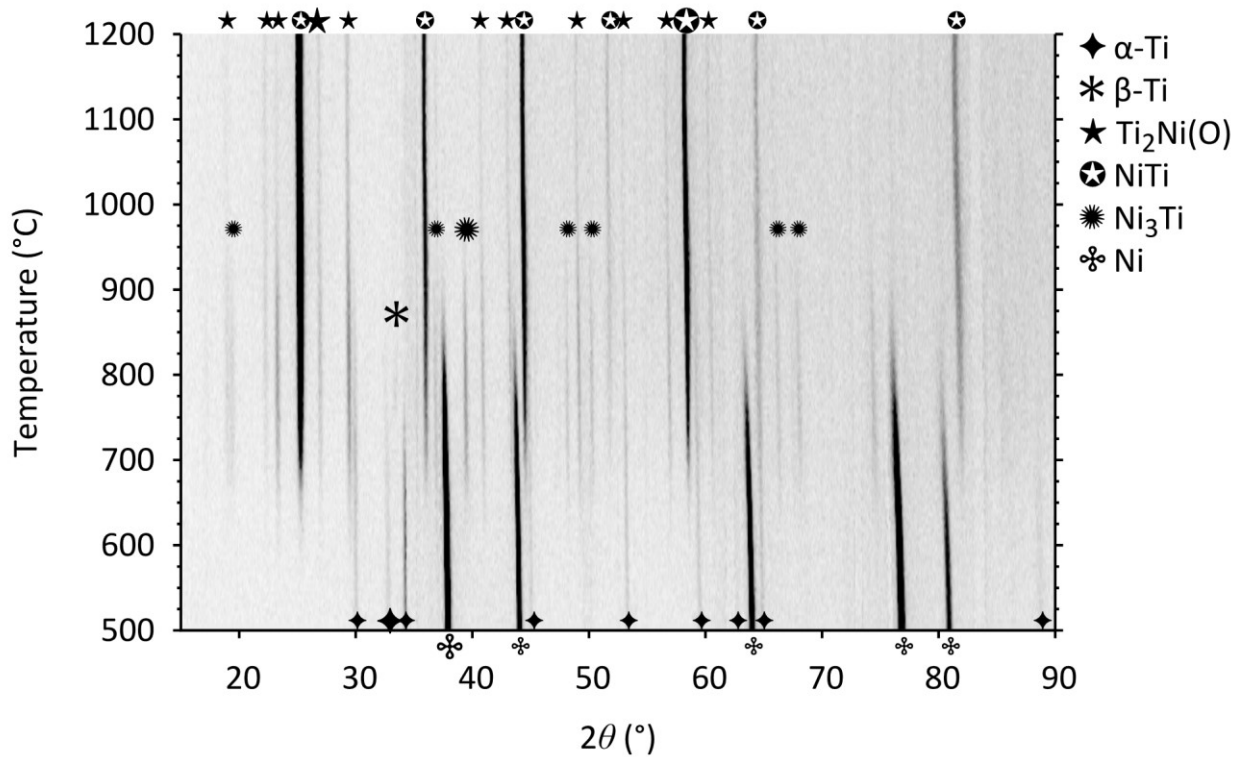
Figure 4-17   **In-situ 2-D neutron diffraction film plot of the LP Ti mixture during heating from 500 to 1200 °C at 2 °C/min (oversized symbols denote peaks selected for area analysis)**

Legend:
- ✦ α-Ti
- ✳ β-Ti
- ★ Ti₂Ni(O)
- ✪ NiTi
- ✺ Ni₃Ti
- ✿ Ni
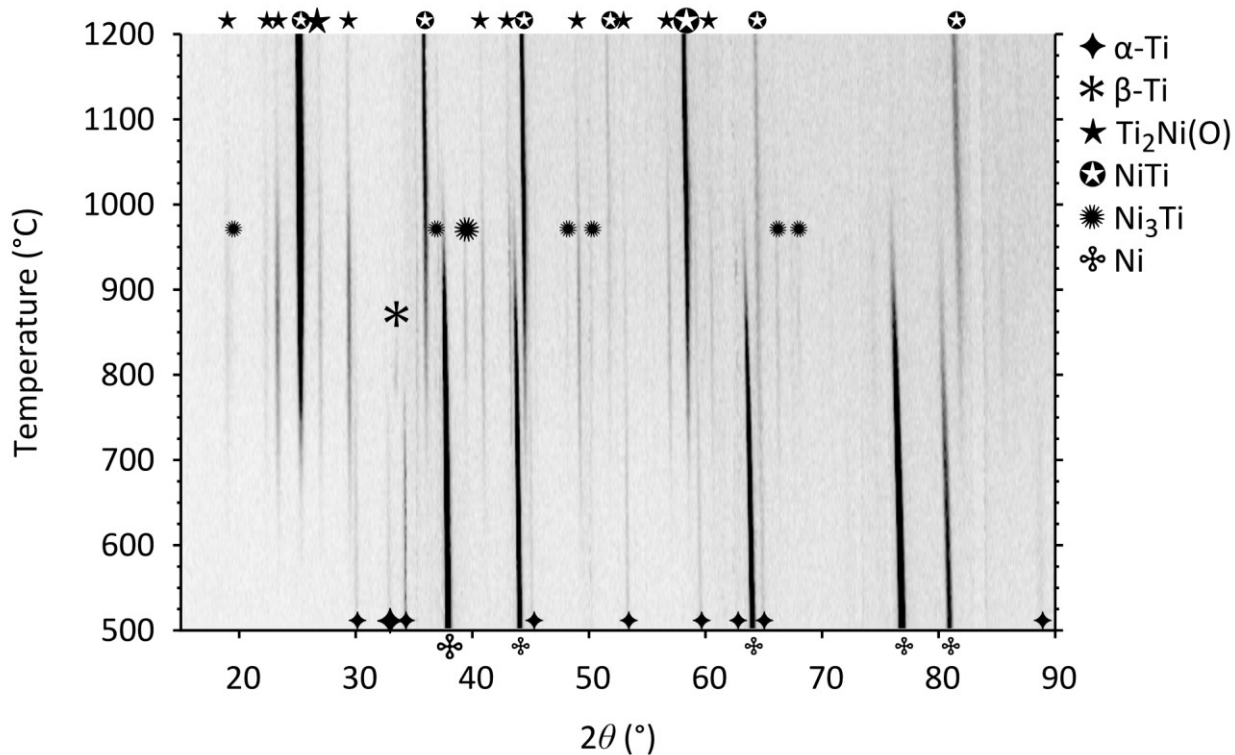
Figure 4-18   **In-situ 2-D neutron diffraction film plot of the HP Ti mixture during heating from 500 to 1200 °C at 2 °C/min (oversized symbols denotes peaks selected for area analysis).**

At 500 °C, the lowest temperature at which diffraction data were acquired, there are no detectable differences between the LP mixture (Figure 4-17) and the HP mixture (Figure 4-18), which simply consist of elemental Ni and α-Ti. In the LP mixture, significant changes in the diffraction pattern occur between 600 °C and 940 °C. The growth of the three intermetallic phases (Ni_3Ti, NiTi and Ti_2Ni) and the disappearance of the primary Ni and α-Ti phases are easily followed. The strongest signal comes from the NiTi phase, which persists up to the maximum temperature of 1200 °C. The intensities of the Ti_2Ni and the Ni_3Ti diffraction peaks initially increase, then decrease during heating. While the Ti_2Ni signal persists up to the maximum temperature, the Ni_3Ti signal disappears at approximately 1100 °C.

The phase evolution in the HP mixture is similar to that in the LP mixture. However there are some important differences. Ni_3Ti peaks appear at a lower temperature and reach higher intensities in the LP mixture. This enhanced Ni_3Ti formation correlates with an earlier disappearance of the Ni diffraction peaks (~940 °C) than in the HP mixture (~1025 °C). Finally, there is evidence of enhanced solid-state transformation of α-Ti to β-Ti in the HP mixture, indicating that this Ti rich phase has reacted to form intermetallic phases to a lesser extent than in the LP mixture.

Based on the persistence of NiTi and Ti_2Ni peaks, it is expected that these phases will appear in the microstructure after cooling to room temperature. Neutron diffraction performed on the post sintered specimens at room temperature confirms the presence of both phases. The room temperature diffraction patterns are not presented to avoid possible confusion caused by the NiTi phase transformation from austenite to martensite. Instead, the etched microstructures of the post-sintered samples in Figure 4-19 demonstrate that, indeed, the two phases remain in the samples. The similarity in the microstructures produced by heating to 1200 °C at 2 °C/min in the DSC (Figure 4-15) and ND experiments (Figure 4-19) indicates good correlation between the two sintering procedures.
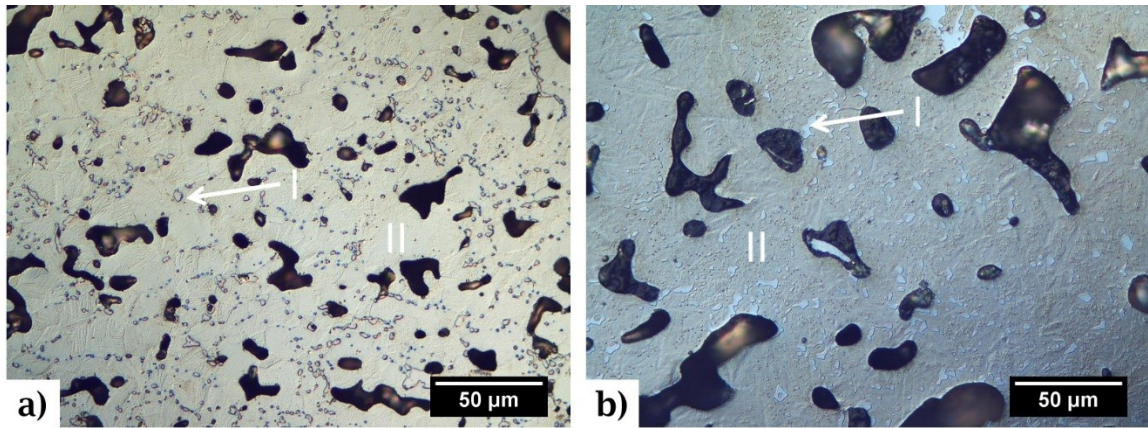
Figure 4-19 **Optical micrographs of the powder mixtures (a - LP mixture, b - HP mixture) after in situ sintering in the neutron beam. (I – Ti2Ni, II – NiTi)**

Additional insights into the phase progression suggested by the plots of Figures 11 and 12 can be obtained from the plots in Figure 4-20 through Figure 4-24. In these figures, a single diffraction peak from each phase that was reasonably well separated from neighbouring peaks was chosen for analysis (labelled using oversized symbols in Figure 4-17 and Figure 4-18). The integrated area under each peak was determined and is proportional to the mass of the corresponding phase. Given a small difference in the total mass (approximately 4%) between the LP mixture and the HP mixture specimens, it is possible to directly compare the influence of Ti purity levels on intermetallic phase progression. However, absolute quantitative values for the phase fraction were not determined. For low intensity peaks, it was found that the 2.5 minute acquisition time was insufficient to obtain peaks of sufficient intensity. Therefore, four patterns were binned into one pattern containing phase information spanning 20 °C instead of the usual 5 °C for all peaks. Since lattice parameters change with temperature due to thermal expansion, the diffraction peaks were tracked by allowing the range of angles used for the

area calculation to shift to lower scattering angles concomitantly with the diffraction peaks. The curves overlaid on the data points are guides for the eye. The uncertainty in the peak intensity values is assumed to be the square root of the integrated area, since neutron counting can be considered a Poisson process, for which the best estimate of the standard deviation is the square root of the count itself.
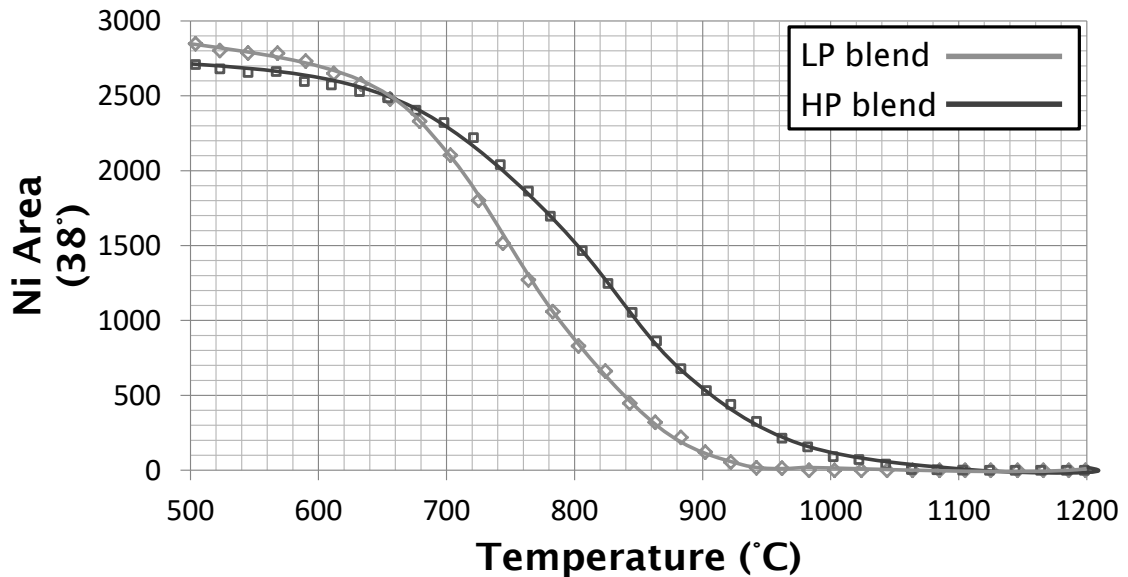
Figure 4-20   Phase evolution of elemental Ni in the two Ti mixtures during sintering from 500-1200 °C at 2 °C/min

Figure 4-20 shows the evolution of the intensity of the Ni (111) diffraction peak with temperature in the two powder mixtures. The peaks start at similar total intensities in the two powders at 500 °C. At a little above 600 °C, in both mixtures, the peak intensity starts to decrease. The peak intensity decreases at a faster rate in the LP mixture than in the HP mixture, becoming undetectable (i.e. falling to the background level of the diffraction pattern) at approximately 960 °C, while the peak in the HP mixture does not

disappear until 1060 °C. These results indicate that the consumption of the Ni phase through the formation of intermetallic phases occurs more rapidly in the LP mixture.
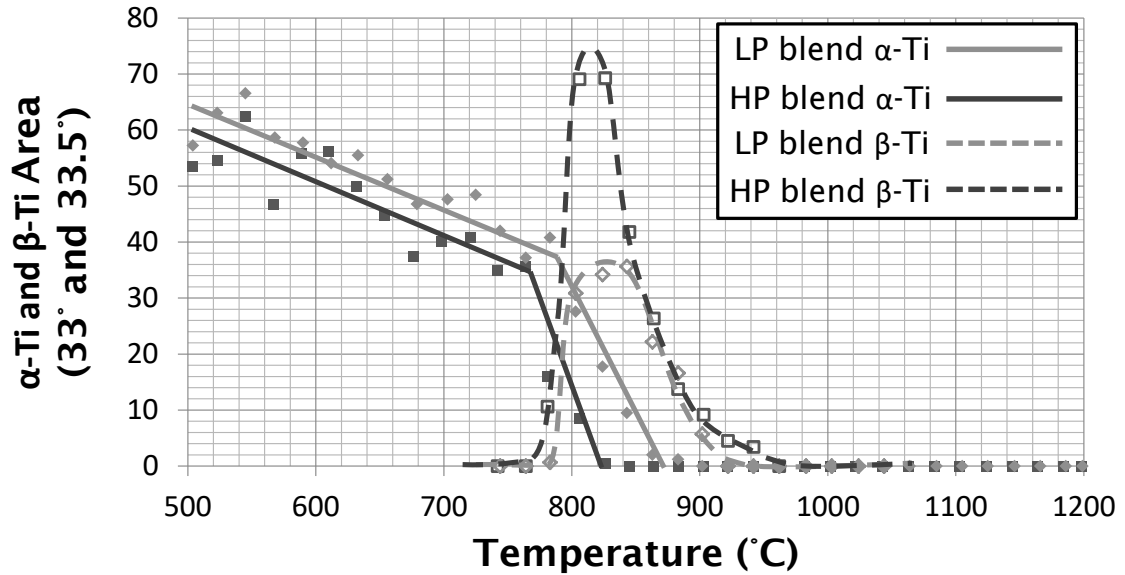
Figure 4-21   Phase evolution of elemental Ti in the two Ti mixtures during sintering from 500-1200 °C at 2 °C/min

The phase evolution of Ti (α-Ti (002) and β-Ti (110)) is shown in Figure 4-21. Similarly to the Ni peaks, the Ti diffraction peaks in both mixtures start off at approximately the same intensity. The intensity of the α-Ti peak decreases more rapidly in the LP mixture than in the HP mixture. Interestingly, the rate at which the intensities of the α-Ti(Ni) peaks decrease shows a sharp increase at 760 °C, at which the β-Ti(Ni) (110) peak first appears. This observation constitutes direct evidence that the reverse eutectoid reaction α-Ti(Ni) + Ti₂Ni → β-Ti(Ni) does indeed occur in these elemental mixtures due to solid-state interdiffusion during heating. This result provides an unambiguous explanation of the phase transformation corresponding to the DSC peaks which have an onset at 760 °C.

During further heating beyond 765 °C, the in-situ ND results indicate that there is a gradual reduction in α-Ti(Ni) and a gradual increase in β-Ti(Ni) up to 820 °C. This result reveals the gradual nature of the α to β phase transformation in the Ti(Ni) phase, which is a consequence of a compositional gradient present in the α-Ti(Ni) phase due to the formation of diffusion couples. This interpretation is supported by the DSC results, in which a very broad transformation peak is visible after the 765 °C onset temperature. If all of the α-Ti(Ni) had been consumed through the reverse eutectoid reaction, the DSC transformation peak and the ND phase evolution would have occurred over a much narrower temperature range. These results therefore constitute clear proof of a Ni compositional gradient within the α-Ti(Ni) phase.

The intensity of the β-Ti(Ni) peak reaches a maximum in both powder mixtures at around 820 °C, which is also the temperature at which the α-Ti(Ni) peak disappears. At this stage, the α to β phase transformation is complete. A reduction in the intensity of the β-Ti(Ni) peak beyond this temperature indicates that the remaining β phase is consumed through intermetallic phase formation. While the intensity of the β-Ti(Ni) peak reaches a maximum in both the LP and HP mixtures at around 820 °C, the maximum intensity is twice as high in the HP mixture as in the LP mixture. This result, which is consistent with the DSC results presented earlier, indicates that lower purity Ti powder promotes more extensive consumption of the Ti-rich phase in both its α and β forms through intermetallic phase formation. The diffraction results also show that all of the β-Ti(Ni) has disappeared by 900 °C in the LP mixture, again consistent with the DSC results, in which no eutectic melting reaction (i.e. β-Ti(Ni) + Ti$_2$Ni → L) was detected for this sample. The small eutectic melting peak at 942 °C in the DSC trace for the HP mixture is

consistent with the ND measurements, which shows that the β-Ti(Ni) phase persists up to 940 °C, then disappears abruptly at 960 °C.
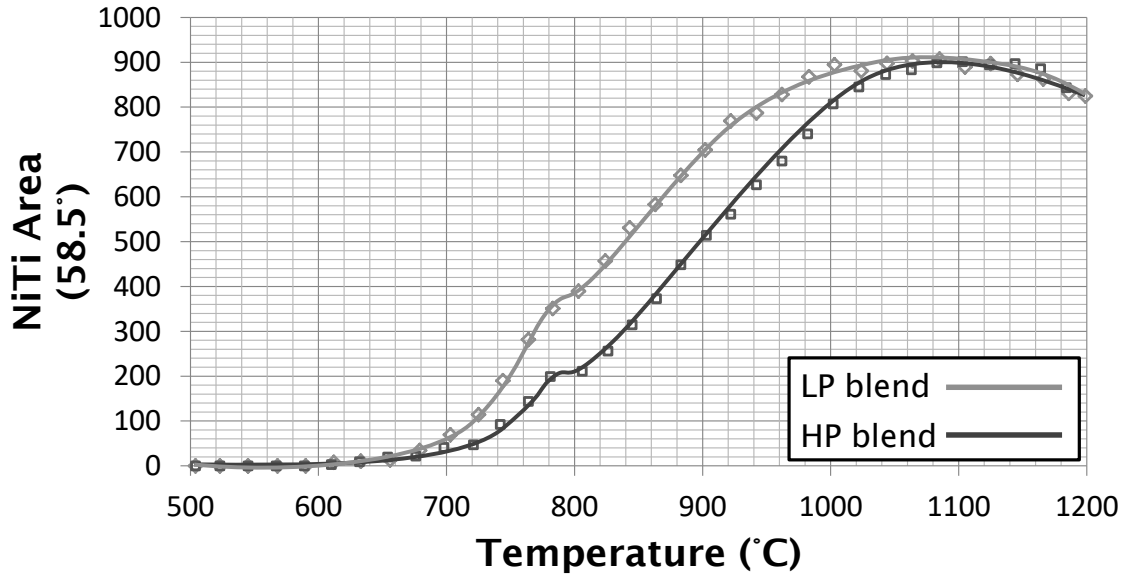
Figure 4-22   **Phase evolution of NiTi in the two Ti mixtures during sintering from 500-1200 °C at 2 °C/min**
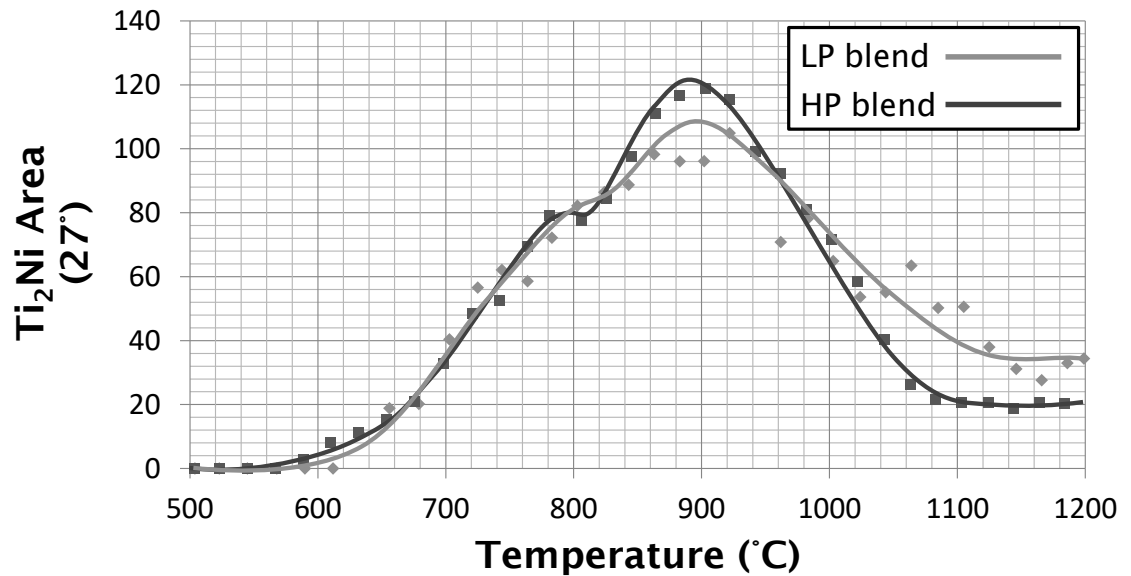
Figure 4-23   **Phase evolution of Ti2Ni in the two Ti mixtures during sintering from 500-1200 °C at 2 °C/min**
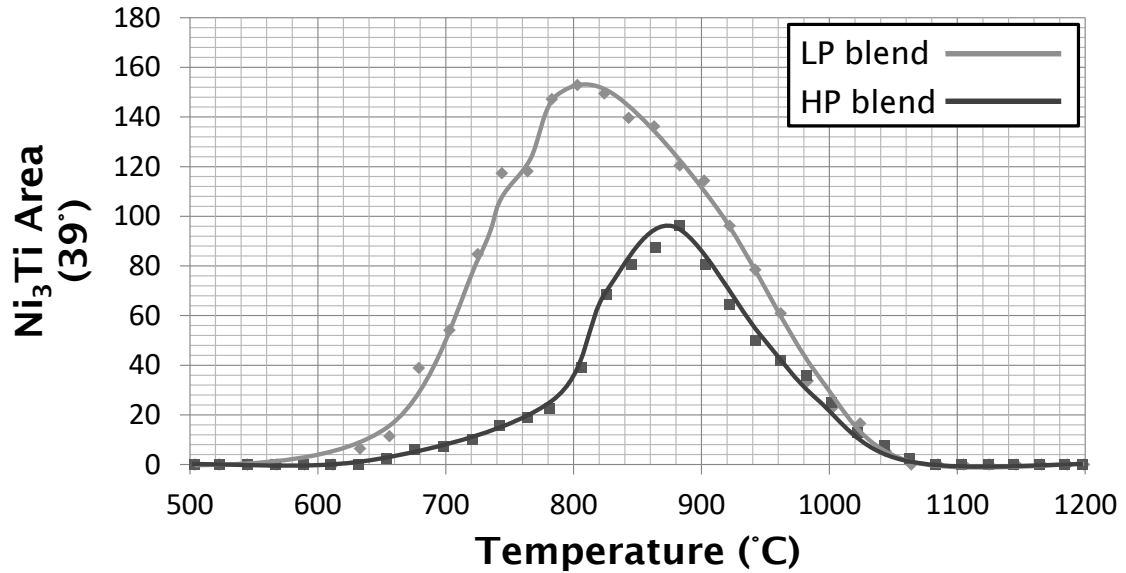
Figure 4-24 **Phase evolution of Ni3Ti in the two Ti mixtures during sintering from 500-1200 °C at 2 °C/min**

The evolution of the intermetallic phases is presented in Figure 4-22 through Figure 4-24. The intensity of the NiTi (210) peak in both the LP and the HP mixtures (Figure 4-22) starts to steadily rise slightly above 600 °C. Starting at around 700 °C, the intensity of the NiTi peak in the LP mixture increases rapidly, reaching a maximium at 1040 °C, followed by a slow decrease upon further heating. The intensity of the NiTi peak in the HP mixture starts to increase rapidly starting at around 760 °C, reaches a maximum at 1100 °C, then drops slightly during further heating. This drop in intensity at the higher temperatures is a consequence of the thermal motion of the atoms (Debye-Waller factor) – it does not indicate a reduction in amount of NiTi present, nor a B2 to BCC order to disorder transition [60].

Figure 4-23 shows how the Ti$_2$Ni (400) peak intensity evolves with increasing temperature. The growth of the Ti$_2$Ni phase is similar for both powder mixtures – the

91

peak intensity changes little from 500 to 600 °C, increases to a maximum at 900 °C, then drops back down to a non-zero level at higher temperatures. The intensity is higher in the LP mixture than in the HP mixture at 1200 °C. The equilibrium phase diagram shows that the reverse peritectic reaction, $Ti_2Ni \rightarrow NiTi + liquid$, occurs at 984 °C leading to melting of Ti_2Ni. However, the ND results for both mixtures indicate that Ti_2Ni persists up to the peak temperature of 1200 °C. This result is consistent with the DSC results which do not show any evidence of a thermal event associated with the peritectic reaction at 984 ℃.

The presence of Ti_2Ni in the ND patterns is consistent with the room temperature micrographs of the DSC specimens. The persistence of Ti_2Ni above the peritectic temperature (984 °C) and up to 1200 °C is unexpected. The presence of this phase was reported previously by authors studying the phase progression through TE-SHS [110], as well as by Chen, Liss and Cao in their in-situ ND work on Ni rich NiTi [60–62]. Figure 4-25 shows the results of spot EDS on the HP mixture after sintering on points less than 5 μm apart. It is clear that the Ti_2Ni contains more oxygen than the surrounding NiTi, indicating that this phase is in reality the $Ti_4Ni_2O_X$ phase reported in the literature. Besides the current ND work and the ND work by Chen, Liss and Cao, there has been no direct evidence that this solid phase exists above the peritectic temperature and, indeed, is present during the whole sintering process. Though the presence of Ti_2Ni (or $Ti_4Ni_2O_X$) at room temperature is well established in the literature, there has only been speculation as to its origin. Even in the paper by Chen, Liss and Cao, the presence of Ti_2Ni above the peritectic temperature is assumed to be due to a thin layer of oxide surrounding the Ti_2Ni particles.
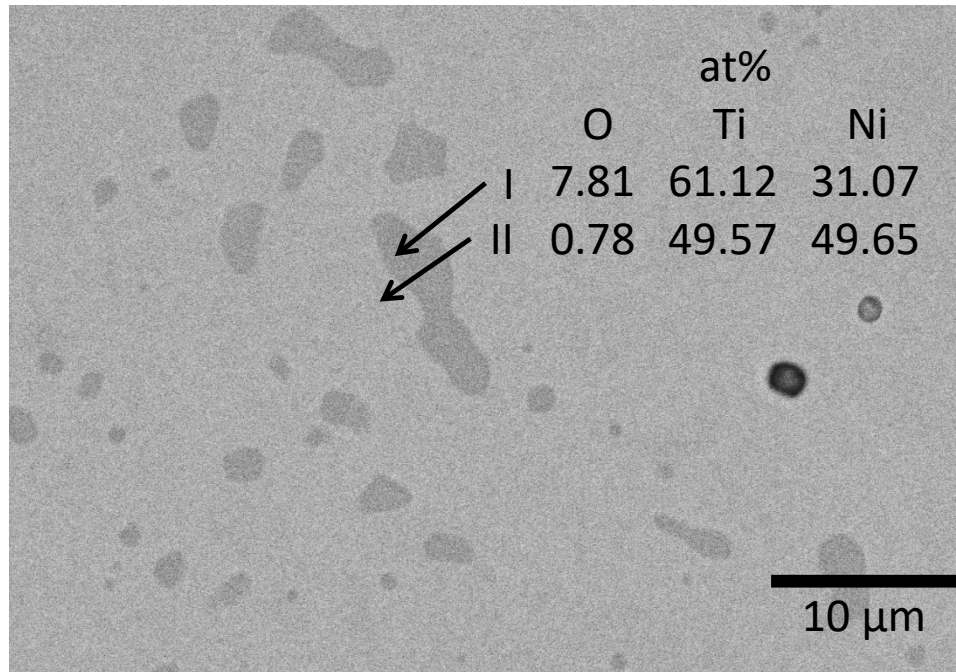
Figure 4-25   EDS results on the two phases present in the HP Ti mixture after ND in situ sintering. (I-Ti2Ni(O); II-NiTi)

Some work has been done on the Ti-Ni-O system [43,113,114] but the highest temperature at which experimental data on the Ti-rich side of the ternary phase diagram are available is 900 °C. Interestingly, the ternary phase diagram contains a solid $Ti_2Ni(O)$ phase over a wide range of compositions. In particular, for a Ni/Ti ratio of 1, a two-phase $Ti_2Ni(O)$-Ni_3Ti phase region occurs. Thus, in the presence of modest amounts of oxygen, NiTi need not form as an interlayer between $Ti_2Ni(O)$ and Ni_3Ti layers. Taking into account the current ND results and the ternary phase diagram, it is proposed that the $Ti_4Ni_2O_X$ oxide phase reported in the literature is not an oxide but rather a solid solution, $Ti_2Ni(O)$, which is stable to at least 1200 °C. More work is required to verify this suggestion. Given that little is known about the $Ti_2Ni(O)$ phase above 900 °C, its role in microstructural development during sintering of NiTi is unknown.

93

The most significant difference in the phase evolution behaviours exhibited by the LP and HP mixtures is in the formation of Ni_3Ti, as demonstrated in the evolution of the Ni_3Ti (202) diffraction peak with temperature (Figure 4-24). In the LP mixture, Ni_3Ti begins to form at ~620 °C, the diffraction peak intensity reaching a maximum at 820 °C. In contrast no (or too little to measure) Ni_3Ti is present in the HP mixture until approximately 760 °C, with the maximum amount occurring at 870 °C. The diffraction peaks for this phase disappear in both powder mixtures at ~1040 °C. The complete disappearance of the Ni_3Ti phase before 1100 °C, as shown by the ND results, is consistent with the DSC trace: no high temperature melting event was detected at 1117 °C, as would have occurred through the reaction $NiTi + Ni_3Ti \rightarrow L$, if any Ni_3Ti were present in the sample at this temperature.

4.3.3.3 Discussion

By combining DSC and ND, a more complete picture of the phase evolution during sintering of NiTi from elemental powders emerges than was previously available, summarized with the aid of the schematic model of Figure 4-26. For both powder mixtures, from 500 to 600 °C, a minor amount of Ti_2Ni forms, with no other intermetallic phase formation. The decrease in the α-Ti (002) peak intensity (Figure 4-21) is due to the formation of Ti_2Ni. However, to a first approximation, both mixtures consist only of α-Ti and pure Ni up to 600 °C (Figure 4-26a). From 600 to 700 °C the intermetallic phases (NiTi, Ti_2Ni and Ni_3Ti) begin to grow (see Figure 4-22 through Figure 4-24) and the more drastic reduction in intensity of the elemental Ti and Ni diffraction peaks is due to the consumption of these reactants to form the intermetallic reaction products. Ti_2Ni

exhibits the highest growth rate in this temperature range, followed by Ni$_3$Ti, particularly in the LP mixture (Figure 4-26b). Very little NiTi forms in either mixture over this temperature range.
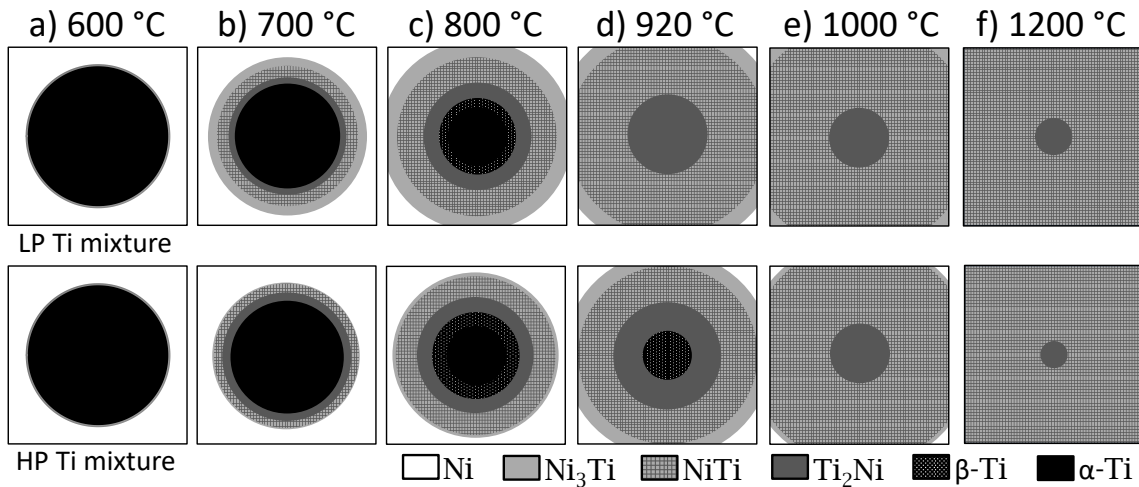
Figure 4-26   Schematic of the phase progression in the LP Ti mixture and the HP Ti mixture.

The onset of intermetallic phase formation, found to occur at around 600 °C via ND, is similar to that determined using DSC based on the exothermic shift in the heat flow trace for both heating rates used (2 °C/min and 20 °C/min). Yamamoto *et al.* [115] showed that Ti can dissolve significant quantities of O during heating only at temperatures above 600 °C. Malinov, Sha and Voon [116] studied surface oxidation of Ti6Al4V. During heating, the surface of the Ti6Al4V was found to oxidize, yet upon further heating the oxide disappeared. They proposed that this phenomena was due to increased O solubility in Ti and dissolution of the lower oxides present on the surface of the Ti6Al4V. It was also suggested that for the binary Ti-O system, dissolution of the surface oxides should occur around 600 °C. Based on this previous work, the onset of intermetallic phase formation

observed in the current work is thought to be due to the diffusion of oxygen into Ti, and the subsequent dissolution of oxide from the surface of the Ti powder starting at 600 °C. Removal of the surface oxide allows direct contact between the Ni and Ti reactants.

In both mixtures, there is a relatively slow rate of decay in the fraction of reactants (i.e. Ni and α-Ti(Ni)) up to 700 °C. The higher rate of Ni decay in the LP mixture is the result of more rapid growth of NiTi and Ni_3Ti compared with the HP mixture: ND indicates that almost no Ni_3Ti is present in the HP mixture at 700 °C. In the HP Ti it is assumed that the Ni_3Ti layer surrounding the Ni particles is so thin that it amounts to a very small volume fraction which is below the ND detection threshold. For Ti_2Ni to grow into α-Ti(Ni), Ni is required at the Ti_2Ni - α-Ti(Ni) interface. Likewise, for Ni_3Ti to grow into Ni, Ti is required at the Ni_3Ti – Ni interface. Given that the growth of Ti_2Ni is similar in both powder mixtures, Ni atoms move from Ni to the Ti_2Ni - α-Ti(Ni) interface at similar rates in both powder mixtures. Also, the slower growth of Ni_3Ti in the HP mixture than in the LP mixture indicates that Ti atoms diffuse from α-Ti(Ni) to the Ni_3Ti – Ni interface more slowly in the HP mixture than in the LP mixture. This discrepancy in diffusion rates is thought to be due to the different Ti powder purities. While it is beyond the scope of the present investigation to determine which impurities are responsible for this behaviour, work by Herzig, Mishin and Divinski [11] and by Perez, Nakajima and Dyment [117] shows a significant increase in the rate of self-diffusion in titanium (up to two orders of magnitude at 600 °C) with very small additions of Ni and Fe in α-Ti.

The most rapid phase evolution in both mixtures takes place between 700 and 920 °C (Figure 4-26c and d). Starting at 765 °C, α-Ti(Ni) is rapidly consumed by the growing β-

Ti(Ni) phase (Figure 4-21) such that, by 800 °C, both α-Ti(Ni) and β-Ti(Ni) are present in the microstructure (Figure 4-26c). The growth rate of all three intermetallic phases also increases in this temperature range, correlating with a rapid drop in the fraction of elemental Ni. The LP mixture comprises less Ni with more NiTi and Ni_3Ti than the HP mixture at 800 °C (Figure 4-26c). Both mixtures show the highest fraction of β-Ti(Ni) just above 800 °C, due to the complete transformation of α to β. This temperature also corresponds to the maximum phase fraction of Ni_3Ti in the LP mixture and a noted increase in the rate of Ni_3Ti formation in the HP mixture. In the LP mixture, the maximum fraction of Ni_3Ti is reached while there is still ~33% of the initial Ni left. Past investigations have found that once an initial layer of Ni_3Ti has formed, slow diffusion of Ti atoms through the layer impedes further growth [8,9]. In the HP mixture, the presence of β-Ti(Ni) appears to alter the rate of diffusion through the diffusion couple, thereby providing a boost to the growth of Ni_3Ti.

The growth rate of the β-Ti(Ni) phase is influenced by the changing Ni solubility due to increasing temperature and by the diffusion of Ni. As the temperature increases, β-Ti(Ni) becomes stable over a larger range of Ni concentrations, allowing β-Ti(Ni) to grow into both α-Ti(Ni) and Ti_2Ni. At the same time, Ni is diffusing into α-Ti(Ni) and transforming it into β-Ti(Ni) (evidenced by the disappearance of α-Ti(Ni) in both mixtures prior to the α-Ti to β-Ti transition of pure Ti). The fraction of β-Ti(Ni) reaches a maximum in both Ti mixtures (~820 °C) at approximately the same temperature that α-Ti(Ni) disappears. Having consumed the α-Ti(Ni) phase, β-Ti(Ni) begins disappearing due to the continuing growth of intermetallic phases which typically reach their maximum growth rates in the temperature range 800 to 900 °C.

At approximately 920 °C (Figure 4-26d), most of the Ti and Ni reactant phases have been consumed in both mixtures. At this point, the Ti_2Ni reaches a maximum in both mixtures and Ni_3Ti reaches a maximum in the HP mixture (Ni_3Ti is already in decline in the LP mixture). Overall, the phase progression is further advanced in the LP mixture, with no Ti rich reactant phase remaining at 920 °C.

Further heating to 1000 °C causes continued growth of the NiTi phase. In this same temperature range, there is a relatively rapid drop in the fractions of Ti_2Ni and Ni_3Ti, indicating that the growth of Ti_2Ni and Ni_3Ti relies on the consumption of the adjacent reactant β –Ti(Ni) and Ni phases. Once all reactants have been consumed, homogenization toward the favoured intermetallic phase occurs, resulting in increased NiTi formation at the expense of the other intermetallic phases (Figure 4-26e). Above 1050 °C, the microstructure becomes a stable mixture consisting predominantly of NiTi and a small fraction of Ti_2Ni (Figure 4-26f).

4.3.4   *Summary*

It can be concluded that the purity level of the titanium starting powders plays an important role from the beginning stages of sintering right through to the final product. The higher levels of impurities in the LP Ti lead to a faster rate of reaction in the LP mixture compared to the HP mixture, particularly with respect to the formation of Ni_3Ti in the early stages of sintering. As a consequence, a much smaller TE-SHS reaction (for heating at 20 °C/min) occurs in the LP mixture, leading to a much finer scale porosity but very irregularly shaped pores in comparison to the rounded pores in the HP mixture (due to a higher liquid fraction in the HP mixture). The initial oxygen content of the powders

plays a role in stabilizing the Ti$_2$Ni phase at higher temperatures, making homogenization difficult. It is suggested that this phase is a solid solution rather than the oxide phase proposed in the literature.

4.4 PAPER 2: RIETVELD REFINEMENT ON IN-SITU NEUTRON DIFFRACTION OF SINTERING OF NITI FROM ELEMENTAL POWDERS

Authors: Dan Cluff, Stephen F. Corbin and Michael A. Gharghouri

Status of the paper: the paper is currently in the internal Chalk River Labs peer review process.

My contribution: I designed the experimental plan in collaboration with Dr. Stephen Corbin and Dr. Michael Gharghouri (neutron work only). All the specimen preparation and experimental work was performed by me with the exception of the powder size analysis and chemical composition (reported in 4.1), as well as the neutron diffraction where I assisted Dr. Michael Gharghouri at Chalk River Laboratories. I performed all of the data analysis and wrote the first draft of the manuscript. The current state of the manuscript is a result of editing and proof reading by all three authors.

Notes on editing for the thesis: To improve the flow of the thesis elements that repeat what is discussed elsewhere have been removed. This includes the Introduction and the Acknowledgements. Portions of the Materials and Methods have been edited out, keeping only the information regarding powders used, naming conventions and sintering profiles discussed in the manuscript.

4.4.1 *Abstract*

Rietveld refinement of neutron diffraction patterns obtained *in-situ* during the reactive sintering of Ni-Ti (49 at% Ni : 51 at% Ti) elemental powder compacts for two sintering profiles was performed. The atomic displacement parameter (U_{iso}) and the lattice parameters for each phase that occurs during reactive sintering (α-Ti , β-Ti(Ni), $Ti_2Ni(O)$, NiTi, Ni_3Ti and Ni) were obtained from separate *in-situ* experiments on stoichiometric powder mixtures. A detailed description of the procedure for the Rietveld refinements is presented. The determination of accurate U_{iso} values and lattice parameters from separate experiments was found to be critical to the successful refinement of minority phases. The phase fractions determined from the two sintering runs were found to be in excellent agreement, with an uncertainty estimated at +/- 0.016 wt%. Intermetallic phases do not begin to form until the oxide layer surrounding the Ti particles dissolves at 600 °C. Initially, $Ti_2Ni(O)$ grows faster than NiTi and Ni_3Ti. By 780 °C, NiTi becomes the dominant phase, growing at the expense of all the other phases. Homogenization occurs at 1100 °C, at which the microstructure consists of 93 wt% NiTi and 7 wt% $Ti_2Ni(O)$. Refinement of the O concentration in $Ti_2Ni(O)$ during sintering yields a better understanding of why $Ti_2Ni(O)$ is always found after sintering from elemental powders. During the initial stages of sintering, $Ti_2Ni(O)$ with little or no O is formed. As the amount of this phase increases, its O content also increases, likely as a result of accepting O from the elemental Ti that it consumes as it grows. The O concentration in $Ti_2Ni(O)$ increases as its phase fraction decreases since it retains all of its O even as it is consumed by NiTi in the later stages of sintering. The oxygen raises the melting point of the phase

such that it is in equilibrium with NiTi at 1200 °C, despite Ti_2Ni having a melting temperature of 984 °C.

4.4.2   *Experimental method (edited)*

4.4.2.1 Materials

The Ni powder used in all the experiments was the F Ni powder. The Ti powder was either an LP Ti powder or an HP Ti powder. Both powders were obtained from Alfa Aesar. Four different mixtures were prepared from the elemental powders. The primary mixture was 49 at% Ni - 51 at% Ti (i.e. Ti-rich NiTi) prepared using the 99.5 wt% Ti powder (*LP mixture*). This mixture was the primary focus of this investigation. The other three mixtures, all prepared using the 99.99 wt% Ti powder, were 33 at% Ni - 66 at% Ti (i.e. Ti_2Ni mixture), 75 at% Ni - 25 at% Ti (i.e. Ni_3Ti mixture) and 5 at% Ni - 95 at% Ti (i.e. 95Ti/5Ni mixture), were required for the analysis of the primary mixture.

4.4.2.2 In-situ neutron diffraction

Two in-situ ND runs were performed on the *LP mixture*: the *RS1000* and the *RS1200* sintering profiles. To aid in the analysis of the reactive sintering study by obtaining a baseline for each of the component phases, the following four ND runs were (see Table 3-3 for sintering profiles):

1) An empty Mo crucible (*Mo1200*).
2) Two elemental Ti pellets and two elemental Ni pellets together in the same V crucible (*El Ni/El Ti*).
3) 95Ti/5Ni mixture (*95Ti/5Ni*).

4) Two pellets of Ti$_2$Ni and two pellets of Ni$_3$Ti (*Ti$_2$Ni/Ni$_3$Ti*).

4.4.3 *Application of Rietveld Analysis to the NiTi system*

Analysis of the diffraction patterns obtained during *in-situ* reactive sintering of Ti and Ni

elemental powder compacts is challenging. While the compacts initially consist of a

simple two-phase powder mixture, up to seven phases can be present simultaneously

during heating, until the system evolves (ideally) into a near-equiatomic NiTi single

phase. The crystal structures of Mo and of the seven possible Ni-Ti phases are given in

Table 4-4 [102,103,118–120]. Nascent phases and phases which represented a small

fraction of the microstructure nevertheless contributed weak diffraction peaks to the

pattern, increasing the difficulty of obtaining reliable results. To successfully model the

diffraction data from the two mixtures, it was necessary to reduce the number of

adjustable parameters. This reduction was achieved by obtaining suitable expressions for

the evolution of U_{iso} with temperature for each phase from the *in-situ* neutron data for the

baseline samples and the Mo crucible. These expressions were used to calculate

temperature-dependent U_{iso} values, which were in turn used as-is (i.e. without allowing

them to refine) for the subsequent analyses of the patterns for samples *RS1000* and

RS1200. While values for the atomic displacement parameters for pure elements are well

known [121], they are not readily available for the Ni-Ti phases of interest in the current

work ((Ni) and (Ti) solid solutions, and the intermetallic Ti$_2$Ni, NiTi and Ni$_3$Ti phases).

Baseline runs *Mo1200*, *El Ni/El Ti*, *95Ti/5Ni* and *Ti$_2$Ni/Ni$_3$Ti* were therefore critical in

developing a clear understanding of how the diffraction pattern of each constituent phase

changed during heating in the absence of other phases. In addition to U_{iso} values, the baseline runs also yielded lattice parameters for each phase.

Table 4-4   **Crystallographic information used during Rietveld refinement. Taken from the following references: [a]- [118], [b]- [119], [c]- [102,103], [d]- [120]**

Phase	Space Group	Lattice Parameters		Atoms						Ref.
		a (Å)	c (Å)	element	Wykoff site	x	y	z	occupancy	
α-Ti	P63/mmc (194)	2.9508	4.6855	Ti	2c	1/3	2/3	1/4	1	[a]
β-Ti	Im-3m (229)	3.279		Ti	2a	0	0	0	1	[a]
Ti_2Ni*	Fd-3m (227)	11.278		Ti	16C	1/8	1/8	1/8	1	[b]
				Ni	32e	0.912	0.912	0.912	1	
				Ti	48f	0.311	0	0	1	
Ti_4Ni_2O*	Fd-3m (227)	11.351		Ti	16c	1/8	1/8	1/8	1	[c]
				O	16d	5/8	5/8	5/8	1	
				Ni	32e	0.916	0.916	0.916	1	
				Ti	48f	0.312	0	0	1	
$Ti_2Ni(O)$**	Fd-3m (227)	11.278		Ti	16c	1/8	1/8	1/8	1	
		to		O	16d	5/8	5/8	5/8	0 to 1	
		11.351		Ni	32e	0.916	0.916	0.916	1	
				Ti	48f	0.312	0	0	1	
NiTi	Pm-3m (221)	3.011		Ni	1a	0	0	0	1	[b]
				Ti	1b	1/2	1/2	1/2	1	
Ni_3Ti***	P63/mmc (194)	5.0924	8.2975	Ti	2a	0	0	0	1	[d]
				Ti	2d	1/3	2/3	3/4	1	
				Ni	6g	1/2	0	0	1	
				Ni	6h	1/6	1/3	1/4	1	
Ni	Fm3m (225)	3.524		Ni	4a	0	0	0	1	[a]
Mo	Im-3m (229)	3.147		Mo	2a	0	0	0	1	[a]

* Note: atom locations in the table are those given in the references. They are for origin choice 1. These
     must be translated by (-1/8, -1/8, -1/8) to origin choice 2 before being used in GSAS.
** $Ti_2Ni(O)$ is taken as a mix between Ti_2Ni and Ti_4Ni_2O
*** PDF# 00-051-1169

U_{iso} values were constrained to be the same for all atoms in a given phase. This approach was adopted because the diffraction patterns contained low angle data (i.e. $2\theta < 95°$ or $d > 0.9$ Å) and the peak-to-background ratios were relatively low [87,93]. When large differences in atomic mass were present, specifically O compared to Ti or Ni, the error

associated with constraining all atoms to the same U_{iso} value was investigated by repeating multiple Rietveld analyses with a U_{iso} value for O double the U_{iso} value used for the Ti and Ni atoms. The changes in the results fell well within the error values presented in the results and discussions. The range in scattering angle covered by the detector was kept the same for all runs to simplify comparisons between runs. The low signal-to-noise ratio in the diffraction patterns is a consequence of having to ensure an acceptable temperature resolution. The long acquisition time required for a good diffraction pattern must be balanced against an acceptable temperature resolution. It was found that an acceptable diffraction pattern was obtained by binning 4 consecutive patterns into a single composite pattern. This results in patterns being acquired in 10-minute intervals, corresponding to a 20 °C range in temperature.

Rietveld analysis was performed using GSAS [89] with the EXPGUI [122] graphical user interface. An instrument parameter file was created by refining the diffraction pattern, recorded prior to mounting the furnace on the diffractometer, from a corundum standard. All diffraction peaks were modeled using a Pseudo-Voigt profile with Finger, Cox and Jephcoat asymmetry ('Profile type 3' in GSAS) and a peak cut offset of 0.001. The background was modeled as a Shifted Chebyshev polynomial ('Function 1' in GSAS). The instrument parameter file was used as the starting point for all subsequent Rietveld refinements. Ranges of the weighted profile R factor (R_{wp}) are provided as a measure of the discrepancies between model and experimental data (for a more detailed explanation of R_{wp} see [91]). GSAS calculates both fitted and background-subtracted R_{wp} values (R_{wp} of the whole pattern vs. R_{wp} due to the peaks only). Unless otherwise noted, the R_{wp} values quoted are the fitted R_{wp}.

The steps followed in the refinement of the room-temperature diffraction patterns for *Mo1200, El Ni/El Ti, 95Ti/5Ni* and *Ti$_2$Ni/Ni$_3$Ti*, for which long acquisition times were possible, were as follows

1) Refine the scaling and structural parameters of each phase as well as the detector zero-offset.
2) Refine peak shape parameters.
3) Refine U_{iso} values.
4) Refine the background. For this final step, the U_{iso} values were fixed, to avoid problems stemming from the typically strong correlation between the U_{iso} values and the background.

Subsequent composite patterns were batch processed. During batch processing, the parameters listed in steps 1-3 were allowed to refine at the same time with each composite pattern using the optimized parameters from the previous composite pattern as a starting point, while the background was held constant. Each fit was then revisited to check for completion and that the background matched. If either were not acceptable more work was spent on the refinement. This process was repeated until all the patterns were fit.

Mo1200 was performed to understand the contribution of the crucible to the final diffraction pattern. Atomic displacement parameter values for Mo exist [121]; however, the Mo crucibles were machined from wrought bar stock, which resulted in deviations from the expected diffraction pattern. The (110) peak at 34.9° 2θ was a double peak (see Figure 4-27) for unexplained reasons; inclusion of this section of the diffraction pattern in the refinement resulted in poor fitting results so it was excluded from the refinement. The weak preferred orientation was refined using a March-Dollase preferred orientation

correction. Due to these difficulties, the quality of the refinement suffered and the best R_{wp} was on the order of 16%. Refinement of *Mo1200* also allowed contributions of the thermocouple and the yttria coating to be evaluated. Contributions from the thermocouple were found to be small but detectable. These contributions changed with temperature as the thermocouple sheath (Ni-Cr Super Omegaclad® XL), undergoes a phase change. The peaks associated with the thermocouple were not refined, but allowed otherwise unidentifiable peaks in other runs to be accounted for. The thin yttria coating did not contribute detectable peaks, such that this phase could be ignored in all other refinements.

El Ni/El Ti (Ti and Ni) was performed in a V crucible. Since V has a near zero coherent neutron scattering cross section [123], there was no overlap with the main α-Ti peak ((101) at 34.5° 2θ) and it was not necessary to exclude any section of the diffraction pattern for the refinement. The weak preferred orientation in the Ti powder was modelled using the March-Dollase preferred orientation correction. The refinements for this run were generally good with R_{wp} ranging from 5.5% to 9.5%. The Ni U_{iso} values obtained agree well with published values while the Ti U_{iso} values obtained were higher than the published values [121] by a factor of 2.
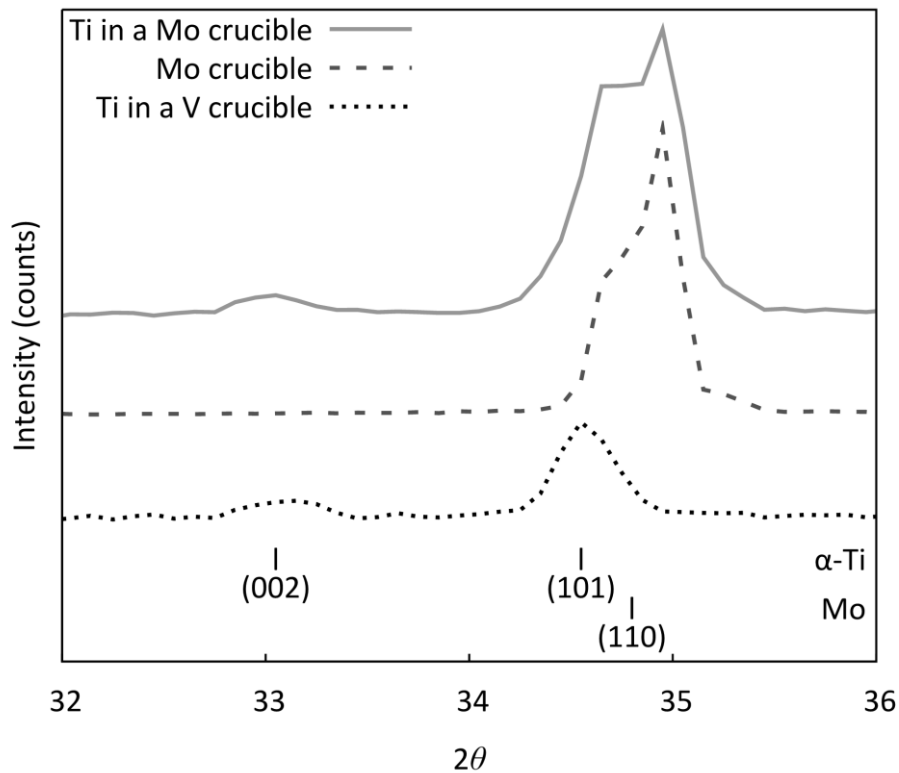
Figure 4-27   Overlap between the Mo (110) peak and the α-Ti (101) peak.

The diffraction patterns for *95Ti/5Ni* were used to characterize the effects of dissolved Ni on the structural and atomic parameters of α-Ti(Ni) and β-Ti(Ni). β-Ti(Ni) lattice parameter values were determined from diffraction patterns recorded during the ramp and hold cycles while the U_{iso} values were determined solely from the diffraction patterns recorded during the holds. Holds occurred at 756 and 805 °C on heat up, and at 805, 785, 766, 756 and736 °C during cool down, with a 160 min hold at the peak temperature (1000 °C). The refinements were generally very good, with R_{wp} ranging from 3.8% to 9.2%. The linear expression obtained for the α-Ti(Ni) U_{iso} data was in very good agreement with published data for α-Ti [121]. This result is likely due to the fact that α-Ti accepts less than 1 at% Ni in solid solution [124]. The larger volume fraction of α-Ti

(> 80 wt%) in the *95Ti/5Ni* run is thought to be responsible for the more accurate U_{iso} values compared to the *El Ni/El Ti* run. Published data for β-Ti(Ni) could not be found.

Ti$_2$Ni/Ni$_3$Ti provided values for the lattice parameters and atomic displacement parameters for these two intermetallic phases which are not available in the literature. The atomic coordinates for Ni$_3$Ti given by Pasturel [125] and PDF#04-007-1577 from the ICDD PDF-4+ database [120] produced a poor fit to the diffraction pattern due to a mismatch in relative intensities between the model and the experimental data. Changing the location of the Ti atoms from the 2c (1/3, 2/3, **0.25**) site to the 2d site (1/3, 2/3, **0.75**), per PDF #00-051-1169 from the ICDD PDF-4+ database [120], produced a very good fit with no need for corrections, despite the relative intensities in PDF#00-051-1169 matching those in PDF#04-007-1577. This discrepancy is due to the much larger contrast (difference in atomic scattering factors) between Ti and Ni for neutrons than for x-rays and shows the great advantage of using neutrons to study the NiTi system. The resulting R_{wp} values from fitting whole composite patterns (including both Ti$_2$Ni and Ni$_3$Ti) ranged from 7.3% to 8.5%.

A separate run to determine the structural and atomic displacement parameters for austenitic NiTi was not performed. Microstructural investigations on specimens sintered according to the sintering profile used in *RS1200* results in a high concentration of NiTi (~90 vol%, with Ti$_4$Ni$_2$O as the remainder) [126]. Hence the diffraction patterns recorded during cool down from *RS1200* were used to determine lattice parameters and U_{iso} values for both NiTi and Ti$_4$Ni$_2$O. While the NiTi U_{iso} values were easily optimized, U_{iso} values for the Ti$_4$Ni$_2$O phase were difficult to refine, due to the low proportion of this phase in

the mixture. The fitted R_{wp} values ranged from 6.9% to 12%. The higher R_{wp} values are a result of an initial high cooling rate. Maintaining a temperature resolution of 20 °C required that patterns be analyzed individually rather than binned in groups of 4 down to 700 °C, resulting in higher signal-to-noise ratios and worse fits to the background. For example, the pattern at 1152 °C had a fitted R_{wp} of 11.6%, but a background-subtracted R_{wp} of 8.9%. This result indicates that 20% of the R_{wp} value is due to the difficulty in modelling the noise in the background.

4.4.3.1 Examining Ti4Ni2Ox phase evolution

The difficulty of obtaining NiTi free of Ti_4Ni_2O has been noted in many studies [24,30,42,48]. It has been suggested that $Ti_4Ni_2O_X$ consists of Ti_2Ni with oxygen in solid solution [30]. More recently, $Ti_2Ni(O)$ was proposed as a better term to describe the Ti_2Ni phase with oxygen in solid solution that occurs during reactive sintering [126]. This argument is supported by the fact that Ti_2Ni and Ti_4Ni_2O have the same crystal structure. Also, Rostoker [43] noted that O can occupy vacant interstitial sites in Ti_2Ni up to the saturation point using x-ray diffraction and metallographic analysis. He showed an experimentally determined ternary phase diagram containing a single-phase field in which the Ti:Ni ratio varied little as the oxygen content varied from 0 to approximately 12 at% at 900 °C. The 4:2:1 ratio in Ti_4Ni_2O corresponds to a $Ti_2Ni(O)$ solid solution in which the interstitial sites are fully occupied. Differentiating between the two extremes of the solid solution (i.e. zero occupancy vs full occupancy of the interstitial sites) using x-rays is difficult due to the low scattering amplitude of O compared to Ni and Ti. However, neutron diffraction overcomes this problem as the scattering amplitude of O is

between those of Ti and Ni. Using VESTA [100] and RIETAN-FP [101], neutron diffraction patterns for $Ti_2Ni(O)$ with O occupancies (occ) of 0, 0.5 and 1 were generated, based on the crystal structure given in Table 4-4. The calculated patterns are shown in Figure 4-28. The Ti_2Ni crystal structure used in the calculations was identical to that of Ti_4Ni_2O, except for the lattice parameter and the occupancy of the oxygen interstitial site (Wyckoff site 16d). For the neutron diffraction pattern corresponding to 50% O occupancy of the interstitial sites, the lattice parameter was taken as the average of published values for T_2Ni and Ti_4Ni_2O. Figure 4-28 shows that, as O occupancy increases, the (222) peak at 23.5° drops significantly in relative intensity while the (311) and (400) peaks (at 22.5° and 27.2°, respectively) increase in relative intensity.
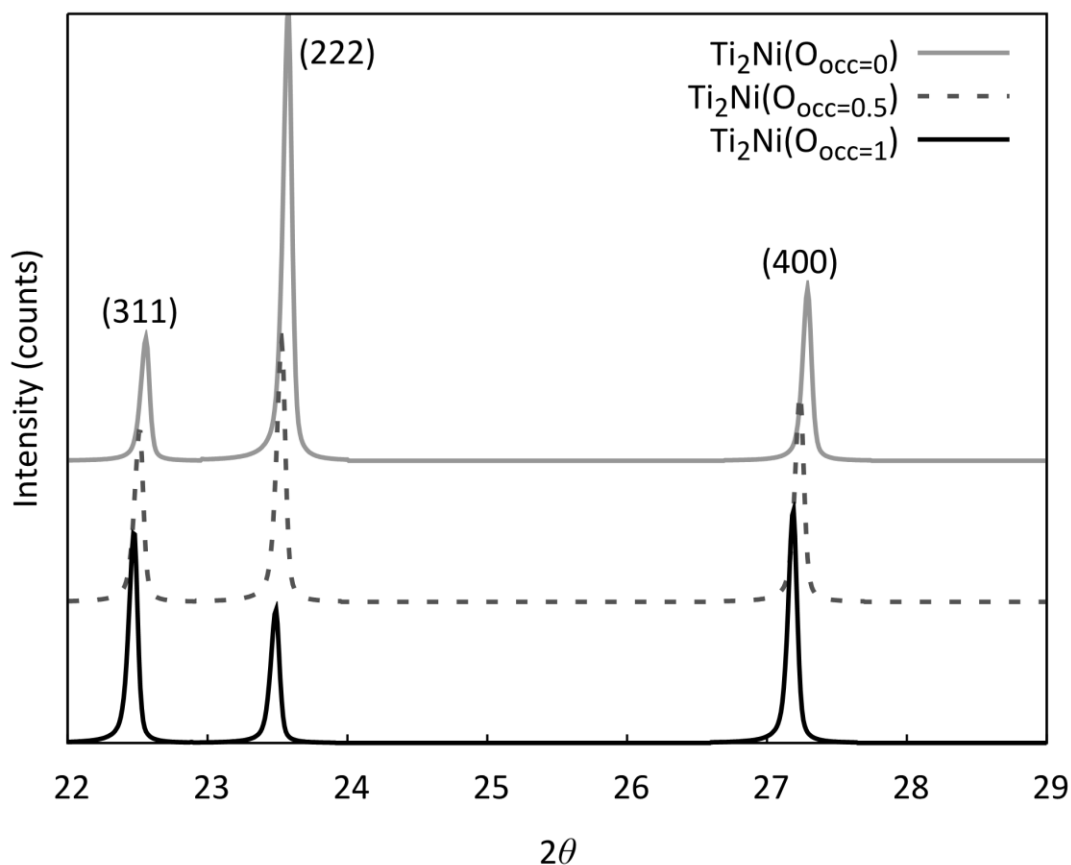
Figure 4-28   Effect of interstitial O occupancy (occ) on the calculated diffraction pattern of Ti₂Ni(O).

4.4.3.2 Examining multiphase reactive sintering in the NiTi system

A different procedure was followed to refine the diffraction patterns from *RS1000* and *RS1200* than was used for the diffraction patterns from the runs on the baseline samples. In *Mo1200*, *El Ni/El Ti*, *95Ti/5Ni* and *Ti₂Ni/Ni₃Ti,* the phase fractions of the various phases changed little if at all, and the goal was to determine the lattice parameters and U_{iso} values of each of the component phases. In *RS1000* and *RS1200*, however, the U_{iso} values were fixed in an attempt to more accurately determine the phase fractions. All phases that were expected to appear during sintering (α-Ti, β-Ti(Ni), austenitic NiTi,

Ti$_2$Ni(O), Ni$_3$Ti, Ni and Mo) were included in the analysis. The Ti$_2$Ni(O) structure used

was that of Ti$_4$Ni$_2$O with the O occupancy initially set to 0. Due to the above-mentioned

difficulties with the Mo patterns, U_{iso} values available in the literature [121] were used

for this phase. For Ni, the U_{iso} values determined from *El Ni/El Ti* were used. The α-Ti

and β-Ti(Ni) U_{iso} values were obtained from *95Ti/5Ni*. *Ti$_2$Ni/Ni$_3$Ti* provided the U_{iso}

values for Ni$_3$Ti, while the U_{iso} values for Ti$_2$Ni(O) were determined jointly from

Ti$_2$Ni/Ni$_3$Ti and from cool down patterns for *RS1200*. Although the U_{iso} values determined

for Ti$_2$Ni(O) at full and zero occupancy (Ti$_4$Ni$_2$O vs Ti$_2$Ni) were similar (within 17 %),

the U_{iso} value was calculated using a rule of mixtures depending on the O occupancy.

Finally U_{iso} values for NiTi were obtained from the *RS1200* cool down patterns. The

linear relationships between U_{iso} and temperature for all of the phases are shown in

Figure 4-29. The standard error is also shown at a single point for each line.
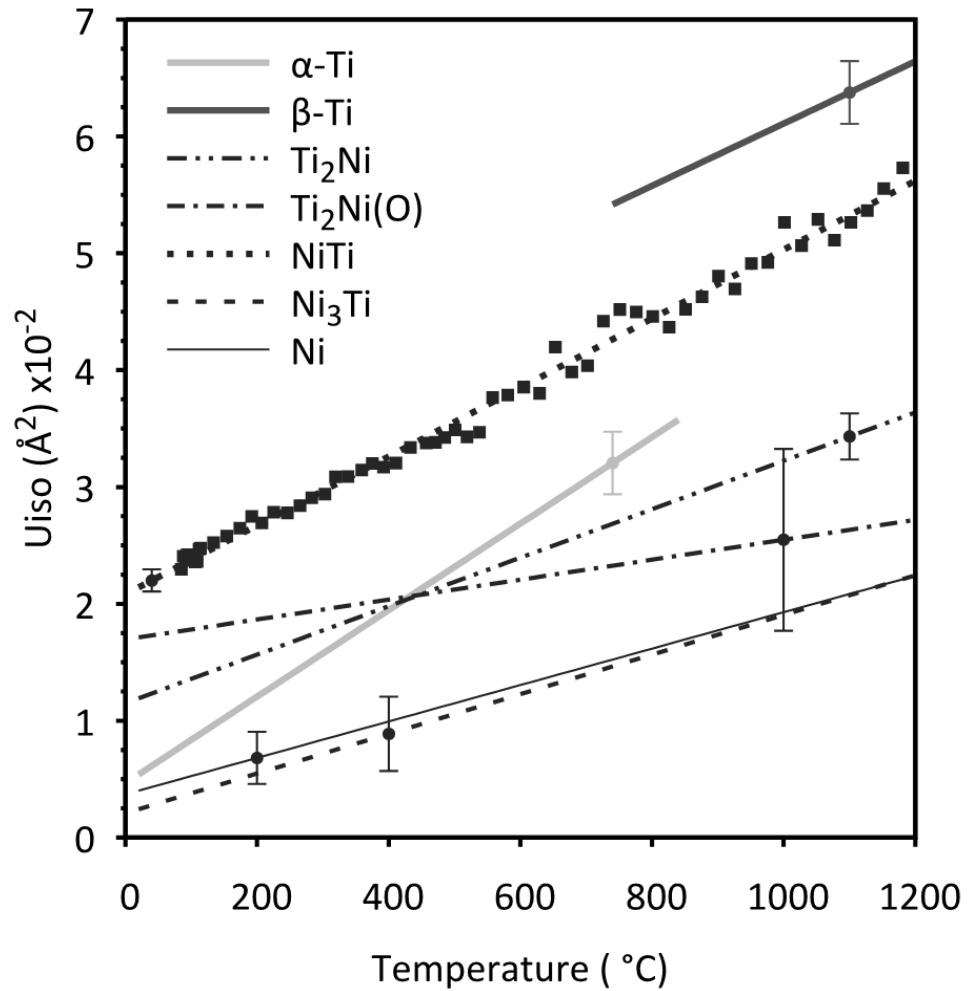
Figure 4-29   Modelled *U_iso* data used during Rietveld refinement of *RS1000* and *RS1200*.

The initial room temperature patterns were refined assuming only Mo, α-Ti and Ni were present. The (101) Ti peak overlapped the odd (110) Mo double peak reported earlier, as shown in Figure 4-27. A good fit could only be obtained by excluding this from the analysis. The detector zero-offset parameter and the structural parameters of the three phases were refined first, followed by the shape parameters and then the background. The weak crystallographic texture exhibited by Mo and α-Ti were modelled using the March-

Dollase correction. The U_{iso} values were input and not allowed to refine. With the 34°

peak excluded, R_{wp} was 8.6% for *RS1000* and 6.5% for *RS1200*.

The remaining composite patterns were split into groups of five (starting with the 500 °C

pattern). The first composite pattern in each group was refined first, after which the

remaining four composite patterns were refined in chronological sequence. During

sequential fitting, the structural parameters, the zero, the peak-shape parameters, and the

background were allowed to refine while the U_{iso} values were fixed. The first pattern in

each group (with the exception of the first group starting at 500 °C), had the same U_{iso}

values as the last pattern of the previous group (obtained as averages). The middle three

patterns all shared the same U_{iso} values (the U_{iso} values of the middle spectrum). A plot of

each pattern and the corresponding refinement was verified not only to ensure that a good

refinement had been obtained, but also to determine whether any phase(s) had

appeared/disappeared. When a phase was found to disappear, the refinement was

repeated without the phase. Conversely, when a phase was found to appear, it was added

to the refinement with the appropriate U_{iso} value. For minority phases with low volume

fractions, the refined lattice parameters were carefully monitored to ensure they did not

drift due, for example, to the presence of a majority phase with strong overlapping

diffraction peaks. Patterns where the quantity of $Ti_2Ni(O)$ reached approximately 5 wt%

were revisited to refine the occupancy parameter for interstitial O (the background was

fixed for this refinement). The U_{iso} value for $Ti_2Ni(O)$ was then adjusted. Typically, this

additional analysis resulted in a very small change in U_{iso} which did not significantly

impact either the O occupancy or the phase fractions. The largest R_{wp} values were 9.8%

for *RS1000* and 7.6% for *RS1200*. As an example of the quality of fit obtained for a given

R_{wp}, the observed and calculated patterns (with R_{wp} = 6.58%) for the 803 °C composite

pattern from the *RS1200* run are presented in Figure 4-30.
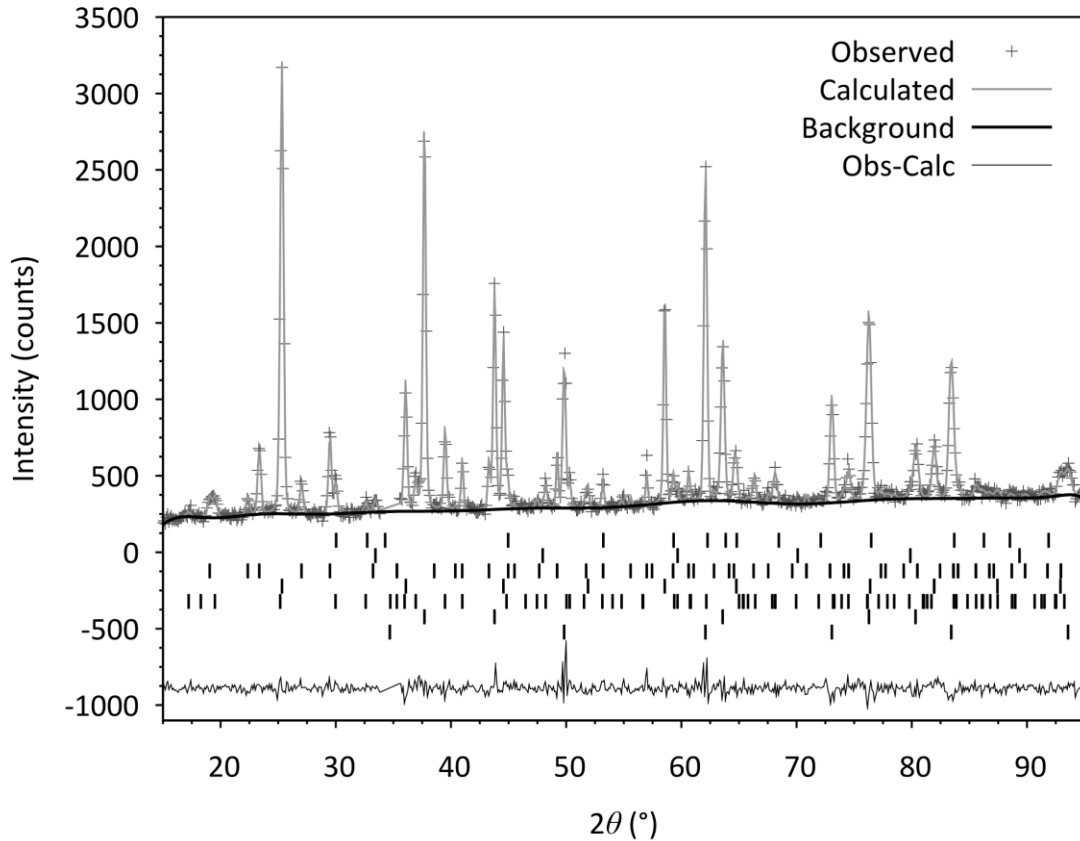
Figure 4-30 **Rietveld refinement of the 803 °C composite pattern from *RS1200* with an R_{wp} = 6.58%. From top to bottom the plane reflections are for the following phases: α-Ti, β-Ti, Ti₂Ni(O), NiTi, Ni₃Ti, Ni and Mo.**

Phase fractions were calculated based on the scale factors obtained from the refinements.

The scale factor of each phase (S_i) was transformed into a corresponding wt% phase

fraction (w_i) using the following equation [89]:

$$w_i = \frac{S_i \, m_i}{\sum_{i=1}^{n} S_i m_i},$$ (4-1)

115

where m_i is the mass of the unit cell of the ith phase. The contribution from the Mo crucible was left out such that n represents only the number of phases present in the specimen. For example, at room temperature in *RS1000*, the sum in the denominator only contained contributions from α-Ti and Ni ($n = 2$).

4.4.4   *Results and Discussion*

The diffraction patterns for *RS1000* and *RS1200* during heat up are presented in Figure 4-31 (*top* and *bottom*, respectively). The data are presented as film plots, in which each vertical line corresponds to the diffraction pattern corresponding to a 5°C temperature interval. In a given pattern (vertical line), the neutron counts have been converted into an 8-bit grayscale value with black (0) indicating the highest intensity. The peaks associated with the Mo crucibles have been removed for clarity.
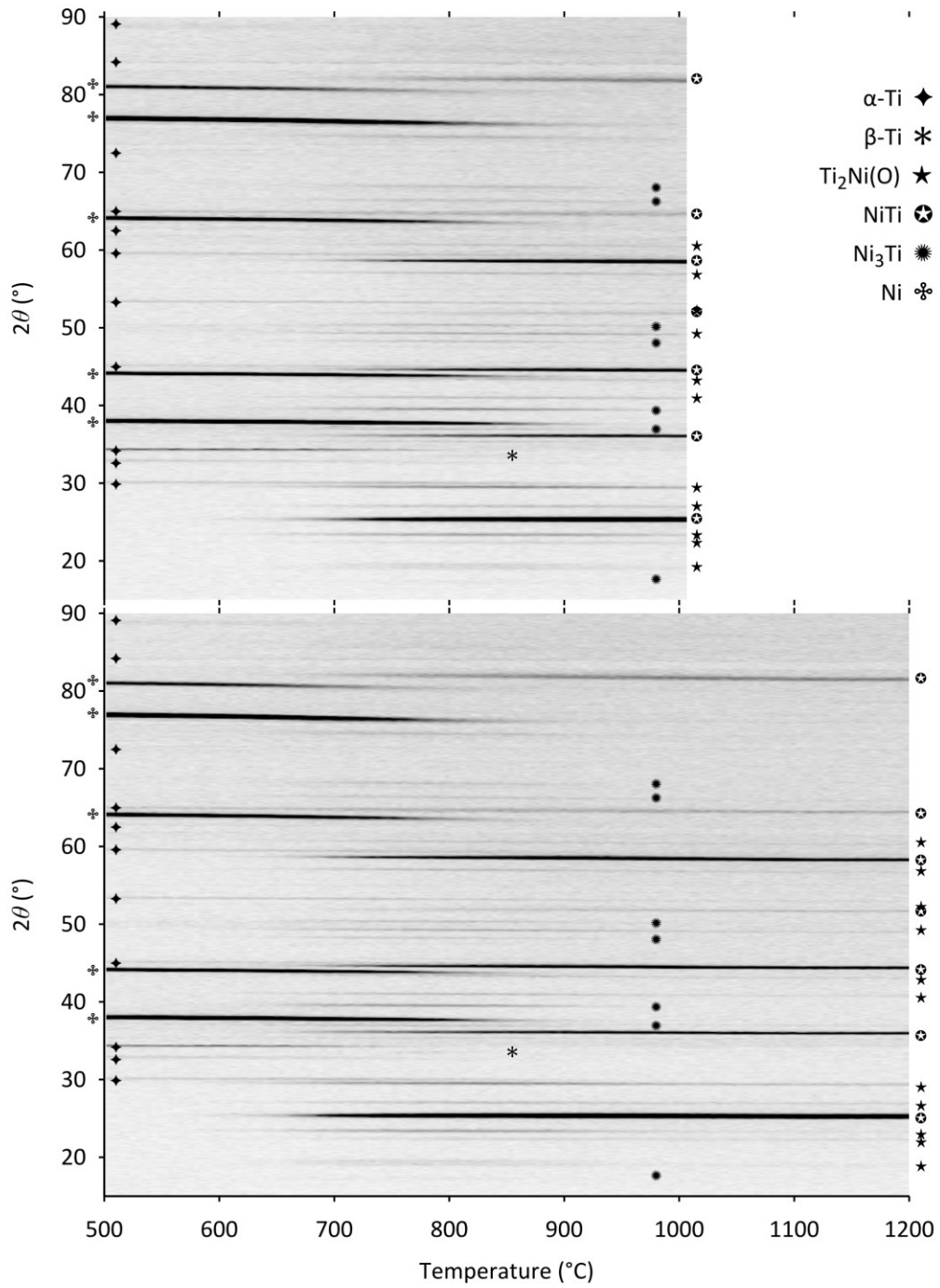
Figure 4-31   **Phase progression during sintering presented as 2-D film plots for:** *RS1000* **(top) and** *RS1200* **(bottom)**

The film plots for the two specimens are very similar up to 1000 °C, indicating good reproducibility for specimens of the same composition under similar sintering conditions. In both specimens, the microstructure does not begin to evolve until 600 °C, at which temperature the protective Ti surface oxide is thought to dissolve, allowing Ni-Ti inter-diffusion to occur [126]. As the temperature increases, all three intermetallic phases grow at the expense of the elemental phases. The elemental α-Ti phase transforms into β-Ti(Ni) and disappears at around 800 °C. By around 850 °C, β-Ti(Ni) is completely consumed. Elemental Ni disappears at a higher temperature, ~950 °C. In this temperature interval, NiTi grows significantly, with Ti_2Ni and Ni_3Ti growing to a lesser extent. A little above 1000 °C (Figure 4-31 *bottom*), Ni_3Ti also disappears, having been consumed by the growing NiTi phase. Ti_2Ni is never fully consumed. Since the powder composition was 49 at% Ni, and the minimum Ni content in NiTi is 49.6 at% Ni [124], Ti_2Ni is expected to remain in the microstructure until it melts at the peritectic temperature (984 °C). However, the results reveal that this phase does not melt but rather that it remains in the microstructure up to 1200 °C, the highest temperature investigated. This result has been reported previously by the authors [110,126] for the same composition, and by Cao and Liss [60–62] for a Ni rich composition (52 at% Ni) in which no remaining Ti_2Ni was expected. It was suggested Cluff, Gharghouri and Corbin [126] that this was due to O stabilizing the phase (the real phase is $Ti_2Ni(O)$).

4.4.5   *Rietveld Analysis*

In assessing the quality of Rietveld refinements, accuracy and reproducibility (precision) are two important aspects. A useful measure of accuracy is the uncertainty determined by

the difference between the calculated phase fraction and the true value. Unfortunately, the true phase fractions during sintering are not known. However, an estimate of the uncertainty was obtained using the results from the room temperature, 500, 520, 540 and 560 °C diffraction patterns of *RS1000*, *RS1200* and *95Ti/5Ni,* for which the true values for the phase fractions could be reliably assumed to be equal to the initial weighed mass fraction. The average uncertainty in the phase fraction was determined to be +/- 0.016. This value is acceptable given the constraints and goals of the experiment. It would have been lower had it been possible to include the strong Ti (101) peak in the refinements.

The reproducibility of the experimental results was assessed by comparing the phase fractions obtained from *RS1000* and *RS1200*. The phase fractions determined through Rietveld refinement are shown in Figure 4-32 *a* through *f,* in which the error bars correspond to the previously determined uncertainty. At almost every point in all phases, the uncertainties of the two runs overlap, indicating excellent reproducibility. The largest inconsistencies between the two samples occur in the β-Ti(Ni) phase fractions (Figure 4-32 *b*) These larger inconsistencies occur because : 1) β-Ti(Ni) has relatively few peaks within the scattering angle range covered by the detector, and 2) it represents a small part of the mixture, resulting in weak diffraction peaks. The excellent reproducibility of the results in Figure 4-32 provide confidence in both the Rietveld refinements, and in the consistency of the mixing, pressing and sintering of the compacts.
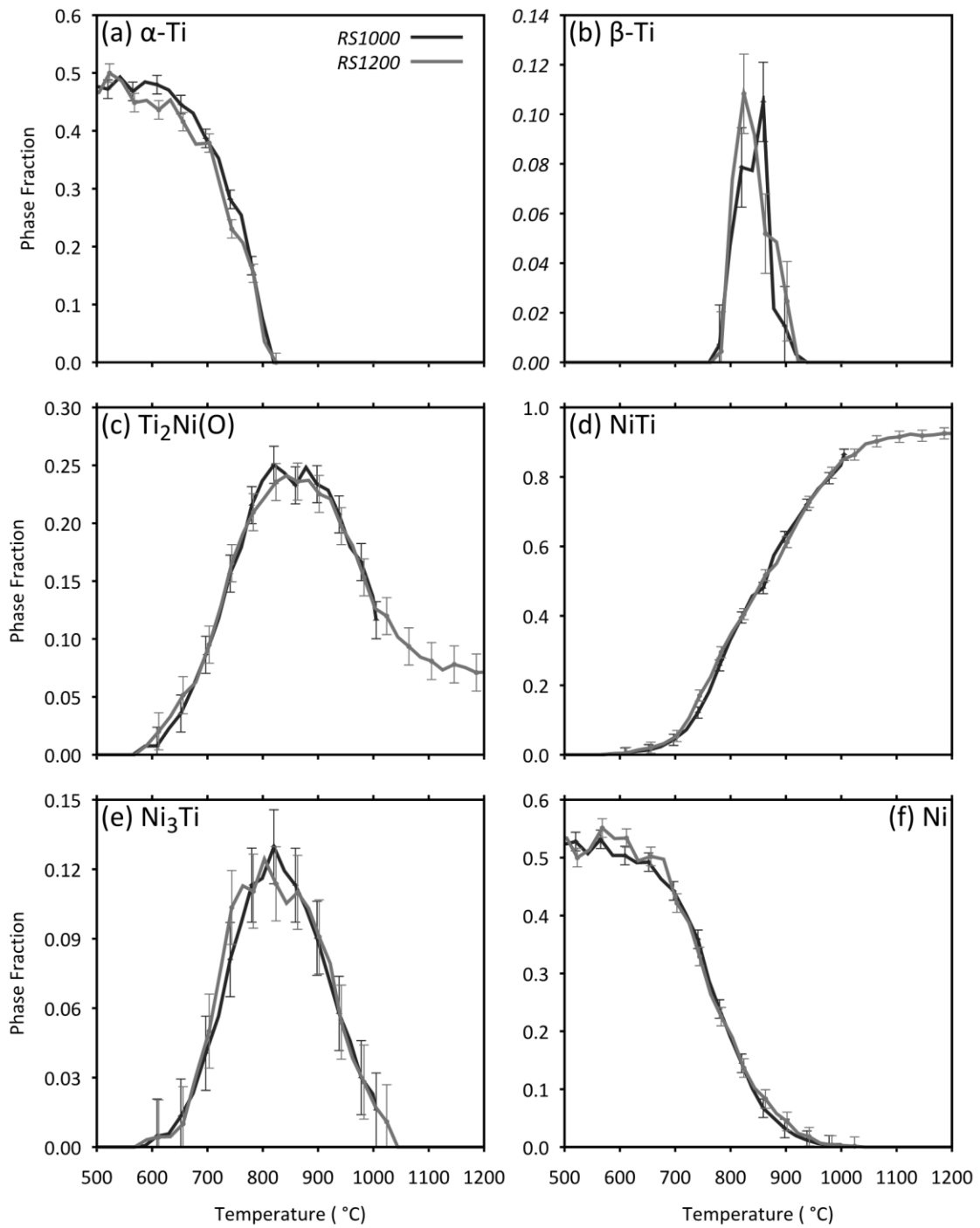
Figure 4-32   Comparisons of refined phase fractions for *RS1000* and *RS1200*.

In a previous publication, the authors examined the phase evolution during sintering based on an analysis of individual neutron diffraction peaks without the benefit of quantitative phase analysis afforded by a full-profile pattern refinement [126]. The present findings confirm the results of the previous work, but provide a more detailed picture of how the phases evolve during sintering due to the quantitative determination of the phase fractions (Figure 4-33). $Ti_2Ni(O)$ is the first intermetallic phase to form, at ~600°C. The other two intermetallic phases start to form at a similar temperature, but subsequently grow at a slower rate. At ~700 °C, NiTi starts growing rapidly, becoming the dominant phase by ~780 °C. The β-Ti(Ni) phase fraction peaks at approximately the same temperature at which α-Ti disappears (~830 °C). Once all the α-Ti transforms to β-Ti(Ni), the latter is consumed by the growing intermetallic phases. The phase fraction of Ni_3Ti peaks at around 820 °C, while that of $Ti_2Ni(O)$ peaks at ~850 °C. Ni takes longer to be fully consumed than elemental Ti, disappearing completely at ~960 °C. The last of the Ni_3Ti is converted to NiTi by 1050 °C. $Ti_2Ni(O)$ is never fully converted into NiTi. Rather, the phase fractions stabilize by ~1100 °C at ~93 wt% NiTi / 7 wt% $Ti_2Ni(O)$, and further homogenization is unlikely. It is not possible to determine how much $Ti_2Ni(O)$ to expect at equilibrium since no phase diagrams are available which include this phase at temperatures above 984 °C.
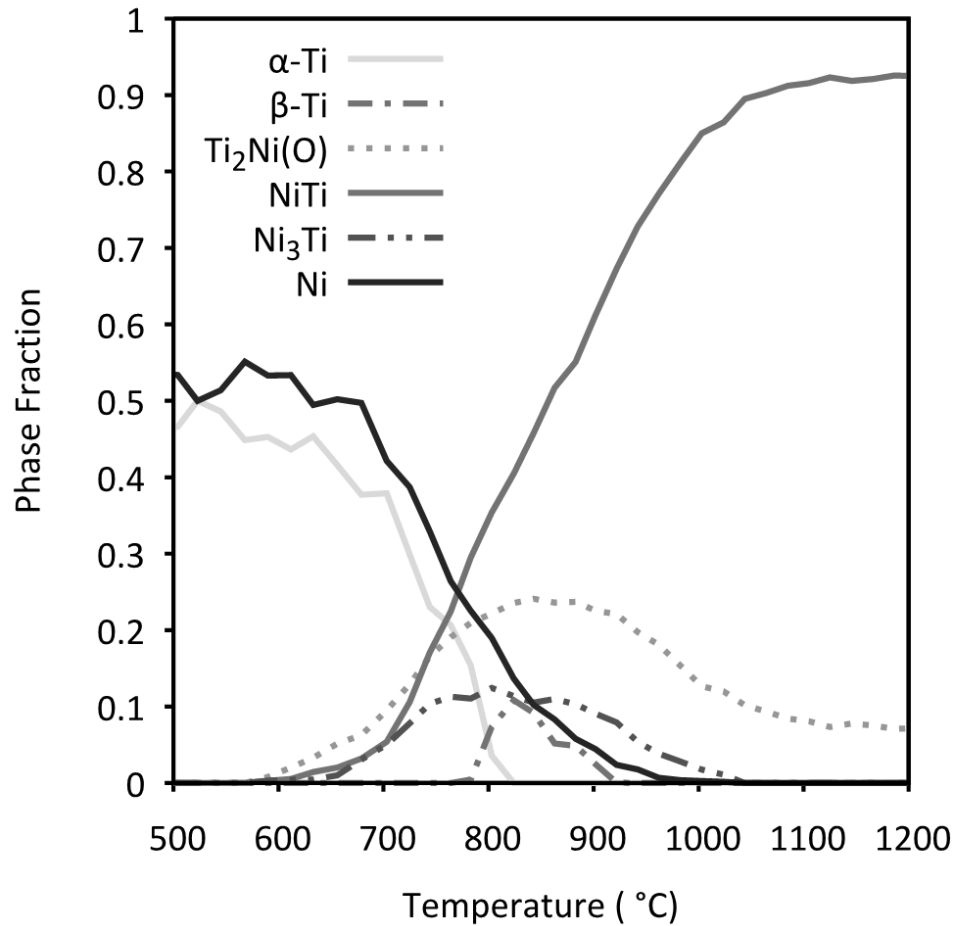
Figure 4-33   Phase progression in *RS1200* based on Rietveld refinements.

The phase progression during reactive sintering of NiTi from elemental powders presented by Chen, Liss and Cao [60] shows similarities to the one presented here. Despite holds at or below 530 °C, Chen, Liss and Cao found that intermetallic phase formation commenced only once the temperature approached ~570 °C (heating at 5 °C/min), reinforcing the idea that the formation of intermetallic phases cannot begin until the surface oxide on Ti dissolves and the O diffuses into Ti(O). Another similarity between the two studies is the presence of $Ti_2Ni(O)$ (labelled Ti_2Ni by Chen, Liss and Cao) above the peritectic temperature. Due to different starting Ni:Ti ratios in the two

studies, the phase progression differs as well. The Ni-rich mixture of Chen, Liss and Cao forms Ni_3Ti as the predominant intermetallic phase in the early stages of sintering vs. Ti_2Ni in the Ti-rich mixture. Also, the Ni_4Ti_3 phase forms in the Ni-rich mixture but not in the Ti-rich mixture of the current study. Finally, Chen, Liss and Cao observed a eutectoid decomposition $NiTi \rightarrow Ti_2Ni + Ni_3Ti$ at 617 °C during cooling. In contrast, the 2-D film plot of *RS1200* during cooling (Figure 4-34) shows neither the growth of Ti_2Ni nor the reappearance of Ni_3Ti in the Ti-rich mixture. The horizontal dashed line in Figure 4-34 indicates the start of the transformation from the NiTi austenite phase (B2) to the NiTi martensite phase (B19') at 82 °C. This temperature is higher than the typical M_s temperature (65 °C) reported in the literature for Ti-rich NiTi [6]. This discrepancy can be explained by the difference in cooling rates. The cooling rate obtained through furnace cooling in the present study is 0.3 °C/min compared to 5 °C/min or higher in many of the other studies. Tang [6], through thermodynamic modelling determined that B19' is stable below 97 °C but requires undercooling for nucleation. The slow heating rate provides ample time for the transformation to occur at higher temperatures despite a smaller nucleation rate.
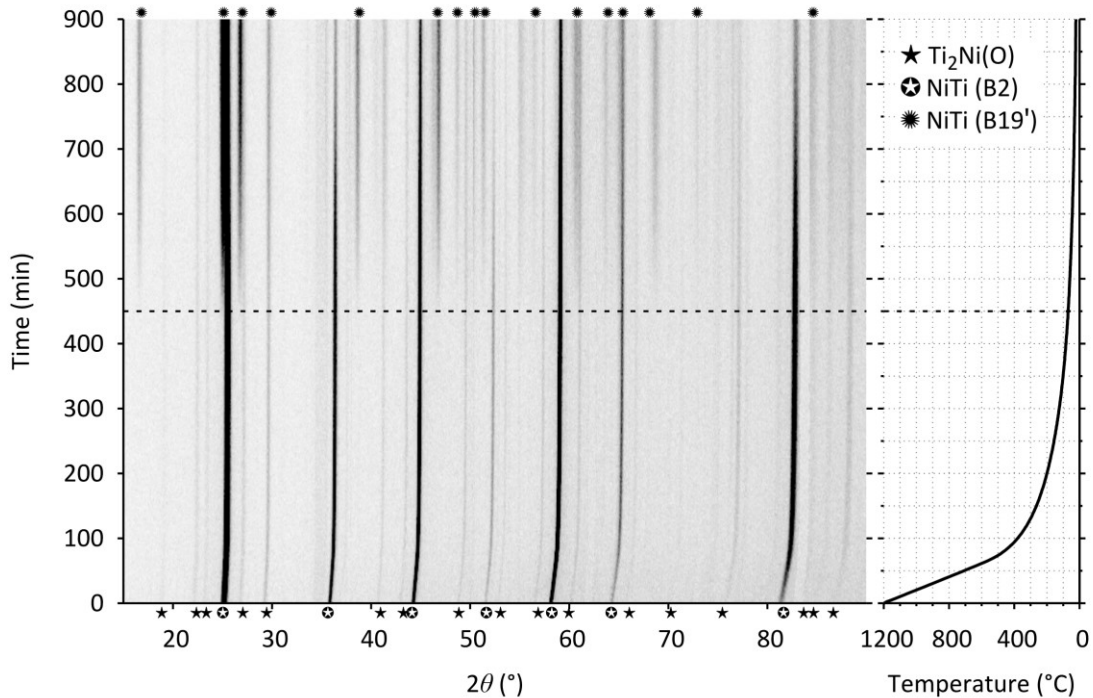
Figure 4-34 ***RS1200* phase progression during cool down presented as a 2-D film plot. The dashed line indicates the start of the diffusionless transformation in NiTi from austenite (B2) to martensite (B19').**

The full-profile refinements in the present study provide new insights into the nature and behavior of the $Ti_2Ni(O)$ phase. Currently, in the literature, there is confusion about the oxygen-containing phase, considered to be $Ti_4Ni_2O/Ti_4Ni_2O_x/Ti_2Ni(O)$ with a similar crystal structure to that of Ti_2Ni. There is no information on how and when the phase(s) appears and evolves, and the peritectic at 984 °C adds to the confusion. That the two phases are in fact the same phase - Ti_2Ni with O in solution - is evidenced by the progression of the peak shapes. Figure 4-35 shows how the low angle $Ti_2Ni(O)$ peaks shift consistently with increasing O content as the temperature increases. The (311), (222) and (400) peaks (22.3°, 23.3° and 27°, respectively) all increase in intensity up to 900 °C, at which β-Ti(Ni) disappears from the microstructure and the phase fraction of $Ti_2Ni(O)$ begins to decline (Figure 4-33). Above 900 °C, the relative intensity of the (222) peak

decreases while the relative intensities of the (311) and (400) peaks increase (see Figure 4-28). There is no peak broadening, and no new peaks, as would be expected if two distinct phases were present.
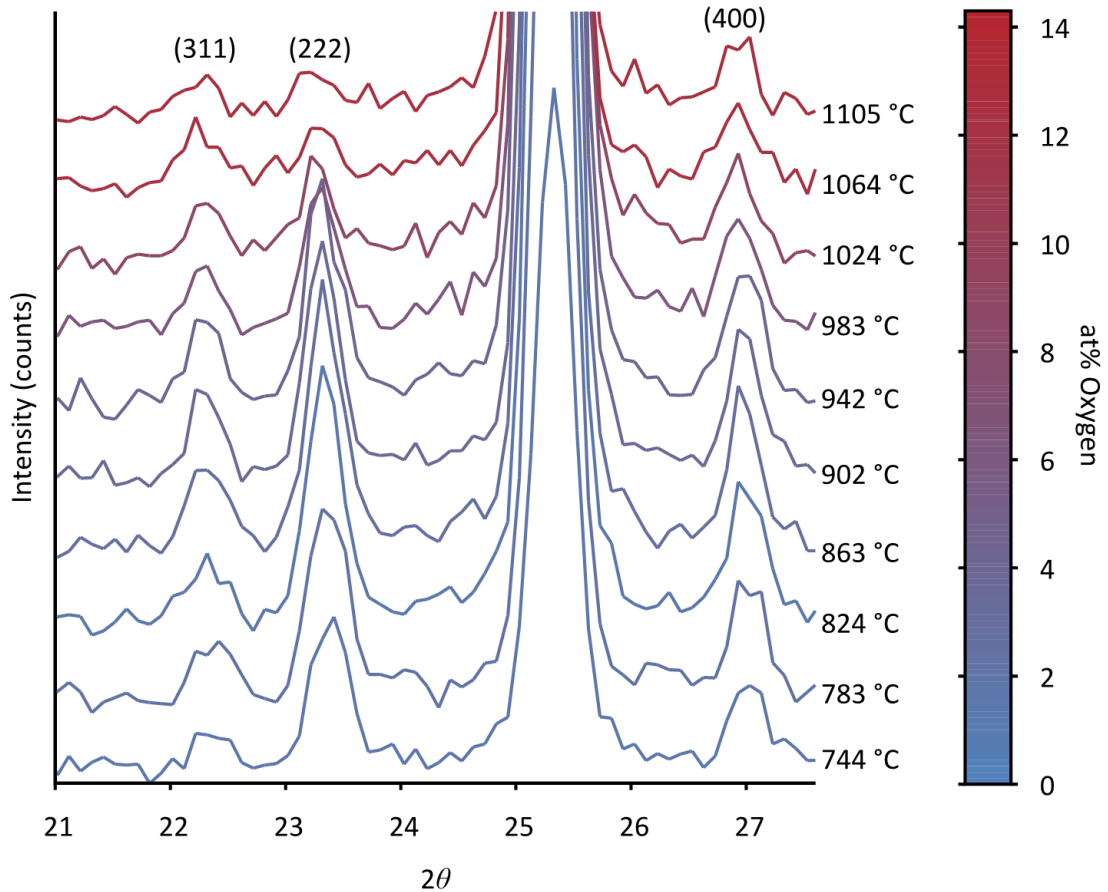
Figure 4-35   **Evolution of Ti₂Ni(O) peaks as O concentration increases with temperature: (311) at 22.3°, (222) at 23.3° and (400) at 27°). At% O determined through Rietveld refinements.**

Figure 4-36 shows the O concentration in Ti₂Ni(O) as a function of temperature in *RS1000* and *RS1200* determined from the Rietveld refinements, where the error bars are the standard uncertainty. As with the phase fractions, there is excellent agreement between the two separate runs. The Ti₂Ni(O) phase initially contains little oxygen

(approximately 2 at%). The oxygen concentration slowly increases to 4 at% by 900 °C, above which it increases rapidly, nearly doubling every 100 °C. The oxygen concentration stabilizes at 14 at% (equivalent to Ti_4Ni_2O) during the 1000 °C hold in *RS1000,* and at 1100 °C in *RS1200* (the temperature at which the phase fraction of $Ti_2Ni(O)$ stabilizes).
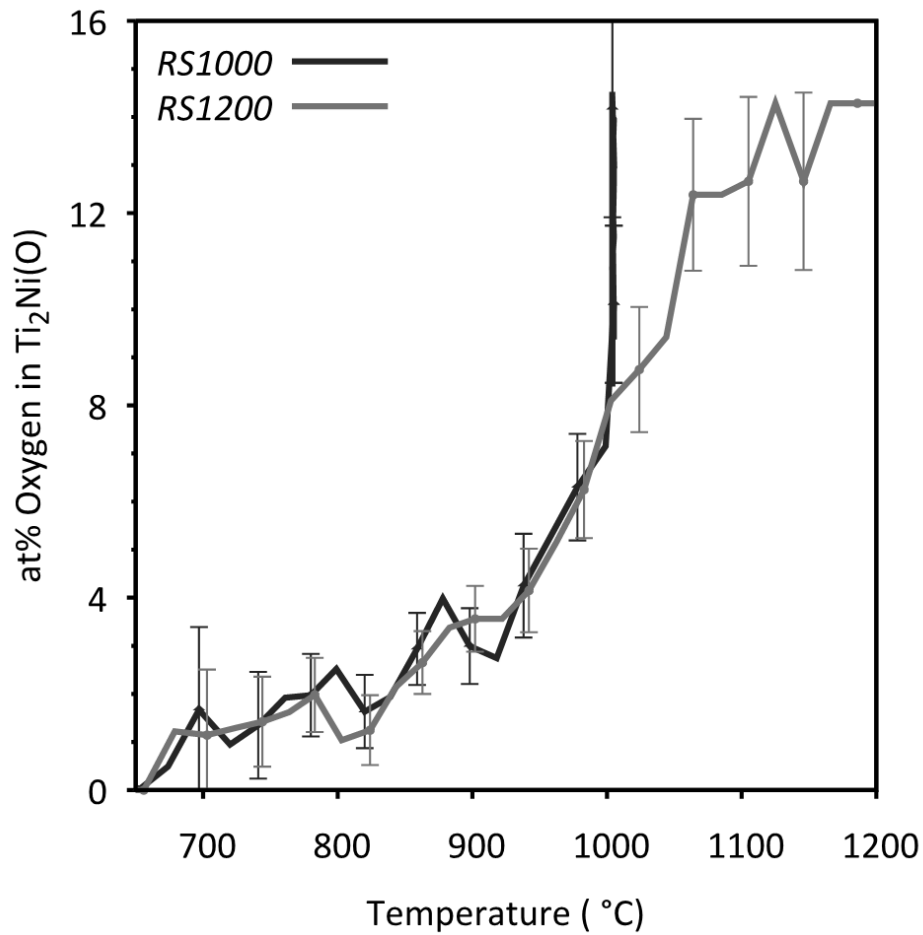
Figure 4-36   Evolution of O concentration in $Ti_2Ni(O)$ with temperature from Rietveld refinements.

This study clarifies the nature and origin of the $Ti_2Ni(O)$ phase found in post-sintered microstructures. Of the three intermetallic phases, the solubility of oxygen is highest in

126

Ti$_2$Ni(O) and lowest in NiTi [43]. It is proposed that O preferentially segregates to Ti$_2$Ni(O) such that, as Ti$_2$Ni(O) consumes the β-Ti(Ni) phase, it also incorporates the O in that phase. In contrast, when NiTi consumes Ti$_2$Ni(O), it incorporates little or none of the oxygen from Ti$_2$Ni(O). Therefore when it first forms, Ti$_2$Ni(O) contains little, if any, oxygen. As it consumes the elemental Ti phase, it incorporates the oxygen from the elemental Titanium, however the absolute quantity of Ti$_2$Ni(O) also increases such that the relative amount of O in solid solution remains low. This changes once all the β-Ti(Ni) is consumed and the weight fraction of Ti$_2$Ni(O) begins to decrease. The result is a decrease in the absolute quantity of Ti$_2$Ni(O), with no change in the total oxygen content, leading to an increased O concentration in the remaining Ti$_2$Ni(O). Thus, Ti$_2$Ni(O) is very difficult to remove entirely because Ti$_2$Ni forms naturally during reactive sintering, and evolves easily into the thermodynamically stable/metastable Ti$_2$Ni(O) phase with only small amounts of oxygen in the system. The persistence of Ti$_2$Ni(O) (reported as Ti$_2$Ni) above the peritectic temperature is evident even in Ni-rich mixtures (52 at% Ni) [60]. The affinity of the Ti$_2$Ni(O) phase for O indicates that effective ways of reducing the amount of Ti$_2$Ni(O) in the final microstructure would be to reduce the O content of the starting powders, or to reduce the powders in the green compacts prior to heating to the sintering temperature. A comparison of the total wt% oxygen in the green state (.7 wt O in Ti and 0.13 wt% O in Ni) with the quantity of oxygen tied up in Ti$_2$Ni(O) (a fully occupied interstitial site equates to 4.9 wt% O in Ti$_2$Ni(O), which in turn makes up ~ 7.5 wt% of the total mass, Figure 4-33) after sintering (0.39 wt% O vs 0.38 wt% O respectively) underscores the importance of reducing the oxygen in the starting powders.

The O in $Ni_2Ti(O)$ likely enhances the stability of the phase above the peritectic temperature. Indeed, the neutron diffraction data show that, there is no drastic drop in the phase fraction of this phase at the peritectic temperature, indicating that no melting occurs. The degree to which O shifts the melting temperature of $Ti_2Ni(O)$ is not known, requiring tests at higher temperatures than 1200°C.

4.4.6 *Conclusions*

Rietveld refinement of neutron diffraction patterns obtained *in-situ* during the reactive sintering of Ni-Ti (49 at% Ni : 51 at% Ti) elemental powder compacts was performed for two different sintering profiles. The atomic displacement parameter (U_{iso}) and the lattice parameters for each phase that occurs during reactive sintering (α-Ti , β-Ti(Ni), $Ti_2Ni(O)$, NiTi, Ni_3Ti and Ni) were obtained from separate *in-situ* experiments on stoichiometric powder mixtures. The determination of accurate U_{iso} values from separate experiments was found to be particularly important for the successful refinement of minority phases. Diffraction peaks from minority phases often suffered from peak overlap in the NiTi mixture, leading to poorly refined lattice parameters. Prior knowledge of the lattice parameters for each phase ensured that these errors could be identified and corrected. The reproducibility of the analysis was excellent, as demonstrated by the consistency of results obtained for the two different sintering profiles. The uncertainty in the weight percent of each intermetallic phase was determined to be 0.016 wt%.

Intermetallic phase formation did not begin until the oxide layer surrounding Ti particles dissolved at 600 °C. During the early stages of sintering, $Ti_2Ni(O)$ was the fastest growing intermetallic phase. NiTi became the dominant phase by 780 °C and it continued

to grow at the expense of all the other phases. The final microstructure consisted of a combination of NiTi and $Ti_2Ni(O)$. While Ti_2Ni has a melting temperature of 984 °C, the present neutron diffraction results indicate that interstitial O raises the melting point of the $Ti_2Ni(O)$ phase up to at least 1200 °C (the highest temperature investigated).

Refinement of the oxygen concentration in $Ti_2Ni(O)$ during sintering, expressed as the occupancy of the oxygen interstitial sites, has led to a better understanding of why $Ti_2Ni(O)$ is always found after sintering from elemental powders. During the initial stages of sintering, $Ti_2Ni(O)$ with little or no O is formed. As the amount of this phase increases, its O content also increases, likely as a result of accepting O from the elemental Ti that it consumes as it grows. A significant increase in O concentration occurs when the phase fraction of $Ti_2Ni(O)$ starts to decrease, since, as NiTi consumes $Ti_2Ni(O)$, the O remains in $Ti_2Ni(O)$. The O raises the melting point of $Ti_2Ni(O)$, making it extremely difficult to remove.

4.5 THERMAL EXPLOSION MODE OF SELF-PROPAGATING HIGH-TEMPERATURE SYNTHESIS (TE-SHS) IN COARSE POWDERS

4.5.1 *Experimental method*

Two Ni-Ti powder blends were prepared at a composition of 49 at.% Ni with the balance Ti. The first blend was an RA Ti – F Ni blend hereafter referred to as RA mixture. The second was an HP Ti – C Ni mixture hereafter referred to as CNi mixture. The two blends investigated had one coarse component and one finer component to limit solid-state sintering and promote TE-SHS while the two blends were chosen to investigate the

influence of the Ni and Ti powder size ratio on sintering behaviour. Their respective green microstructures are presented in Figure 4-4.

A 4.76 mm diameter die was used to uniaxially compact the disc shaped specimens required for the DSC sintering investigations. The specimens were compacted at 860 MPa. Sintering of the discs was performed in-situ in a Netzsch 404 F1 high temperature differential scanning calorimeter (DSC) under a high purity Ar atmosphere. The following two thermal profiles were used: (1) heating to 1050 °C at 20 °C/min and cooling and, (2) heating to 500 °C at 20 °C/min followed by heating to 1200 °C at 2 °C/min and cooling.

Pellets for neutron diffraction were uniaxially compacted in a 6.35 mm diameter die to a pressure of 620 MPa. With approximately 1 g of powder, this resulted in pellets that were around 10 mm in length. Three pellets were sintered together in a Mo crucible. The specimens were sintered by heating at 18 °C/min to 500 °C, then heating to 1200 °C at 2 °C/min, followed by furnace cooling.

Rietveld refinement of the ND data was carried out according to Section 4.4.3.

4.5.2   *Results and Discussions*

4.5.2.1 DSC

Initially each powder blend was sintered in the DSC by heating to 1050 °C at 20 °C/min. The resulting DSC traces are shown in Figure 4-37. Inset in Figure 4-37 is a close up of the heat-up traces from 600 °C to 1050 °C. Little change to the baseline can be seen in

either trace until 700°C. At 700°C both blends show a slight exothermic shift in the baseline rising to a peak at 765°C. At 765°C the traces show a slight endothermic dip. In previous work [33] this dip was associated with the reverse eutectoid reaction α-Ti + Ti$_2$Ni → β-Ti (see Figure 1-1), indicating that some metallurgical interaction between the elemental powders has already occurred by 765 °C. In the middle of the eutectoid transformation we see an exothermic rise followed by a levelling off until 945 °C. At around 945 °C in the RA mixture, a large exothermic peak associated with the thermal explosion mode of self-propagating high temperature synthesis (TE-SHS) occurs [32,33]. In the CNi mixture the TE-SHS exotherm is delayed by 20 °C. The CNi mixture produces the largest TE-SHS exothermic peak. At the tail end of the TE-SHS peak in the RA mixture a visible endothermic peak starting at ~984 °C occurs. On cooling each trace shows an exothermic peak that starts at ~984 °C.
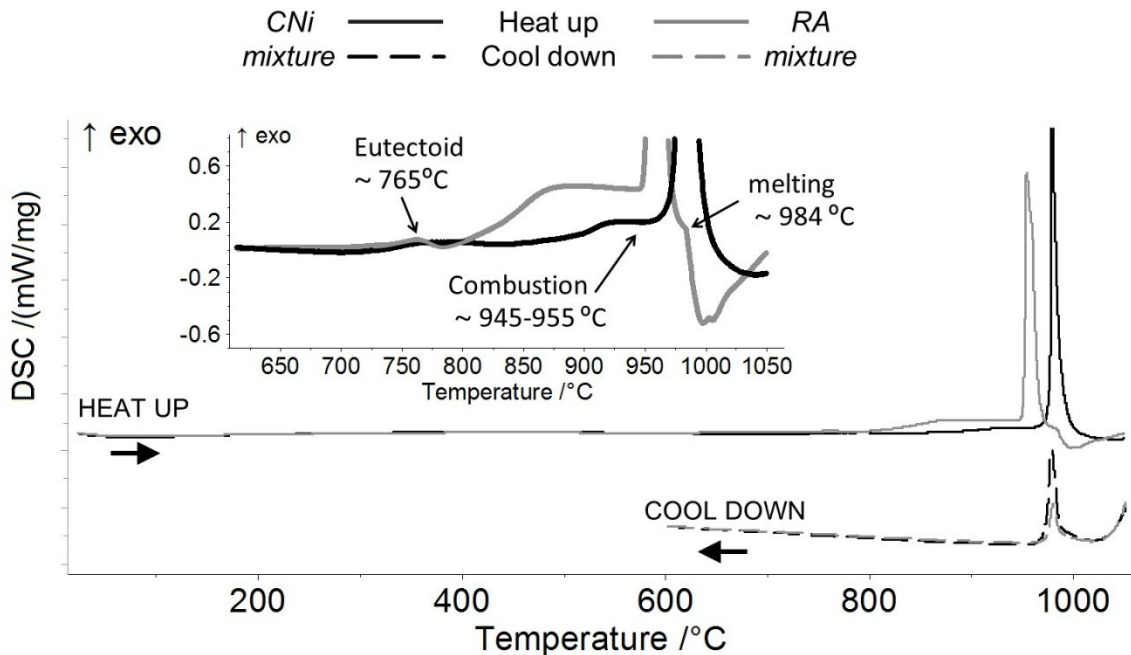
Figure 4-37 **DSC traces for the two powder mixtures heated to 1050 °C at 20 °C/min with a magnified view for 600°C - 1050°C inset**

The DSC traces provide a significant amount of information regarding the sintering behaviour of the powders. The exothermic shift in each baseline commencing at ~ 700 °C is thought to be due to the formation of the intermetallic phases Ti_2Ni, $NiTi$ and Ni_3Ti (Figure 1-1) [112].The traces show that little intermetallic phase formation occurs in the temperature range in which the Ti powders are in the α-Ti phase state. Intermetallic phase formation increases when the Ti powders transform to β-Ti. The reason for this is not currently known. On the one hand, the solubility of Ni is greater in β-Ti than in α-Ti; on the other hand, the diffusion of Ni is slower in β-Ti than in α-Ti [117]. In addition, the self-diffusion of Ti is three orders of magnitude faster in pure β-Ti than in pure α-Ti at the 882 °C transformation temperature [127]. Thus, while the increasing temperature is expected to increase diffusion, it is postulated that the difference in intermetallic

formation behaviour is partly due to the different rates of Ti self-diffusion. Verification of this assumption requires further research which is beyond the scope of this study.

The β-Ti + Ti$_2$Ni reverse eutectic reaction occurs at 942°C. The microstructural evolution leading up to TE-SHS for a similar RA mixture [32] and a CNi mixture [33] is described in depth by Whitney *et al* [32,33], who linked the onset of TE-SHS with the formation of liquid. Although no melting endotherm is visible in Figure 4-37 from either sample, liquid at the β-Ti - Ti$_2$Ni interface is still believed to be present prior to TE-SHS. The two studies of Whitney *et al.* show that the main difference in TE-SHS between the two blends used is a larger volume fraction of β-Ti at the eutectic composition (~ 9 at% Ni) in the RA mixture at 942 °C. In the RA mixture, the Ti core maintains Ni saturation up to the eutectic temperature. In the CNi mixture, however, the small surface area to volume ratio of the Ni powder restricts the diffusion of Ni into Ti. The majority of the β-Ti phase is thus not at the eutectic composition at the equilibrium eutectic temperature, resulting in less liquid formation at this temperature than in the RA mixture. The enthalpies associated with the TE-SHS reaction measured from the traces in Figure 4-37 are listed in Table 4-5. The TE-SHS enthalpy under similar sintering conditions as the RA mixture has been correlated in the literature to the amount of β-Ti present at the eutectic temperature [32]. Accepting this correlation, the data in Table 4-5 thus indicate that the β-Ti content in both blends in the current work is similar. A closer inspection of Figure 4-37 indicates that the TE-SHS peak of the CNi mixture spans over the temperature range of the Ti$_2$Ni endothermic melting peak which is visible in the RA mixture. Since the enthalpy of the RA mixture peak does not incorporate this endothermic peak, the enthalpy associated with TE-SHS is accurate for this sample. With the overlapping

exothermic and endothermic events in the CNi mixture the enthalpy of the exothermic reaction is larger than calculated using the DSC trace. It is expected that in reality there is more β-Ti present in the CNi mixture when TE-SHS occurs than in the RA mixture. The endothermic peaks on cooling at 984 °C show that liquid is still present in both the RA mixture and the CNi mixture after the TE-SHS peak. Of note is that, despite not showing a melting peak on heating, the CNi mixture has the largest solidification peak indicating it contains the highest mass fraction of liquid above 984 °C.

Table 4-5   **TE-SHS combustion enthalpies for both powder mixtures at 20 °C and**
2 °C

Heating rate	Enthalpy (J/g)	
(°C/min)	RA mixture	CNi mixture
20	-247	-240
2	-140	-170

This interpretation of the DSC traces is supported by the macroscopic evidence shown in Figure 4-38. The RA mixture has a very coarse pore structure (Figure 4-38 a)) suggesting the C Ti particles melted during TE-SHS leaving a rigid intermetallic structure which roughly maintained its shape.
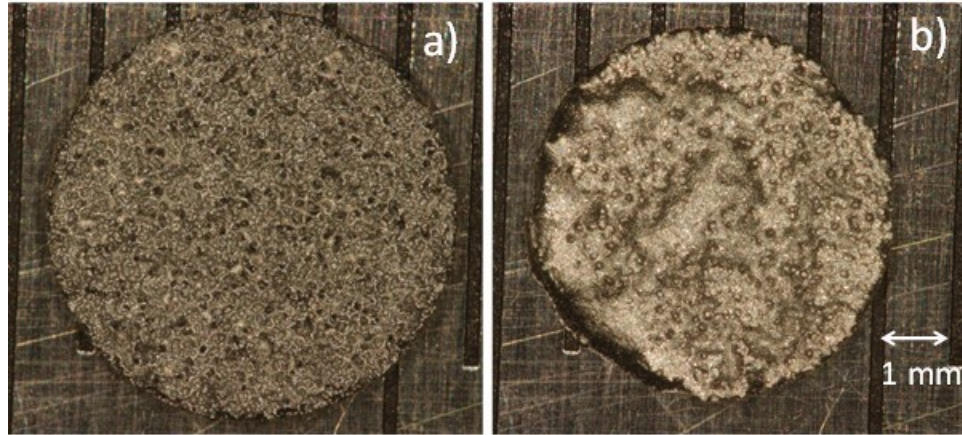
Figure 4-38 **Macroscopic images of the RA mixture (a) and the CNi mixture (b) DSC compacts after sintering at 20 °C/min**

The CNi mixture (Figure 4-38 b)) lost much of its shape. Although difficult to tell from the angle shown, the compact had slumped in some areas leaving a compact that was very uneven in height. In the investigation by Biswas [46] the slumping was due to a melting of the intermetallic structure. If this is the case the real temperature of the specimen would have to have been above the Ni rich eutectic at 1115 °C to liquefy all the intermetallic phases.

While much information can be obtained from a DSC trace it is very difficult to establish the contribution of each phase. In-situ neutron diffraction offers this possibility but the time required to acquire a good quality spectrum is much longer than to record a temperature. To this end a heating rate of 2 °C/min was used for the neutron diffraction experiments. However, a slower heating rate provides more time for phase evolution, with the attendant possibility that all the β-Ti would be consumed prior to the Ti-rich eutectic temperature being reached. DSC was thus used to ensure that TE-SHS would still occur in the powders used here. The DSC traces for specimens heated at 2 °C/min are

135

presented in Figure 4-39. It is clear that TE-SHS still occurs in both the RA mixture and the CNi mixture. The enthalpies of the TE-SHS peaks are given in Table 4-5. The lower enthalpies associated with the lower heating rate suggest that the slower heating rate allowed for increased intermetallic formation with a resulting decrease in β-Ti content prior to the Ti-rich eutectic temperature of 942 °C. Based on the prior discussion the RA mixture has less β-Ti than the CNi mixture at 942 °C. Neither trace shows any sign of a Ti_2Ni melting endotherm at 984 °C. An endothermic peak occurs in the CNi mixture at the 1115 °C $NiTi$-Ni_3Ti eutectic temperature. Liquid remains present in the specimen until it is cooled below the eutectic point whereupon the liquid solidifies, as is evident from the exothermic solidification peak in the cool down trace. This would indicate that there is still Ni_3Ti present in the CNi mixture whereas in the RA mixture the Ni_3Ti has been consumed.
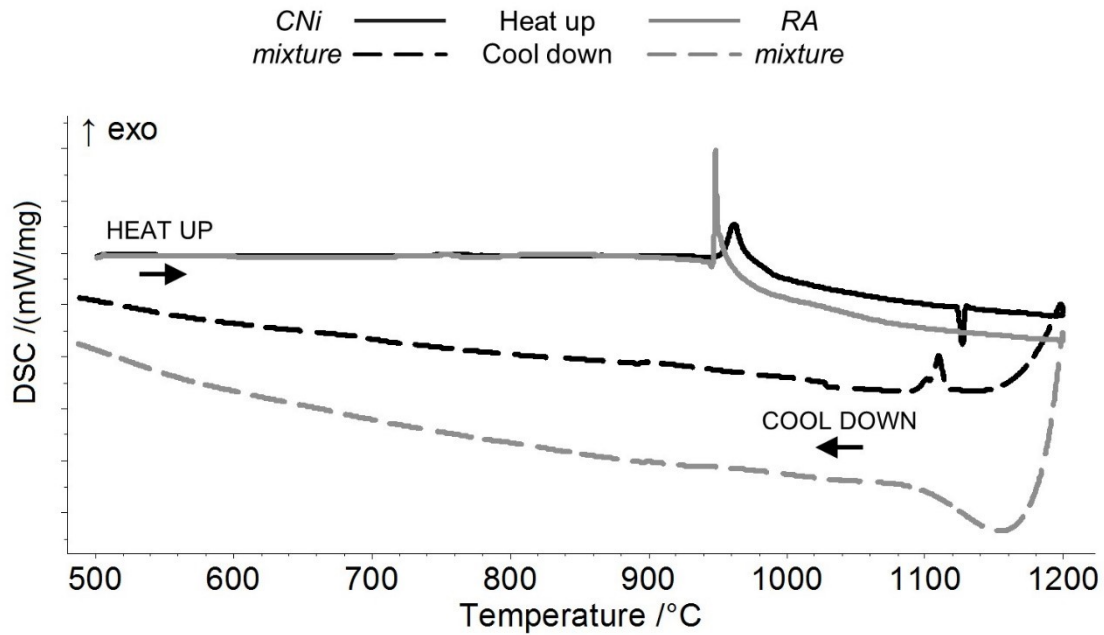
Figure 4-39   DSC traces for the two powder mixtures heated to 1200 °C at 2 °C/min from 500 °C

The shapes of the compacts post sintering at 2 °C/min are very similar to those of the compacts sintered at 20 °C/min (Figure 4-40). In the RA mixture (a) pores visible on the specimen surface are smaller than for the higher heating rate. This is due to the increased solid state diffusion and a reduction in the amount of β-Ti present at 942 °C. The CNi mixture (b) again showed significant slumping. The white circle in Figure 4-40 b) highlights a hole in the post-sintered compact. Due to the size of the specimen in relation to the crucible the liquid flowed to the bottom leaving some solid phases at the top resulting in a heterogeneous compact. From these results precautions were taken to minimize crucible-liquid interaction during the in-situ neutron diffraction experiments. While the information gleaned from the DSC traces and the macroscopic images is very useful, it lacks the in-situ information about phase evolution that in-situ neutron diffraction can provide.
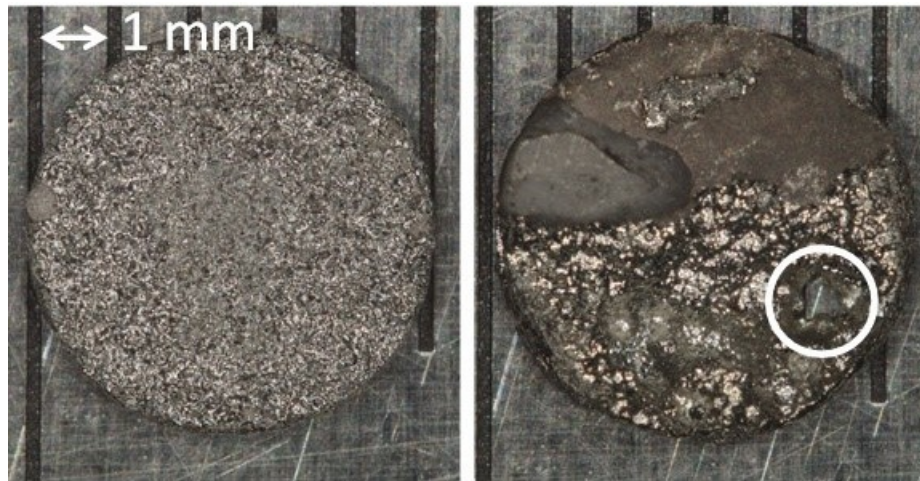
Figure 4-40 **Macroscopic images of the RA mixture (a) and the CNi mixture (b) DSC compacts after sintering at 2 °C/min**

4.5.2.2 Neutron Diffraction

The macroscopic images of the samples used in the neutron diffraction experiments are shown in Figure 4-41. The RA mixture samples showed similar characteristics to those exhibited by the DSC compacts. The pellets expanded radially and stuck to the crucible wall. The CNi mixture samples had melted completely and re-solidified, filling the bottom of the Mo crucible. Unlike in the DSC sample, the neutron diffraction samples filled the majority of the crucible. As a result, when liquid formed and the compact slumped, it was enough to fully submerge the whole blend.
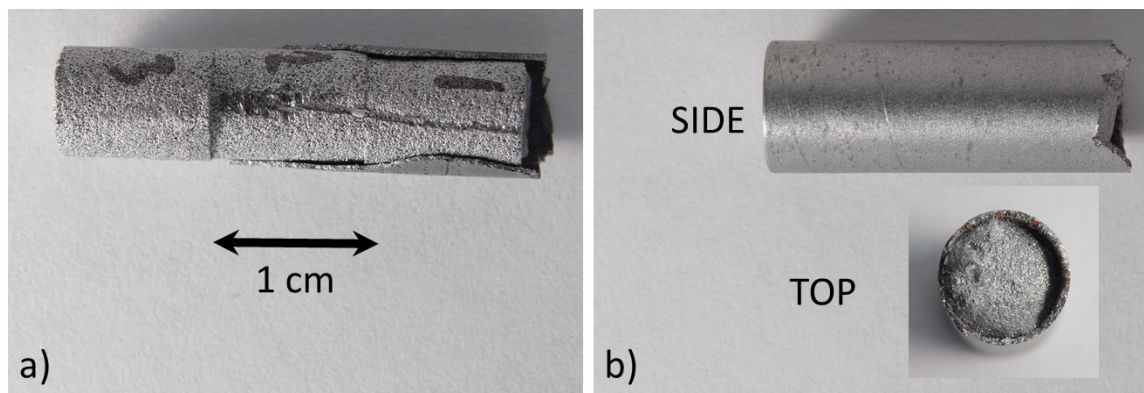
Figure 4-41 **Macroscopic images of the RA mixture (a) and the CNi mixture (b) ND pellets after sintering at 2 °C/min**

The neutron diffraction data obtained from the in-situ experiments are presented as film plots for the CNi mixture and the RA mixture in Figure 4-42. The film plots present a qualitative overview of the phase progression. Each horizontal line in a film plot represents a complete diffraction pattern captured over a 5 °C range. The neutron count for a given scattering angle is displayed as a 256-level grayscale pixel, with black

corresponding to the highest count. Peaks associated with the Mo crucibles have been removed from the figures for clarity.

Little difference was observed in the phase progression of the CNi mixture and the RA mixture up to 700 °C (Figure 4-42). Above 700 °C NiTi began to form in the CNi mixture evidenced by the peaks associated with NiTi slowly increasing in intensity as the temperature increased. Peaks associated with the $Ti_2Ni(O)$ and Ni_3Ti were near invisible. In the RA mixture peaks associated with all three intermetallics were present above 700 °C increasing in intensity at a quicker rate than was evident in the CNi mixture.
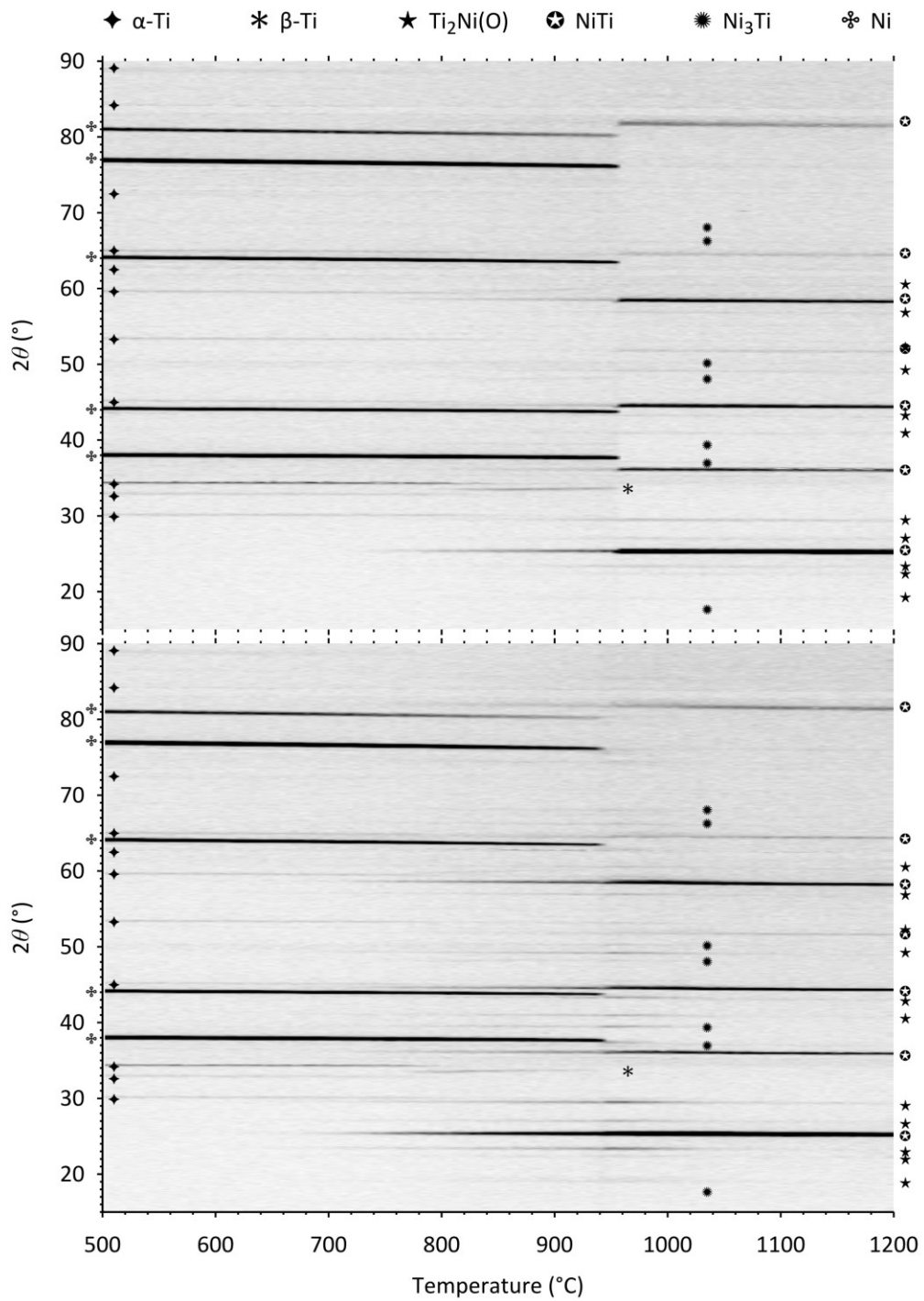
Figure 4-42 **Phase progression during sintering presented as 2-D film plots for:** *CNi mixture* **(top) and** *RA mixture* **(bottom)**

140

At approximately 765 °C α-Ti in the RA mixture slowly converted to β-Ti. Comparatively this phase transformation was delayed to ~ 800 °C in the CNi mixture. Also around 800 °C faint lines for $Ti_2Ni(O)$ and Ni_3Ti began to appear in the CNi mixture. The quicker rate of intermetallic formation in the RA mixture lead to the disappearance of the elemental α-Ti phase at lower temperatures (~ 800 °C vs. ~ 860 °C) and reduced phase fraction of β-Ti compared to the CNi mixture.

Both specimens underwent TE-SHS with the onset occurring at 942 °C in the RA mixture (see Figure 4-7) compared to 955 °C in the CNi mixture (see Figure 4-8). In both mixtures peaks associated with the elemental phases (β-Ti and Ni) disappeared rapidly while the peaks associated with NiTi showed a rapid increase in intensity. The impact of TE-SHS on the $Ti_2Ni(O)$ and Ni_3Ti varied significantly between the two mixtures. In the CNi mixture TE-SHS had little effect on the intensity of $Ti_2Ni(O)$ while what little Ni_3Ti was present disappeared. In the RA mixture both $Ti_2Ni(O)$ and Ni_3Ti increased in intensity.

Heating beyond 1000 °C showed little change in the CNi mixture up to 1200 °C. Both NiTi and $Ti_2Ni(O)$ were present at 1200 °C. In the RA mixture further heating results in the reduction of $Ti_2Ni(O)$ and the elimination of Ni_3Ti such that beyond ~ 1050 °C little change was observed in the diffraction patterns. Similar to the CNi mixture both NiTi and $Ti_2Ni(O)$ were present at 1200 °C in the RA mixture. A fact that is not surprising given what has been learned of the $Ti_2Ni(O)$ phase.

A more thorough analysis of the phase progression in the CNi mixture and the RA mixture is possible using the quantitative results achieved through Rietveld refinement,

141

presented in Figure 4-43. An unknown quantity of liquid is formed during TE-SHS in both mixtures and some may persist up to peak temperature. For this reason the phase fraction values given for the two mixtures beyond TE-SHS are assumed to be qualitative and may overestimate the actual phase fraction.

In both the CNi mixture and the RA mixture the phase fraction of α-Ti remains relatively constant until approximately 700 °C for the CNi mixture and 650 °C for the RA mixture. At which point a slow decrease in phase fraction is observed. Above 765 °C for the RA mixture and 780 °C for the CNi mixture the phase fraction drops rapidly to zero. The decrease is more rapid in the RA mixture than in the CNi mixture with the RA mixture showing α-Ti disappearing at 800 °C, some 60 °C sooner than in the CNi mixture. As expected, the disappearance of α-Ti coincides with the appearance of β-Ti. The β-Ti phase fraction in the RA mixture peaks at 840 °C. This is followed by a relatively rapid decrease. Just beyond 940 °C the remaining β-Ti disappears with the intensity falling to zero very rapidly. The trend is similar in the CNi mixture but with a broader peak that reaches a maximum at approximately 900 °C. Again just beyond 940 °C the β-Ti diffraction peak rapidly disappears.

In the CNi mixture $Ti_2Ni(O)$ starts to form at $\sim$ 800 °C. It steadily increases in phase fraction, peaking at $\sim$ 945 °C, beyond which it slowly decays, levelling off at a non-zero value. In the RA mixture $Ti_2Ni(O)$ begins to form at approximately 650 °C. The phase fraction increases until it reaches a small plateau between $\sim$ 760 °C to 820 °C. Beyond $\sim$ 820 °C the phase fraction increases again until at $\sim$945 °C it suddenly shoots up then decays to a non-zero level.
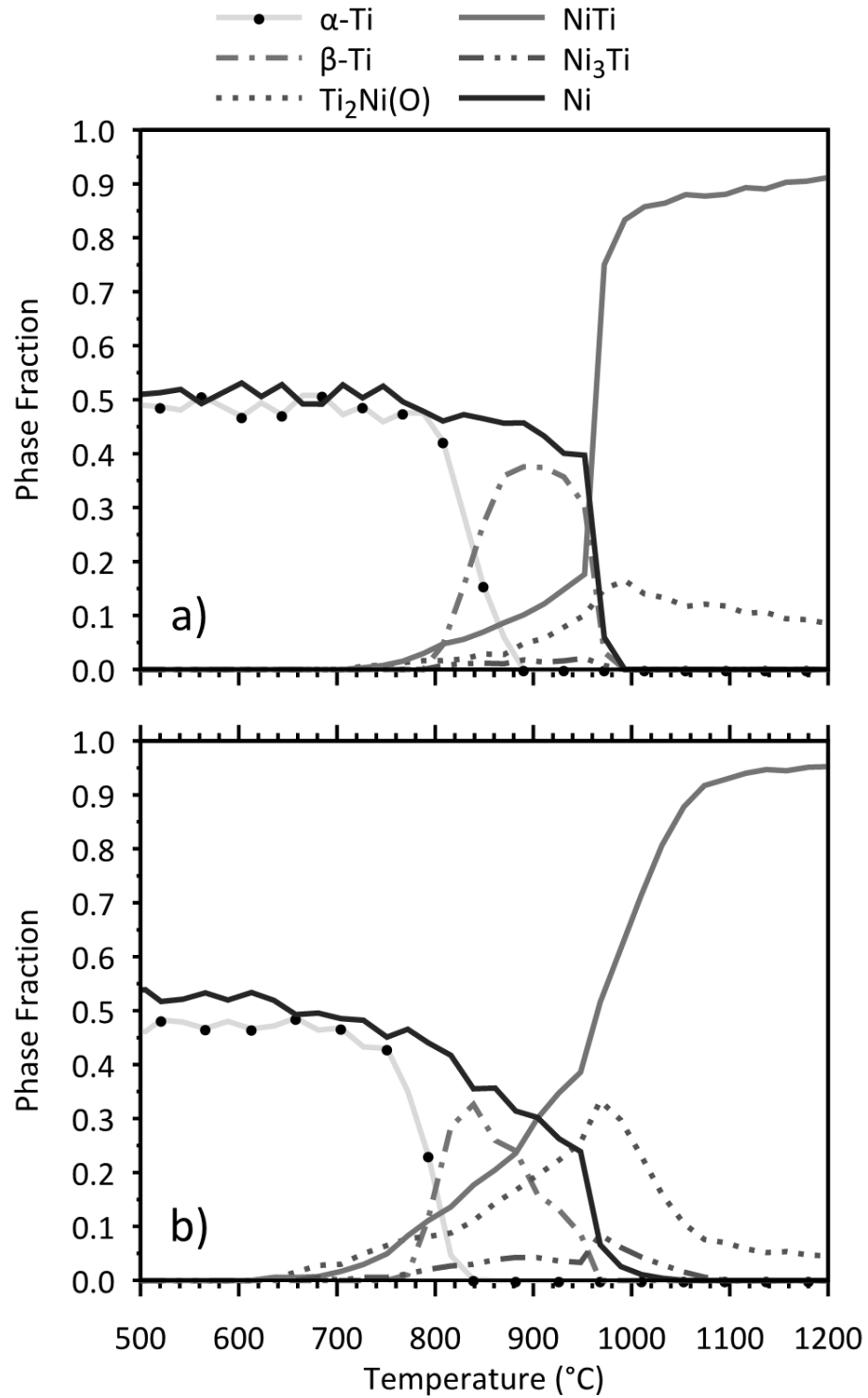
Figure 4-43   **Phase progression in (a) *CNi mixture* and (b) *RA mixture* based on Rietveld refinements**

In the RA mixture NiTi first appear at ~ 700 °C, approximately 50 °C before it was first observed in the CNi mixture. After the initial appearance of NiTi, the phase fraction in both mixtures increases steadily, increasing faster in the RA mixture than in the CNi mixture. At ~ 945 °C the peak intensity in the two blends increases rapidly, peaking at ~ 1080 °C in the RA mixture, and peaking at 1020°C in the CNi mixture.

Ni_3Ti is first visible around 650 °C in the RA mixture with the phase fraction slowly increasing with temperature until from 945°C to ~ 975 °C Ni_3Ti increases rapidly in phase fraction. Finally it decays to 0 by ~ 1050 °C. Ni_3Ti does not show up in the CNi mixture until about 800 °C at which point the Ni_3Ti content increases until a plateau is reached at 900 °C. The rapid increase in Ni_3Ti that occurs from 945-975° in the RA mixture does not occur in the CNi mixture - Ni_3Ti diffraction simply disappears during TE-SHS.

In both the RA mixture and the CNi mixture the Ni phase fractions remains near constant until around 700 °C (a little earlier in the RA mixture and a little later in the CNi mixture). At this point both specimens show an increase in the rate at which Ni is removed from the microstructure with a faster loss of Ni in the RA mixture compared to the CNi mixture. This continues until above 940 °C, at which point Ni disappears rapidly in both mixtures.

Comparing Figure 4-43 (a) and (b) what becomes apparent is that the faster removal of the elemental Ti and Ni phases in the RA mixture than in the CNi mixture is due to faster intermetallic phase formation in the RA mixture. The RA mixture undergoes an earlier and more rapid transformation to β-Ti than the CNi mixture. This observation is

consistent with the DSC traces presented earlier. By the time TE-SHS initiates, much of the β-Ti has formed and decayed in the RA mixture whereas the β-Ti in the CNi mixture is only starting to be consumed. Again this is consistent with the DSC traces and the notion that the amount of β-Ti present prior to TE-SHS is correlated to the TE-SHS enthalpy. The complete disappearance of elemental α- and β-Ti means that all of the Ti is incorporated in the intermetallic phases or is in a liquid state. The decrease in the amount of Ni phase starting at ~ 700 °C is due to the formation of intermetallic phases that consume the elemental Ni. TE-SHS fully eliminates elemental Ni in both powder blends. As with Ti all this indicates is the absence of a crystalline Ni phase.

It is also possible to link the points of interest in the traces for the intermetallic phases to events in the elemental phases. Indeed, the plateau at 770 °C for $Ti_2Ni(O)$ in the RA mixture corresponds with the eutectoid temperature, indicating that the formation of $Ti_2Ni(O)$ slows as the adjacent Ti phase (now β-Ti) starts accepting significantly more Ni into solid solution. The end of this plateau occurs at approximately the temperature at which the β-Ti phase fraction peaks in the RA mixture (~ 820 °C). Meanwhile the NiTi phase grows steadily until TE-SHS. At this point all three intermetallic phases see a significant increase in volume fraction as they rapidly consume the elemental phases. Both Ni_3Ti and $Ti_2Ni(O)$ volume fractions peak shortly after TE-SHS and the NiTi phase continues to grow. The $Ti_2Ni(O)$ peak does not disappear completely even at the highest temperature of 1200°C.

The behaviour in the CNi mixture is different than in the RA mixture. The three intermetallic phases only start to appear once β-Ti starts to form. While the fractions of

NiTi and $Ti_2Ni(O)$ steadily increase, the fraction of Ni_3Ti seems to plateau at ~ 860 °C where it remains until TE-SHS. At TE-SHS elemental Ti, elemental Ni and Ni_3Ti all disappear and the $Ti_2Ni(O)$ phase shows only a marginal increase in volume fraction. The temperature spike inside the crucible as recorded by the sample thermocouple was 145 °C above the furnace temperature, or 1095 °C. While this is below the $NiTi$-Ni_3Ti reverse-eutectic (1115 °C) temperature the actual sample temperature could be much higher. It is likely that the Ni_3Ti melted and formed $NiTi$. Despite the final appearance of the specimen it did not fully liquefy since the $NiTi$ remained crystalline throughout the whole run. As in the RA mixture the presence of the $Ti_2Ni(O)$ in the CNi mixture up to 1200°C is due to a stabilizing effect of O on the phase.

4.6 HIGH TEMPERATURE LATTICE PARAMETERS IN THE NI-TI SYSTEM THROUGH IN-SITU NEUTRON DIFFRACTION AND RIETVELD REFINEMENT

Lattice parameters were obtained from the Rietveld refinements on the in-situ neutron diffraction data over a wide range of temperatures. Rietveld refinements were performed according to the procedure outlined in 4.4.3. Prior to performing Rietveld refinements on the Ni-Ti samples, a refinement was performed on a corundum standard. This was used to determine the zero of the diffractometer and to verify the wavelength. The refined lattice parameter values for the corundum are $a = 4.7605(3)$ Å and $c = 12.9941(8)$ Å compared to the values of $a = 4.760243$ Å and $c = 12.996$ Å provided with the standard. This shows a difference of 0.0003 Å in a and 0.002 Å in c. The numbers in the parentheses of the refined lattice parameters are the standard uncertainties (s.u.). The s.u. is a measure of refinement precision, more specifically it is a measure of how well the model fits the

experimental data but not how accurate the model is [87]. Lattice parameter s.u.s have been observed to be much smaller than the probable error in parameter values determined by replication studies [87]. This is the case above where the error in the refined c parameter is more than twice the s.u. value (0.002 vs 0.0008). In a Rietveld refinement round robin, where powder samples were sent out to various labs for measurement and analysis, the reported lattice parameter values showed a spread of 0.023 Å [93].

Problems in obtaining accurate lattice parameters through Rietveld refinement of constant wavelength neutron data include determining the zero offset of the diffractometer and an accurate value of the wavelength [87,93,128]. While this was performed using the corundum standard, in practice the accuracy of these two parameters is affected by their serial correlation in the model allowing one parameter to correct for errors in the other [128]. The wavelength (determined using the standard) is kept constant during refinement of sample data, however opinions vary on the refinement of the zero parameter. Peplinski *et al* [128] believe it good practice to not release the zero whereas Hill and Cranswick [93] improved the accuracy of some of the lattice parameters in the Rietveld round robin by refining the zero.

The current experimental conditions also impact the accuracy of refined lattice parameters determined by refinement of the in-situ ND patterns. These include the 2θ collection range (ideally it would extend to higher angles), data collection during a ramp and the starting powders. The values obtained for the lattice parameters reflect the value for the average temperature over the temperature range of the acquired pattern (or composite patterns).The powders under investigation are not the typical high purity

starting materials used in lattice parameter studies. Despite the issues raised above the lattice parameters obtained from the ND experiments are valuable. Few studies are available that have determined high temperature lattice parameters for the elemental Ti (both α-Ti and β-Ti) and Ni phases [129], and these can be difficult to source. More importantly, to the author's knowledge lattice parameters for β-Ti(Ni) and the three intermetallic phases at temperatures significantly higher than ambient is non-existent in the literature. The errors presented for the lattice parameters obtained by Rietveld refinement are the s.u.s (due to availability). The error is in parenthesis following the lattice parameter and refers to the error in the last significant digit. Lattice parameter data for the phases present in the Ni-Ti system were determined from the following ND runs:

- *El Ni/El Ti*: for α-Ti (*a* and *c*), β-Ti (*a*) and Ni (*a*).
- *95Ti/5Ni*: for α-Ti (*a* and *c*) and β-Ti(Ni) (*a*)
- *Ti2Ni/Ni3Ti*: for Ti$_2$Ni (*a*) and Ni$_3$Ti (*a* and *c*)
- *LP mixture* (*RS1200* sintering profile): for NiTi (*a*)
- *HP mixture* (*RS1200* sintering profile): used for NiTi (*a*)

The lattice parameter data from the above refined in-situ ND runs used to produce the graphs in this section is in Appendix A.

4.6.1 *Elemental powders*

Ambient lattice parameters for α-Ti are presented in Table 4-6. The wt% oxygen is provided as the *c* parameter in α-Ti is particularly sensitive to interstitial contaminants [130]. The Ti powder used for the *El Ni/El Ti* and *95Ti/5Ni* runs was the same and there is generally good agreement between the two sets of lattice parameters

showing variations of 0.0035 Å in *a* and 0.002 Å in *c*. The largest variation comes from comparing the lattice parameters from the *El Ni/El Ti* with the values obtained by Clark [130] for high purity α-Ti (0.007 Å in *a* and 0.01 Å in *c*). Clark used x-ray diffraction on polycrystalline Ti sheet to reduce surface contamination compared to powders. The larger discrepancy in the *c* parameter is to be expected due to a difference in O concentration between the two α-Ti specimens. When the lattice parameters are compared to values for α-Ti with approximately the same wt% O the difference in the *c* lattice parameter drops to 0.006 Å while the difference in *a* is unchanged. The higher accuracy from the *95Ti/5Ni* refinement is likely due in small part to an experimental temperature closer to that of Clark's and in large part due to the larger amount of Ti present in the sample. Despite a near equal amount of Ti : Ni used in the *El Ni/El Ti,* Ni is a much stronger neutron scatterer and the resulting diffraction pattern is dominated by Ni peaks. During refinement of the zero parameter the misfit in the Ni peaks carried more weight than those in the Ti. To investigate this, Ni was removed from the model and the 32 °C diffraction pattern was refined to fit only the α-Ti peaks. This resulted in lattice parameter values of 2.954(1) Å and 4.688(2) Å for *a* and *c* respectively. These values are closer to those determined by Clark for a similar amount of oxygen (Δa = 0.003 Å and an effective Δc = 0 Å). Finally while the content of H and N in the powders are low (.025 wt% and .012 wt% respectively) it may also be a factor in the differences in refined lattice parameters vs. the data presented by Clark [130].

Table 4-6   **Ambient temperature α-Ti lattice parameters determined by Rietveld refinement of ND patterns vs. literature values** [130]

Temperature (°C)	Lattice parameter (Å)			wt% O	ND run/ref
	a	*c*	*c/a*		
32	2.9576(5)	4.693(1)	1.587	0.27	*El Ni/El Ti*
26	2.9541(3)	4.6906(6)	1.5878	0.27	*95Ti/5Ni*
25	2.9504(3)	4.6833(3)	1.5873	0	Clark
25	2.9506	4.6875	1.589	0.3	Clark*

* Lattice parameter values read off of Figure 1

High temperature lattice parameters for both α-Ti and β-Ti are presented in Figure 4-44. In the case of *95Ti/5Ni* the α-Ti lattice parameters are limited to 760 °C due to the reverse eutectoid reaction at 765 °C. In α-Ti, nickel is only soluble to .3wt% (0.24 at%) at 765 °C, whereas at the same temperature β-Ti hold 5-6 wt% Ni [7]. In the former the low Ni content does not have a significant effect on the lattice parameters while in β-Ti the high concentration of Ni has a significant impact on the lattice parameter. For this reason it is discussed separately in the following section. Spreadborough and Christian [131] performed high temperature XRD on both Ti powders and Ti solid samples. They noted surface contamination problems with the powders and so only the data from the solid samples are presented here. The data from Senkov *et al* [132] is based on a model described in their paper as experimental data was presented in the form of figures only.

150
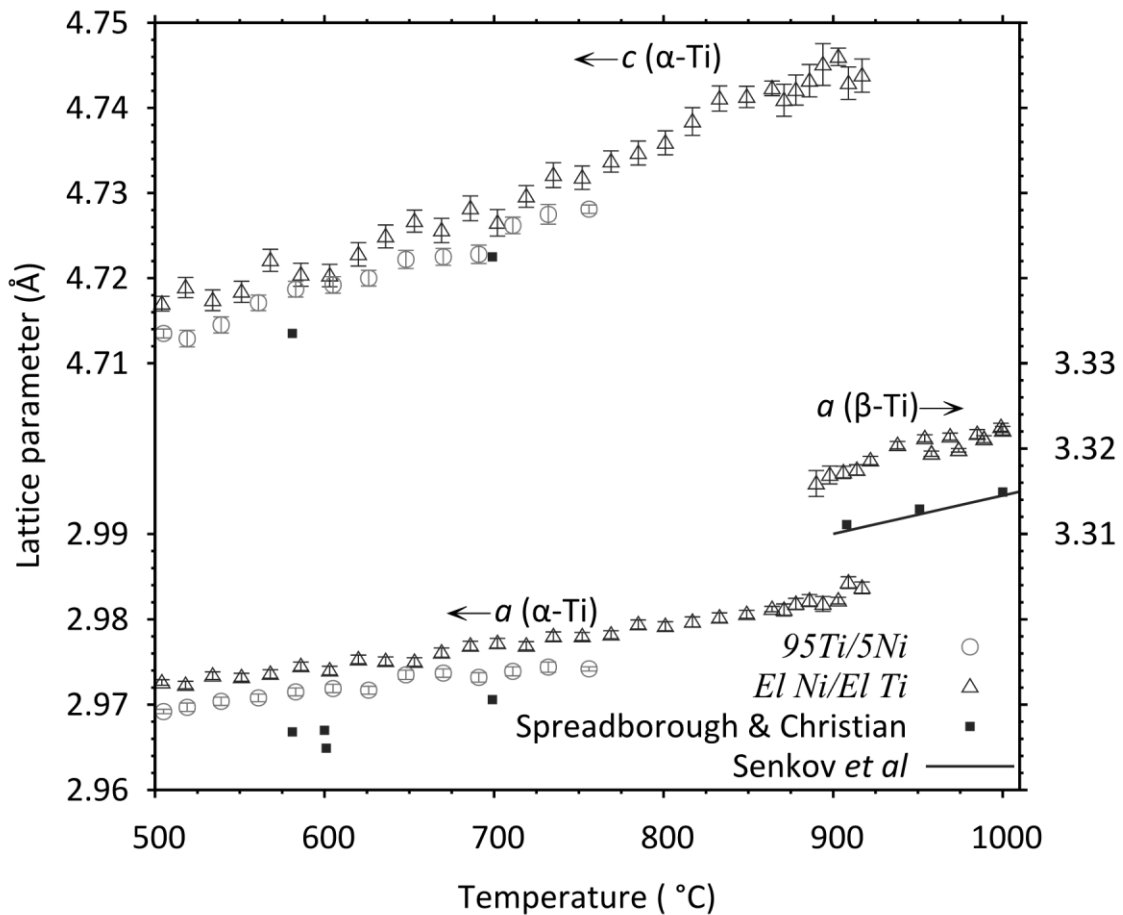
Figure 4-44 **Lattice parameters of elemental Ti for both α-Ti (top and bottom left) and β-Ti (middle right) from Rietveld refinement of ND runs and literature values** [131,132]. **Values from Senkov *et al.* are based on a model presented in** [132].

As is the case for the ambient lattice parameters the values of *a* and *c* from the 95Ti/5Ni run are lower than those from the *El Ni/El Ti* run. In both cases the lattice parameters determined through Rietvled refinement are higher than the values given in literature. The reasons listed for the difference in the ambient temperature data also applies for the high temperature data. Spreadborough and Christian give coefficients of expansion for α-Ti over a range of 0 to 600 °C as $9.55e10^{-6} \pm 0.5e10^{-6}$/ °C for *a* and $10.65e10^{-6} \pm 0.7e10^{-6}$/ °C for *c*. Coefficients of expansion over the same range for *95Ti/5Ni* are $10.4e10^{-6}$/ °C for

151

a and 10.5e10^{-6}/ °C for *c* and for *El Ni/El Ti* are 9.7e10^{-6}/ °C for *a* and 10.2e10^{-6}/ °C for *c*. Other than a larger coefficient of expansion for *a* determined for *95Ti/5Ni* these values fall within the range of error expressed by Spreadborough and Christian. This would indicate that the causes of the difference in lattice parameters is not dependent on temperature.

Lattice parameter values for α-Ti are presented at temperatures up to 925 °C. Oxygen is a well-known α-Ti stabilizer [133]. Even the relatively small amount of oxygen present in the Ti powders (0.27 wt% O) allows α-Ti to remain stable up to 950 °C [133].

β-Ti lattice parameters are reported on the middle right side of Figure 4-44. The values obtained from *El Ni/El Ti* are larger than those reported by Spreadborough and Christian [131] and Senkov *et al* [132] by approximately 0.007 Å. The coefficient of expansion from 900 to 1000 °C determined from *El Ni/El Ti* for *a* is 12.8e10^{-6}/ °C and the extrapolated room temperature lattice parameter for β-Ti is 3.279 Å. These values compare reasonably well with a coefficient of expansion of 12e10^{-6}/ °C (for 900 to 1070 °C) and an extrapolated room temperature lattice parameter of 3.279 as published by Spreadborugh and Christian.

Ni lattice parameters determined from the refinement of *El Ni/El Ti* are compared to lattice parameter values determined by Kohlhaas *et al* [134] by way of high temperature x-ray diffraction and lattice parameter values calculated from thermal expansion data by Wang *et al* [135] in Figure 4-45. The calculated values by Wang *et al* match those experimentally determined by Kohlhaas quite well up to 800°C. Above 800 °C the experimentally determined lattice parameters are larger than those predicted by the model

152

from Wang *et al*. The expansion of the *El Ni/El Ti* lattice parameters with increasing temperature follow the same general trend as Wang *et al* with a positive offset by approximately 0.006 Å. At temperatures above 800 °C the difference between the *El Ni/El Ti* and Kohlhaas lattice parameters decreases.
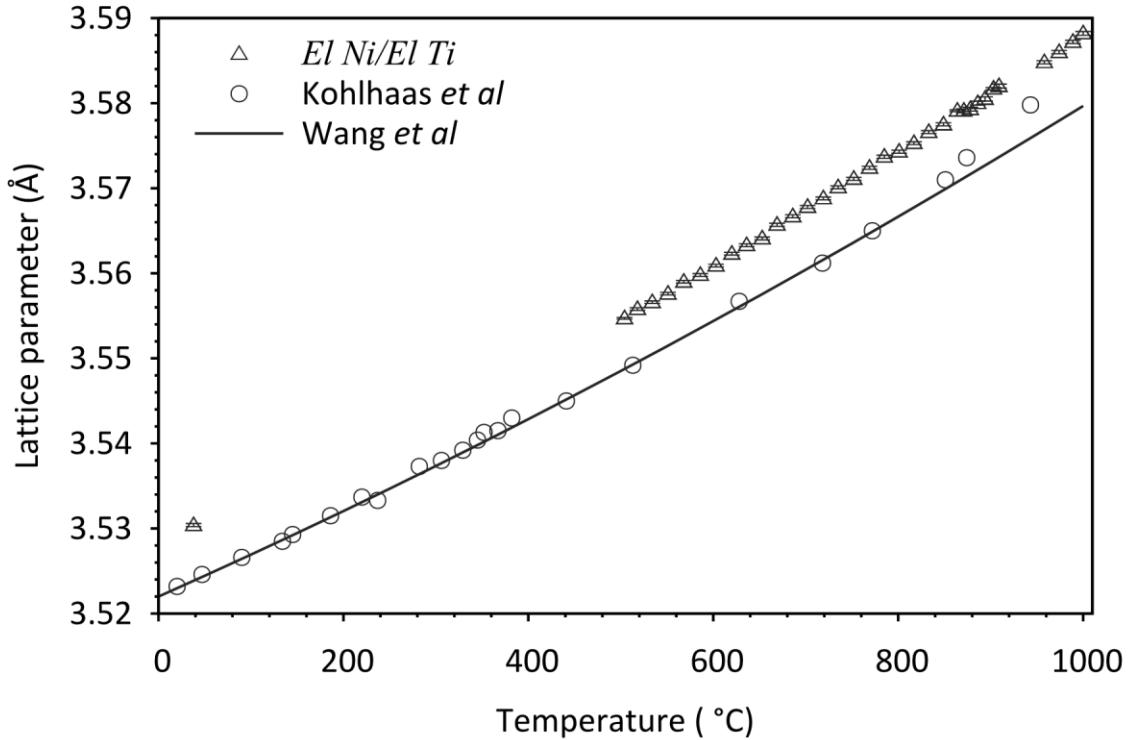
Figure 4-45 **Lattice parameters of elemental Ni from Rietveld refinement on in-situ ND patterns and literature values** [134,135]**. Values from Wang *et al*. are based on a model presented in** [135]**.**

Differences between powder purity is one reason for the difference between the literature values and the *El Ni/El Ti* lattice parameter values (Kohlhass list an impurity level of less than 0.003%). Another reason could be bias due to the Rietveld refinement. The α-Ti peaks were removed from the ambient temperature pattern and Rietveld refinement was performed on the pattern with α-Ti removed from the model. Unlike in the case of the α-

Ti, there was no change in the Ni lattice parameter. This would indicate that the Ni peaks did indeed dominate the refinement of the zero position.

4.6.2 β-Ti(Ni)

Lattice parameters for β-Ti(Ni) mixed to 6.1 wt% Ni (5 at% Ni) are presented in Figure 4-46 alongside the elemental β-Ti values determined from *El Ni/El Ti* as a comparison. The lattice parameters of β-Ti(Ni) are lower than those for elemental β-Ti for the same temperature by 0.03 Å. Ni is a smaller atom and is substitutional in β-Ti resulting in a smaller lattice parameter. It is expected that an increasing Ni content results in a decreasing lattice parameter. The β-Ti(Ni) lattice parameter plot can be split into two sections: above 810 °C and below 810 °C. The lattice parameters for β-Ti(Ni) above 810 °C show a much slower increase in dimension with rise in temperature. The coefficient of expansion for β-Ti(Ni) over the range of temperatures of 900 to 1000 °C is 14.5e-6/ °C. While larger it is reasonably close with the value of 12.8e-6/ °C for elemental β-Ti over the same range. This would suggest that above 810 °C the rate of lattice expansion in β-Ti(Ni) is largely unaffected by the Ni content.
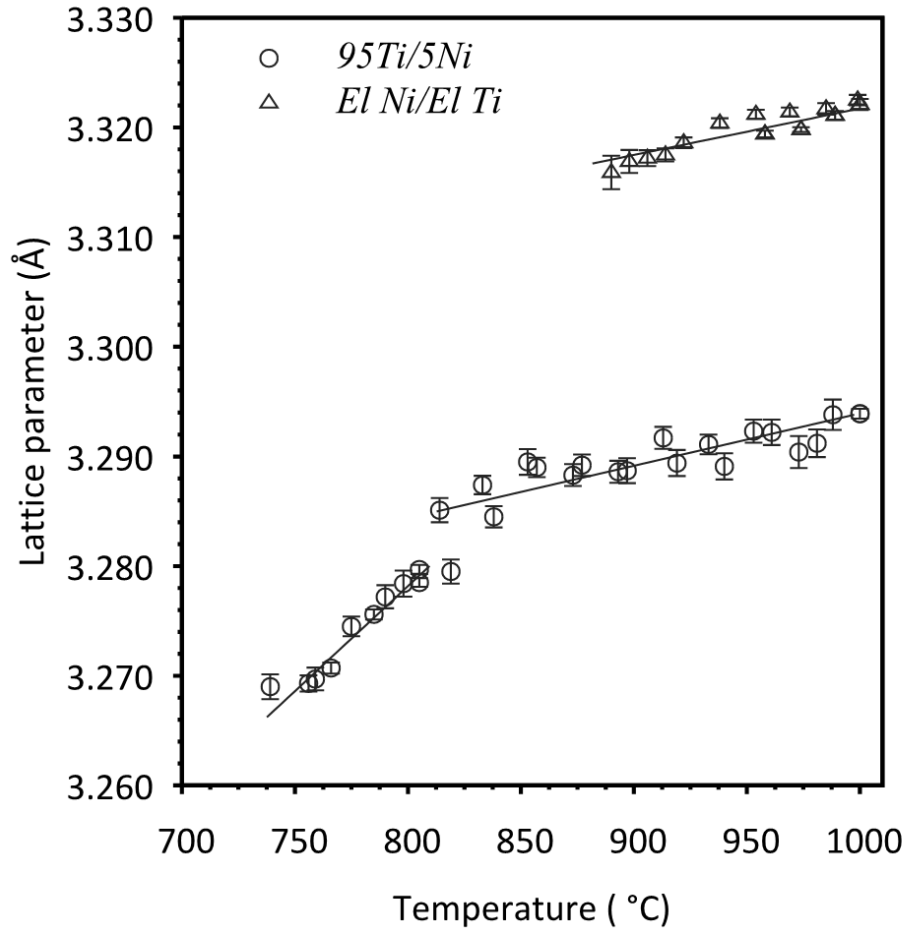
Figure 4-46 **Lattice parameters of β-Ti(Ni) with 6.1 wt% Ni in solid solution (*95Ti/5Ni*) plotted with elemental β-Ti (0.004 wt%) for comparison (*El Ni/El Ti*)**

Below 810 °C the coefficient of expansion is much higher at 58.5e-6/ °C over a temperature range of 765 to 810 °C. The explanation for this is provided by an analysis of Figure 4-47. At 814 °C β-Ti is the only phase present in the microstructure. Starting at 805 °C α-Ti appears in the diffraction patterns. Note that no Ti$_2$Ni is present in the diffraction pattern until 756 °C. The specimen is thus in the two phase α-Ti + β-Ti(Ni) region during cooling from 805 to 756 °C. The two phase region indicates a hypo-eutectoid composition. During cooling the growing α-Ti phase rejects Ni into β-Ti(Ni).

The increasing Ni content with decreasing temperature results in a more rapid decline in the β-Ti(Ni) lattice parameter than is expected due to a drop in temperature alone. The eutectoid decomposition commenced at 756 °C and was completed by 736°C.
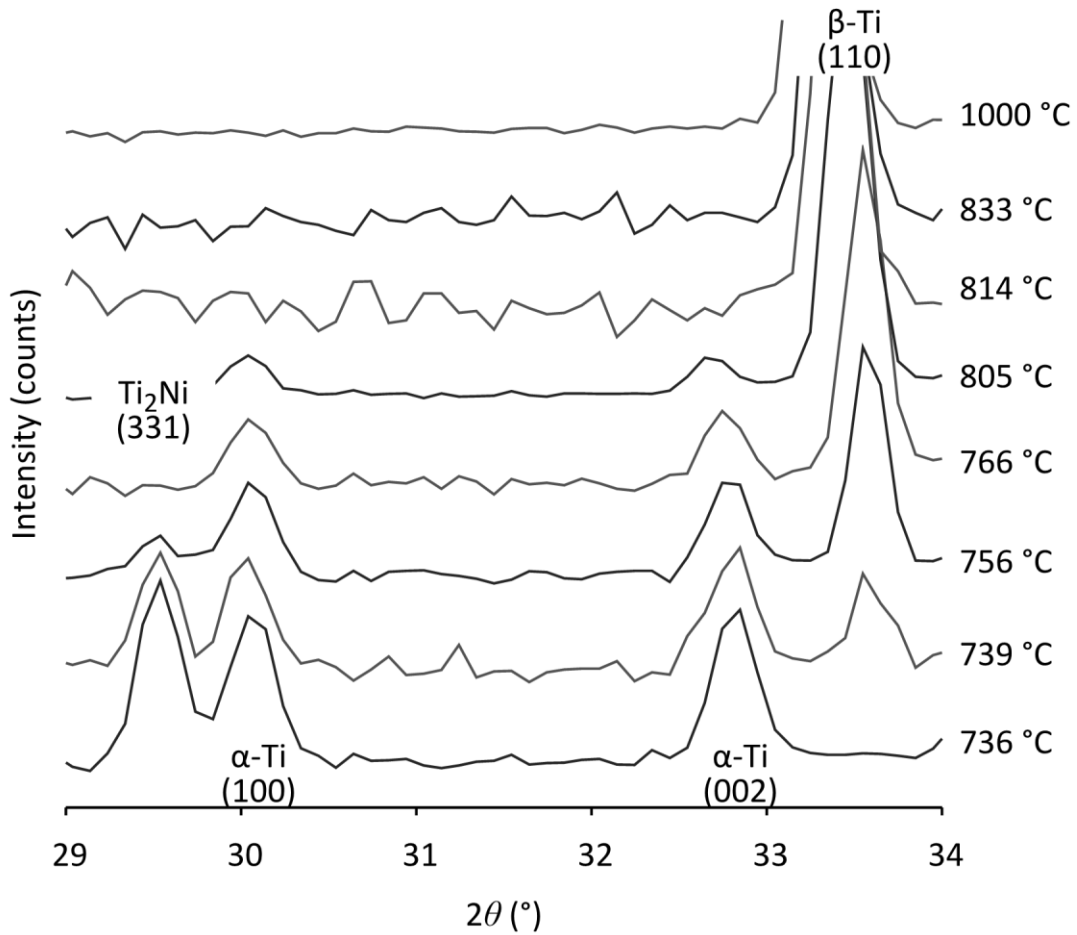
Figure 4-47 **Selected diffraction patterns for β-Ti(Ni) during cooling from 1000 °C to 736 °C showing primary α-Ti at 805 °C followed by the eutectoid (β-Ti → α-Ti + Ti$_2$Ni) starting at 756 °C.**

The composition of the sample was mixed to the eutectoid composition of 6.1 wt% Ni according to [7], as such the two phase α-Ti + β-Ti region is unexpected. Possible explanations include sample composition differing from the desired mixing composition,

small errors in the phase diagram and impurities in the powders. The trace amount of oxygen may create a ternary eutectoid with a higher Ni composition than the composition presented in the binary phase diagram [7]. Further investigation on the mixture is required to understand the true cause of the α-Ti + β-Ti region starting at 805 °C.

4.6.3 *Intermetallic phases*

Lattice parameters for the following three intermetallics are presented below: Ti_2Ni, NiTi (referred to as austenite with a B2 crystal structure) and Ni_3Ti. While the intermediate intermetallics Ni_4Ti_3 and Ni_3Ti_2 can appear depending on thermal history [1], none were observed in this investigation. The low temperature phase of NiTi (referred to as martensite with a B19' crystal structure) appears in the cool down traces of the *HP mixture* and the *LP mixture* but is not presented.

Lattice parameters for Ti_2Ni are presented in Figure 4-48. The 32 °C lattice parameter determined in this study is larger by as much as 0.063 Å than the literature values (Table 4-7). The current results compare most favorably with those presented by Duwez and Taylor [136] with a difference of 0.008 Å. Oxygen contamination is not thought to be a major contributor to the difference. Analysis of the (400), (222) and (311) Ti_2Ni peaks do not indicate significant oxygen present and a refinement of the O occupancy indicates approximately 0.5±0.4 at% O. This value is in line with the reported oxygen content of 1.03 at% by Mueller and Knott [137] who give a lattice parameter of 11.3193(2) Å, a 0.022 Å difference. The oxygen content of the Ti_2Ni in the work by Duwez and Taylor [136] is not known. A linear extrapolation of the 200 to 930 °C lattice parameter data to 25 °C yields a lattice parameter of 11.332 Å, very close to the 11.333 Å given by

Duwez and Taylor [136]. This suggests there is a larger bias in the 32 °C pattern than in would be expected at elevated temperatures.
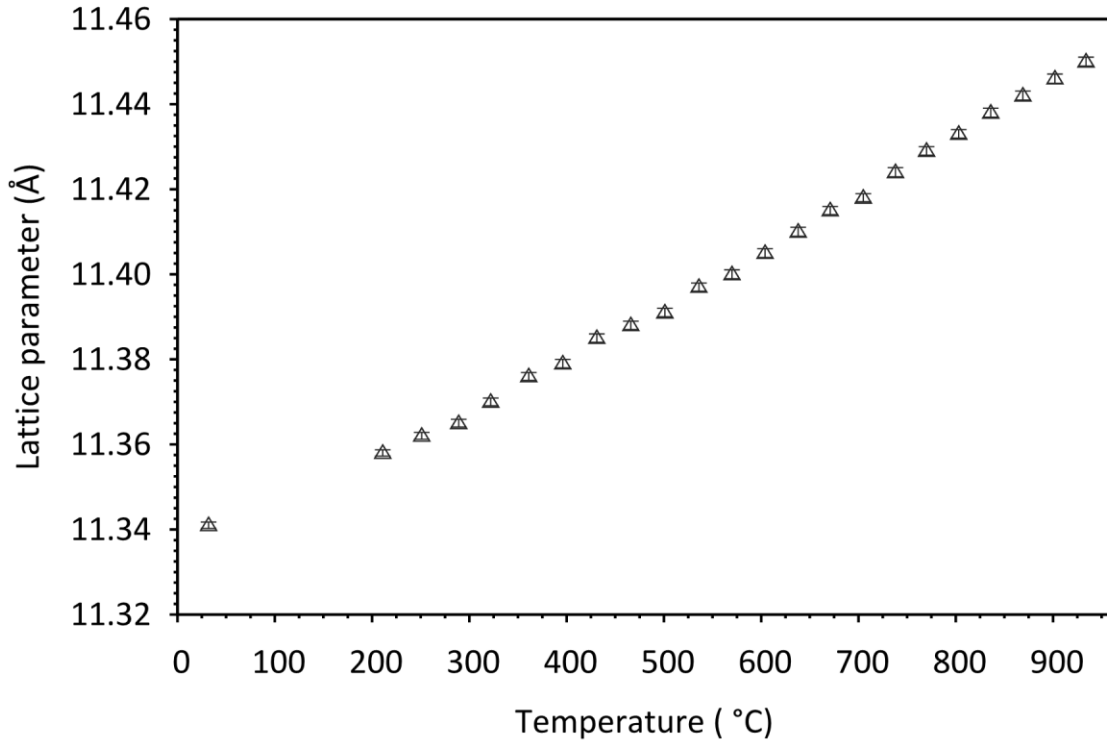
Figure 4-48   Ti₂Ni lattice parameters from the refinement of the *Ti₂Ni/Ni₃Ti* ND experiment

Table 4-7   Ambient temperature Ti₂Ni lattice parameter determined by Rietveld refinement of ND patterns vs. literature values [102,119,136,138]

Temperature (°C)	Lattice parameter (Å)	ND run/ref
32	11.3409(7)	*Ti ₂ Ni/Ni ₃ Ti*
25	11.3193(2)	Mueller
25	11.278	Yurko
25	11.333	Duwez
25	11.29	Rostoker

158

The NiTi lattice parameters for both the *HP mixture* and the *LP mixture* generally show good agreement (Figure 4-49) over the full temperature range. The difference in lattice parameters between the two experiments became larger as the temperature increased (as large as 0.002 Å). The *HP mixture* had higher lattice parameters. At temperatures below 85 °C, the austenite phase transforms to martensite. In the *HP mixture* this transformation is complete by 65 °C while in the *LP mixture* diffraction patterns indicate a two phase austenite – martensite microstructure. There is generally good agreement between the lattice parameters determined in this study with those determined by Khalil Allafi *et al* [139]. They determined lattice parameters by Rietveld refinement on a 55.2 wt% (50.1 at%) Ni : 44.8 wt% Ti NiTi specimen for 64, 74 and 84 °C. The difference between the lattice parameters from the two studies is less than 0.003 Å.
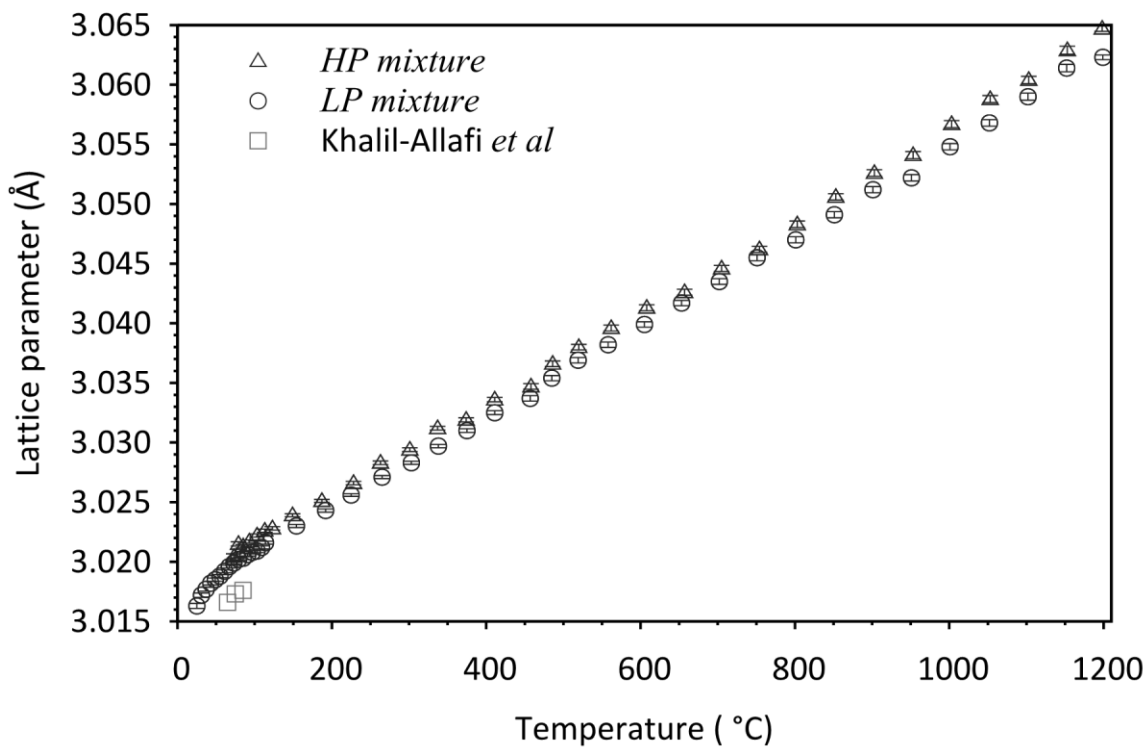
Figure 4-49 **NiTi (B2) lattice parameters from the refinement of the *HP mixture* and the *LP mixture* cool down neutron diffraction patterns**

The *a* and *c* lattice parameters as well as the *c/a* ratio of the HCP Ni_3Ti phase are plotted in Figure 4-50. The value of the *a* lattice parameter went from 5.1143(3) Å at room temperature expanding to 5.1690(4) Å at 930 °C. Over the same temperature interval the *c* axis expanded from 8.3378(8) Å to 8.445(1) Å. The *c/a* showed little change over the temperature range, increasing to 1.634 from 1.630. This is consistent with HCP structures that have a *c/a* ratio of 1.63 [129].

160
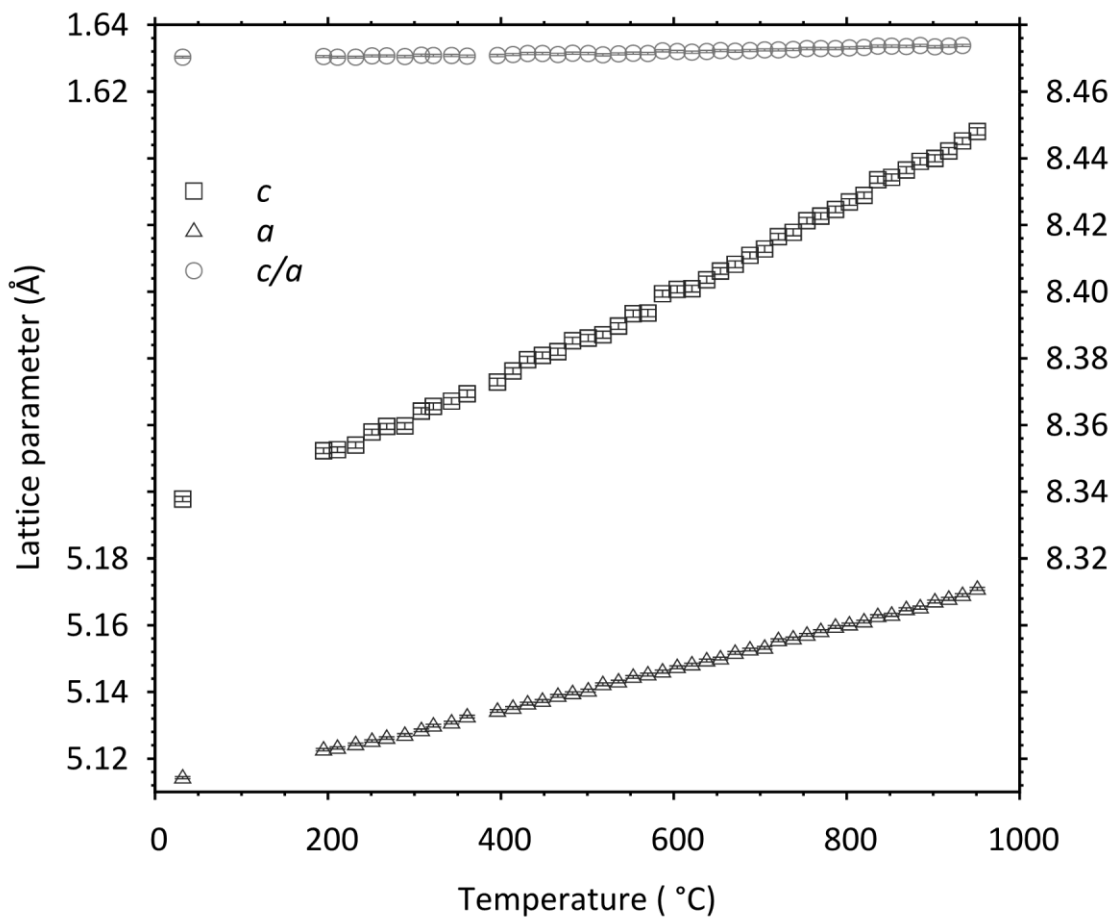
Figure 4-50   Ni₃Ti lattice parameters from the refinement of the *Ti₂Ni/Ni₃Ti* ND experiment

The 32 °C lattice parameter results for Ni₃Ti, while higher, generally agree with the data found in the literature for room temperature data (Table 4-8). The largest difference in the *a* parameter is in comparison to Glimois *et al* [140] at 0.013 Å, whereas the largest difference in the *c* parameter is in comparison to Duwez and Taylor [136] at 0.0158 Å.

Table 4-8 **Ambient temperature Ni₃Ti lattice parameter determined by Rietveld refinement of ND patterns vs. literature values** [136,140,141]

Temperature (°C)	Lattice parameter (Å)			ND run/PDF
	a	*c*	*c/a*	
32	5.1143(3)	8.3378(8)	1.6303	*Ti₂Ni/Ni₃Ti*
25	5.1088(5)	8.3187(7)	1.6283	Poole
25	5.103	8.293	1.6250	Duwez
25	5.101(2)	8.322(2)	1.631	Glimois

CHAPTER 5
SUMMARY AND CONCLUSIONS

The four different powder mixtures were specifically chosen to investigate different aspects of the sintering of NiTi from elemental powders. The LP mixture and the HP mixture were physically indistinguishable leaving the Ti powder purity level a major factor in the different sintering behaviours. The HP mixture and the RA mixture offered similar Ti purity levels but differed in size by a factor of 3. This resulted in an increase in the volume to surface area of the Ti particle in the mixture. In contrast the CNi mixture had a significantly larger Ni volume to surface area than the other powder mixtures.

While the interpretation of DSC traces led to a deeper understanding of the sintering behaviour of elemental Ti and Ni powders, neutron diffraction was required for a full understanding of the phase progression. Differential thermal ('DT') traces produced using the T_{SAMPLE} and $T_{CONTROL}$ thermocouples were compared to DSC traces to verify the temperature accuracy of the ND data. For neutron diffraction experiments performed in either Mo or V crucibles temperature accuracy was found to be very good.

Rietveld refinement of neutron diffraction patterns obtained *in-situ* during the reactive sintering of Ni-Ti (49 at% Ni : 51 at% Ti) elemental powder compacts was performed for the LP mixture (both RS1000 and RS1200 sintering profiles), HP mixture (RS1200 only), RA mixture (RS1200 only) and the CNi mixture (RS1200 only). The atomic displacement parameter (U_{iso}) and the lattice parameters for each phase that occurs during reactive sintering (α-Ti , β-Ti(Ni), $Ti_2Ni(O)$, NiTi, Ni_3Ti and Ni) were obtained from separate *in-situ* experiments on stoichiometric powder mixtures. The determination of

accurate U_{iso} values from separate experiments was found to be particularly important for the successful refinement of minority phases. Diffraction peaks from minority phases often suffered from peak overlap in the NiTi mixture, leading to poorly refined lattice parameters. Prior knowledge of the lattice parameters for each phase ensured that these errors could be identified and corrected. The reproducibility of the analysis was excellent, as demonstrated by the consistency of results obtained for the two different sintering profiles. The uncertainty in the weight percent of each intermetallic phase was determined to be 0.016 wt%.

In general intermetallic phase formation did not begin until the oxide layer surrounding Ti particles dissolved at 600 °C. During the early stages of sintering, $Ti_2Ni(O)$ was the fastest growing intermetallic phase. Eventually NiTi became the dominant phase and it continued to grow at the expense of all the other phases. The final microstructure consisted of a combination of NiTi and $Ti_2Ni(O)$. While Ti_2Ni has a melting temperature of 984 °C, the present neutron diffraction results indicate that interstitial O raises the melting point of the $Ti_2Ni(O)$ phase up to at least 1200 °C (the highest temperature investigated).

Beyond the general trend, each powder mixture has a unique phase progression (Figure 5-1) due to the differences in the starting powder mixtures. The LP mixture shows the most rapid intermetallic formation followed by the HP mixture, the RA mixture and then the CNi mixture.
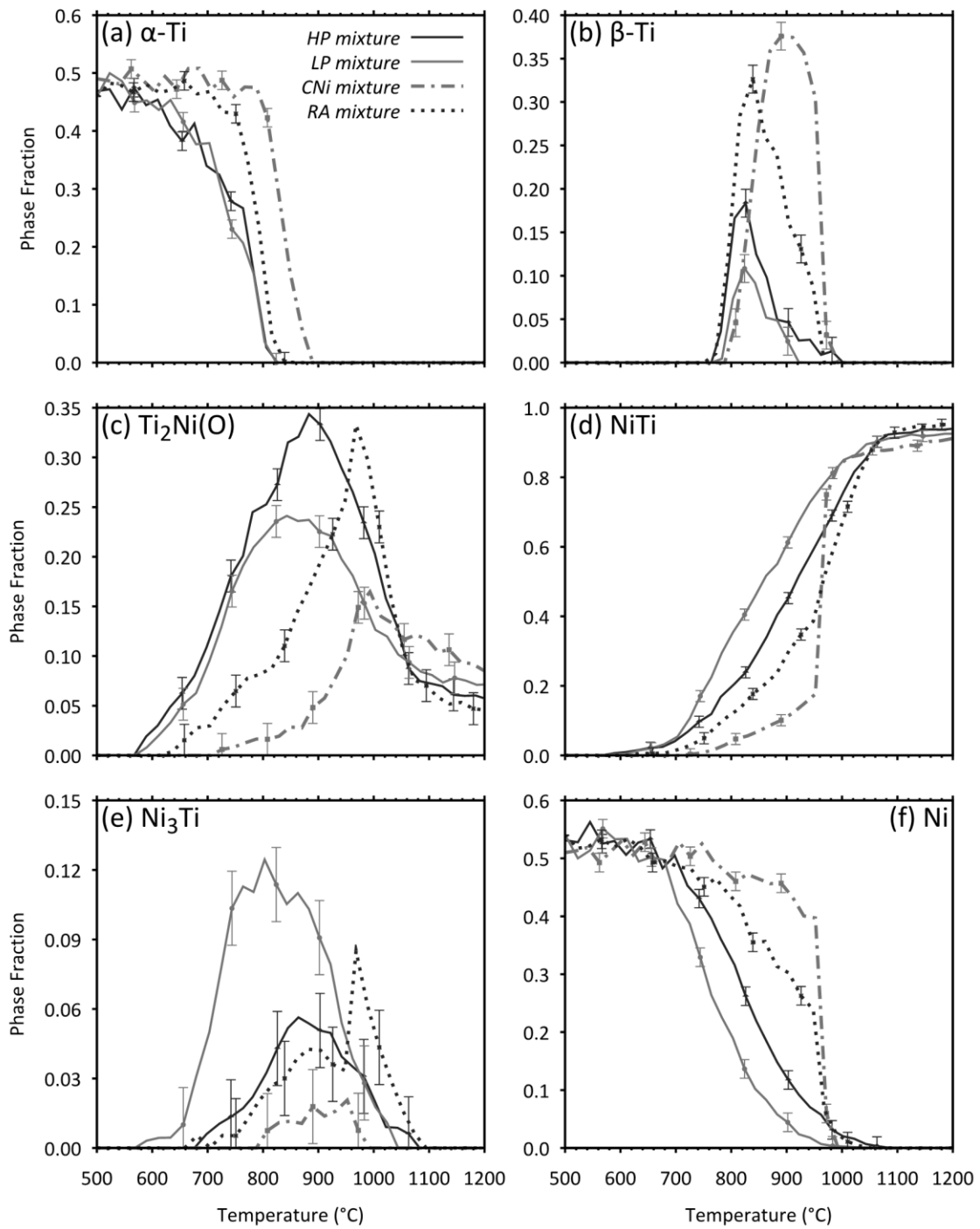
Figure 5-1 **Phase progression by phase for all powder mixtures determined by Rietveld analysis on in-situ neutron diffraction patterns (RS1200 sintering profile)**

Comparing the phase progression of the LP mixture and the HP mixture it is clear that elemental Ti powder purity plays an important role in the sintering of NiTi from the beginning stages of sintering right through to the final product. While it is not understood it is thought that the higher levels of impurities in the LP Ti powder alters the diffusion rate and/or pathways leading to a faster rate of reaction in the LP mixture compared to the HP mixture. In the two mixtures α-Ti and β-Ti are removed at similar rates with the LP mixture removing Ti (in both α and β-Ti) marginally faster than in the HP mixture. Elemental Ni is removed noticeably quicker in the LP mixture leading to a quicker formation of the Ni rich intermetallics (NiTi and Ni_3Ti) in the LP mixture while the HP mixture has a larger phase fraction of the Ti rich intermetallic $Ti_2Ni(O)$ during the early stages of sintering. As a consequence of the faster rate of reaction a much finer scale porosity is evident in the LP mixture than in the HP mixture (see Figure 4-14).

The faster rate of reaction in the HP mixture compared to the RA mixture is explained by the larger Ti powder size in the RA mixture. The larger surface area to volume ratio in the HP mixture provided more interfacial area, more access to elemental Ti and shorter diffusion distances allowing for faster intermetallic formation. An exception to this is Ni_3Ti which forms almost as quick in the RA mixture as in the HP mixture. In general the difference between the rate of intermetallic formation between the LP mixture and the HP mixture is similar to the difference between the HP mixture and the RA mixture. While the underlying mechanisms are not understood it can be concluded that the small change in Ti powder purity affects the rate of intermetallic formation by the same order of magnitude as tripling the Ti powder size.

166

The CNi mixture had the slowest phase progression of all the powders. Ni is known to be the faster diffusing element in the Ni-Ti system. In the RA mixture Ni could diffuse rapidly in the inter-particle diffusion pathways to access to the Ti particle. Once at the surface of the Ti, nickel was able to diffuse into the powder core forming intermetallics. In the CNi mixture Ni was deprived of the inter-particle diffusion paths present in the other mixtures making diffusion from the Ni core to the Ti much slower. At the same time the Ti at the Ni particle surface diffused very slowly into the Ni core creating very little intermetallic phases during sintering up until TE-SHS.

The coarse powder in the RA mixture and the CNi mixture slowed diffusion to the point that TE-SHS was visible with a heating rate of 2°C/min. For the first time in-situ neutron diffraction was used to study the phase progression of TE-SHS. The different phase progression in the two mixtures resulted in a larger TE-SHS peak and specimens that slumped in the CNi mixture. During TE-SHS elemental Ti and Ni disappeared, with a corresponding surge in the fractions of the intermetallic phases. In the RA mixture all three intermetallic phases were present at the end of the reaction, while in the CNi mixture the Ni_3Ti phase disappeared during TE-SHS.

These results support the relationship between β-Ti and TE-SHS put forward by Whitney *et al.* [32,33] and what is seen in the DSC results. The LP mixture and the HP mixture show a weight fraction of β-Ti of 0 or within experimental error of zero at 942 °C and correspondingly show no indications of TE-SHS. The RA mixture had ~10 wt% β-Ti at the measured TE-SHS temperature of 942 °C while the CNi mixture, with a much larger measured TE-SHS still had ~30 wt% β-Ti at 955 °C (its recorded TE-SHS onset).

Unfortunately in the in-situ neutron diffraction work by Chen *et al* [60–62] they were unable to distinguish β-Ti in their diffraction patterns, which clearly plays an important role in the sintering behaviour of NiTi.

Refinement of the oxygen concentration in Ti$_2$Ni(O) during sintering, expressed as the occupancy of the oxygen interstitial sites, was performed for the first time. It has led to a better understanding of why Ti$_2$Ni(O) is always found after sintering from elemental powders. During the initial stages of sintering, Ti$_2$Ni(O) with little or no O is formed. As the amount of this phase increases, its O content also increases, likely as a result of accepting O from the elemental Ti that it consumes as it grows. A significant increase in O concentration occurs when the phase fraction of Ti$_2$Ni(O) starts to decrease, since, as NiTi consumes Ti$_2$Ni(O), the O remains in Ti$_2$Ni(O). The O raises the melting point of Ti$_2$Ni(O), making it extremely difficult to remove. It is thought that the best way to eliminate the Ti$_2$Ni phase is to use low O content powders of both Ni and Ti.

In situ neutron diffraction has allowed for the determination of the lattice parameters of the phases present in the Ni-Ti system through Rietveld refinement. The results generally showed good agreement (max 0.01 Å) with published values when available. The 765 °C β-Ti(Ni) → α-Ti + Ti$_2$Ni eutectoid reaction was shown in-situ for the first time. The 6.1 wt% Ni lowered the lattice parameter of elemental β-Ti by 0.03 Å for the equivalent temperature. During cool down a two phase mixture of β-Ti(Ni) + α-Ti formed whereupon the expansion coefficient of β-Ti(Ni) became much steeper. This was attributed to solute rejection by α-Ti increasing the Ni content in β-Ti(Ni). The lattice parameters for Ti$_2$Ni and Ni$_3$Ti were determined up to a temperature of 940 °C and the

lattice parameters of NiTi were determined up to 1200 °C. To the author's knowledge this is the first time the lattice parameters for these intermetallic phases has been determined to temperatures above a 200 °C.

REFERENCES

[1]   K. Otsuka and X. Ren, Prog. Mater. Sci. **50**, 511 (2005).

[2]   L. Zhang, Y. Q. Zhang, Y. H. Jiang, and R. Zhou, J. Alloys Compd. **644**, 513 (2015).

[3]   T. Krenke, S. Aksoy, E. Duman, M. Acet, X. Moya, L. Mañosa, and A. Planes, J. Appl. Phys. **108**, 043914 (2010).

[4]   K. Bhattacharya, S. Conti, G. Zanzotto, and J. Zimmer, Nature **428**, 55 (2004).

[5]   D. Porter and K. Easterling, *Phase Transformations in Metals and Alloys, Second Edition*, 2nd ed. (CRC Press, UK, 1992).

[6]   W. Tang, Metall. Mater. Trans. A **28A**, 537 (1997).

[7]   J. L. Murray, *ASM Handbook Vol. 3. Alloy Phase Diagrams* (ASM International, USA, 1992).

[8]   G. F. Bastin and G. D. Rieck, Metall. Trans. **5**, 1817 (1974).

[9]   G. F. Bastin and R. G. D, Metall. Trans. **5**, 1827 (1974).

[10]   M. Mâaza, C. Sella, J. P. Ambroise, M. Kâabouchi, M. Milôche, F. Wehling, and M. Groos, J. Appl. Crystallogr. **26**, 334 (1993).

[11]   C. Herzig, Y. Mishin, and S. Divinski, Metall. Mater. Trans. A **33A**, 765 (2002).

[12]   R. A. German, *Powder Metallurgy and Particulate Materials Processing: The Process, Materials, Products, Properties and Applications* (Metal Powder Industries Federation, 2005).

[13]   Y. Sekiguchi, K. Funami, H. Funakubo, and Y. Suzuki, J. Phys. Colloq. **43**, C4 (1982).

[14]   E. Schüller, O. A. Hamed, M. Bram, D. Sebold, H. P. Buchkremer, and D. Stöver, Adv. Eng. Mater. **5**, 918 (2003).

[15]   B. Tian, Y. X. Tong, F. Chen, Y. Liu, and Y. F. Zheng, J. Alloys Compd. **477**, 576 (2009).

[16]   H. Kato, T. Koyari, M. Tokizane, and S. Miura, Acta Metall. Mater. **42**, 1351 (1994).

[17]   W. A. Johnson, J. A. Domingue, S. H. Reichman, and F. E. Sczerzenie, J. Phys. Colloq. **43**, C4 (1982).

[18] W. A. Johnson, J. A. Domingue, and S. H. Reichman, J. Phys. Colloq. **43**, C4 (1982).

[19] D. G. Morris and M. A. Morris, Mater. Sci. Eng. A **110**, 139 (1989).

[20] N. Zhang, P. B. Khosrovabadi, J. H. Lindenhovius, and B. H. Kolster, Mater. Sci. Eng. A **150**, 263 (1992).

[21] J. C. Hey and A. P. Jardine, Mater. Sci. Eng. A **188**, 291 (1994).

[22] M. D. McNeese, D. C. Lagoudas, and T. C. Pollock, Mater. Sci. Eng. A **280**, 334 (2000).

[23] M. Bram, A. Ahmad-Khanlou, A. Heckmann, B. Fuchs, H. P. Buchkremer, and D. Stöver, Mater. Sci. Eng. A **337**, 254 (2002).

[24] E. Schüller, M. Bram, H. Buchkremer, and D. Stöver, Mater. Sci. Eng. A **378**, 165 (2004).

[25] B. Bertheville, M. Neudenberger, and J.-E. Bidaux, Mater. Sci. Eng. A **384**, 143 (2004).

[26] B. Bertheville and J.-E. Bidaux, J. Alloys Compd. **387**, 211 (2005).

[27] B. Yuan, C. Y. Chung, and M. Zhu, Mater. Sci. Eng. A **382**, 181 (2004).

[28] L. Krone, E. Schüller, M. Bram, O. Hamed, H.-P. Buchkremer, and D. Stöver, Mater. Sci. Eng. A **378**, 185 (2004).

[29] J. Mentz, M. Bram, H. P. Buchkremer, and D. Stöver, Adv. Eng. Mater. **8**, 247 (2006).

[30] J. Mentz, J. Frenzel, M. F.-X. Wagner, K. Neuking, G. Eggeler, H. P. Buchkremer, and D. Stöver, Mater. Sci. Eng. A **491**, 270 (2008).

[31] J. Mentz, M. Bram, H. P. Buchkremer, and D. Stöver, Mater. Sci. Eng. A **481-482**, 630 (2008).

[32] M. Whitney, S. F. Corbin, and R. B. Gorbet, Acta Mater. **56**, 559 (2008).

[33] M. Whitney, S. F. Corbin, and R. B. Gorbet, Intermetallics **17**, 894 (2009).

[34] S. F. Corbin and D. Cluff, J. Alloys Compd. **487**, 179 (2009).

[35] D. Cluff and S. F. Corbin, Intermetallics **18**, 1480 (2010).

[36] J. Butler, P. Tiernan, A. A. Gandhi, K. McNamara, and S. A. M. Tofail, J. Mater. Eng. Perform. **20**, 757 (2011).

[37] F.-C. Yen and K.-S. Hwang, Mater. Sci. Eng. A **528**, 5296 (2011).

[38] A. Bansiddhi and D. C. Dunand, J. Mater. Eng. Perform. **20**, 511 (2011).

[39] M. H. Ismail, R. Goodall, H. A. Davies, and I. Todd, Mater. Lett. **70**, 142 (2012).

[40] M. Lucaci, M. Valeanu, R. L. Orban, V. Tsakiris, D. C. Cirstea, and L. Leonat, Mater. Sci. Forum **672**, 99 (2011).

[41] V. Cândea, G. Arghir, C. Popa, I. Gligor, A. Popa, and G. Batin, Mater. Sci. Forum **672**, 125 (2011).

[42] L. Krone, J. Mentz, M. Bram, H.-P. Buchkremer, D. Stöver, M. Wagner, G. Eggeler, D. Christ, S. Reese, D. Bogdanski, M. Köller, S. A. Esenwein, G. Muhr, O. Prymak, and M. Epple, Adv. Eng. Mater. **7**, 613 (2005).

[43] W. Rostoker, Trans. Am. Institue Min. Metall. Eng. J. Met. **203**, 113 (1955).

[44] C. Zanotti, P. Giuliani, P. Bassani, Z. Zhang, and a. Chrysanthou, Intermetallics **18**, 14 (2010).

[45] B. Yuan, X. P. Zhang, C. Y. Chung, and M. Zhu, Mater. Sci. Eng. A **438-440**, 585 (2006).

[46] A. Biswas, Acta Mater. **53**, 1415 (2005).

[47] B. Bertheville and J.-E. Bidaux, Scr. Mater. **52**, 507 (2005).

[48] B. Bertheville, Mater. Trans. **47**, 698 (2006).

[49] G. Majkic, N. Chennoufi, Y. C. Chen, and K. Salama, Metall. Mater. Trans. A **38A**, 2523 (2007).

[50] P. Novák, A. Školáková, D. Pignol, F. Průša, P. Salvetr, T. F. Kubatík, L. Perriere, and M. Karlík, Mater. Chem. Phys. **181**, 295 (2016).

[51] P. Novák, H. Moravec, P. Salvetr, F. Průša, J. Drahokoupil, J. Kopeček, M. Karlík, and T. F. Kubatík, Mater. Sci. Technol. **31**, 1886 (2015).

[52] C. Yang, Q. R. Cheng, L. H. Liu, Y. H. Li, and Y. Y. Li, Intermetallics **56**, 37 (2015).

[53] C. D. Cirstea, M. Lungu, A. M. Balagurov, V. Marinescu, O. Culicov, G. Sbarcea, and V. Cirstea, Adv. Eng. Forum **13**, 83 (2015).

[54] L. L. Ye, Z. G. Liu, K. Raviprasad, M. X. Quan, M. Umemoto, and Z. Q. Hu, Mater. Sci. Eng. A **241**, 290 (1998).

[55] Y. Zhao, M. Taya, Y. Kang, and A. Kawasaki, Acta Mater. **53**, 337 (2005).

[56] C. Shearwood, Y. Q. Fu, L. Yu, and K. A. Khor, Scr. Mater. **52**, 455 (2005).

[57] K. Huang, Y. Qin, J. Zhao, M. Bin Zulkipli, and H. Hijji, MATEC Web Conf. **21**, (2015).

[58] M. H. Ismail, R. Goodall, H. a. Davies, and I. Todd, Mater. Sci. Eng. C **32**, 1480 (2012).

[59] J. Frenzel, E. P. George, a. Dlouhy, C. Somsen, M. F.-X. Wagner, and G. Eggeler, Acta Mater. **58**, 3444 (2010).

[60] G. Chen, K.-D. Liss, and P. Cao, Metall. Mater. Trans. A **46**, 5887 (2015).

[61] G. Chen, K.-D. Liss, and P. Cao, Acta Mater. **67**, 32 (2014).

[62] G. Chen, K.-D. Liss, and P. Cao, Metals (Basel). **5**, 530 (2015).

[63] M. E. Brown, *Introduction to Thermal Analysis: Techniques and Application*, 2nd ed. (Kluwer Academic Publishers, NY, NY, 2004).

[64] J. Tyber, J. McCormick, K. Gall, R. DesRoches, H. J. Maier, and A. E. Abdel Maksoud, J. Eng. Mech. **133**, 1009 (2007).

[65] G. M. Swallowe, P. Sittner, and M. R. Daymond, IEEE Trans. Nucl. Sci. **52**, 326 (2005).

[66] J. A. Shaw, C. B. Churchill, and M. A. Iadicola, Exp. Tech. **32**, 55 (2008).

[67] J. Laeng, Z. Xiu, X. Xu, X. Sun, H. Ru, and Y. Liu, Phys. Scr. **T129**, 250 (2007).

[68] W. Tang, R. Sandström, Z. G. Wei, and S. Miyazaki, Metall. Mater. Trans. A **31A**, 2423 (2000).

[69] C. L. Chu, C. Y. Chung, and P. H. Lin, Mater. Sci. Eng. A **392**, 106 (2005).

[70] C. L. Chu, C. Y. Chung, and P. H. Lin, J. Mater. Sci. **40**, 4959 (2005).

[71] O. Bojda, G. Eggeler, and A. Dlouhý, Scr. Mater. **53**, 99 (2005).

[72] C. L. Chu, P. H. Lin, and C. Y. Chung, J. Mater. Sci. **40**, 773 (2005).

[73] C. L. Chu, C. Y. Chung, and P. H. Lin, Mater. Lett. **59**, 404 (2005).

[74] G. Ji, Z. Zhang, Y. Liu, X. Ding, J. Sun, and X. Ren, J. Alloys Compd. **448**, 171 (2008).

[75] T. Goryczka and J. Van Humbeeck, J. Alloys Compd. **456**, 194 (2008).

[76] C. Grossmann, J. Frenzel, V. Sampath, T. Depka, and G. Eggeler, Metall. Mater. Trans. A **40A**, 2530 (2009).

[77] C. Chu, J.-C. Chung, and P.-K. Chu, Trans. Nonferrous Met. Soc. China **16**, 49 (2006).

[78] B. Y. Li, L. J. Rong, Y. Y. Li, and V. E. Gjunter, Acta Mater. **48**, 3895 (2000).

[79] G. K. Dey, Acta Mater. **51**, 2549 (2003).

[80] C. L. Yeh and W. Y. Sung, J. Alloys Compd. **376**, 79 (2004).

[81] D. Halliday, R. Resnick, and J. Walker, *Fundamentals of Physics Extended* (John Wiley and Sons, 2010).

[82] B. D. Cullity, *Elements of X-Ray Diffraction*, 2nd ed. (Addison-Wesley Pub. Co., 1978).

[83] J. Dahn and J. O'Brien, *PHC6250 Class Notes* (Dalhousie University, Nova Scotia, 2011).

[84] M. A. White, *Properties of Materials* (Oxford University Press, 1999).

[85] D. Turriff, A Study in the Process Kinetics of TLP Sintering in a Binary-Isomorphous Alloy System, University of Waterloo, 2007.

[86] H. M. Rietveld, J. Appl. Crystallogr. **2**, 65 (1969).

[87] R. J. Hill, J. Appl. Crystallogr. **25**, 589 (1992).

[88] D. L. Bish and S. A. Howard, J. Appl. Crystallogr. **21**, 86 (1988).

[89] A. C. Larson and R. B. Von Dreele, Los Alamos Natl. Lab. Rep. **LAUR 86-74**, (2004).

[90] I. Swainson, in *11th Int. Neutron Scatt. Summer Sch.* (Chalk River, Ontario, 2011).

[91] B. H. Toby, Powder Diffr. **21**, 67 (2006).

[92] L. B. McCusker, R. B. Von Dreele, D. E. Cox, D. Louër, and P. Scardi, J. Appl. Crystallogr. **32**, 36 (1999).

[93] R. J. Hill and L. M. D. Cranswick, J. Appl. Crystallogr. **27**, 802 (1994).

[94] I. C. Madsen, N. V. Y. Scarlett, L. M. D. Cranswick, and T. Lwin, J. Appl. Crystallogr. **34**, 409 (2001).

[95] D. L. Bish and J. E. Post, editors , *Modern Powder Diffraction, Reviews in Minerology Vol. 20* (Mineralogical Society of America, 1989).

[96]   R. A. Young, editor , *The Rietveld Method* (Oxford University Press, 1995).

[97]   N. V. Y. Scarlett, I. C. Madsen, L. M. D. Cranswick, T. Lwin, E. Groleau, G. Stephenson, M. Aylmore, and N. Agron-Olshina, J. Appl. Crystallogr. **34**, 383 (2002).

[98]   T. M. Holden, in *11th Int. Neutron Scatt. Summer Sch.* (Chalk River, Ontario, 2011).

[99]   G. E. Bacon, *Neutron Diffraction* (Clarendon Press, Oxford, 1975).

[100] K. Momma and F. Izumi, J. Appl. Crystallogr. **44**, 1272 (2011).

[101] F. Izumi and K. Momma, Solid State Phenom. **130**, 15 (2007).

[102] M. H. Mueller and H. W. Knott, Trans. Metall. Soc. AIME **227**, 674 (1963).

[103] A. Takeuchi, K. Yubuta, and A. Inoue, J. Phys. Conf. Ser. **144**, 012045 (2009).

[104] E. Wu, E. H. Kisi, S. J. Kennedy, and A. J. Studer, J. Am. Ceram. Soc. **8884**, 2281 (2001).

[105] E. Wu, E. H. Kisi, D. P. Riley, R. I. Smith, I. Facility, and U. Kingdom, Society **86**, 3084 (2002).

[106] E. Wu and E. H. Kisi, J. Am. Ceram. Soc. **89**, 710 (2006).

[107] D. P. Riley, C. P. Oliver, and E. H. Kisi, Intermetallics **14**, 33 (2006).

[108] R. E. Whitfield, D. J. Goossens, and A. J. Studer, J. Phys. Conf. Ser. **251**, 012048 (2010).

[109] W. Kasprzak, D. Sediako, M. Walker, M. Sahoo, and I. Swainson, Metall. Mater. Trans. A **42A**, 1854 (2011).

[110] D. Cluff, M. Gharghouri, and S. Corbin, in *Proc. 2014 World Congr. Powder Metall. Part. Mater.* (2014).

[111] ASTM Standard B703-10, 10 (2012).

[112] D. Cluff and S. Corbin, in *Proc. 2013 Int. Conf. Powder Metall. Part. Mater.* (MPIF, Chicago, Il, 2013).

[113] A. Qiu, L. Liu, W. Pang, X. Lu, and C. Li, Trans. Nonferrous Met. Soc. China **21**, 1808 (2011).

[114] G. Chattopadhyay and H. Kleykamp, Zeitschrift Für Met. **74**, 182 (1983).

[115] O. Yamamoto, K. Alvarez, T. Kikuchi, and M. Fukuda, Acta Biomater. **5**, 3605 (2009).

[116] S. Malinov, W. Sha, and C. S. Voon, J. Microsc. **207**, 163 (2002).

[117] R. A. Perez, H. Nakajima, and F. Dyment, Mater. Trans. **44**, 2 (2003).

[118] R. W. G. Wyckoff, *Crystal Structures Volume 1*, 2nd Editio (John Wiley and Sons, New York, NY, USA, 1963).

[119] G. A. Yurko, J. W. Barton, and J. Gordon Parr, Acta Crystallogr. **12**, 909 (1959).

[120] ICDD, in edited by S. Kabekkodu (International Centre for Diffraction Data, Newton Square, Pa, USA, 2015).

[121] L.-M. Peng, G. Ren, S. L. Dudarev, and M. J. Whelan, Acta Crystallogr. Sect. A **A52**, 456 (1996).

[122] B. H. Toby, J. Appl. Crystallogr. **34**, 210 (2001).

[123] V. F. Sears, Neutron News **3**, 26 (1992).

[124] T. B. Massalski, H. Okamoto, P. R. Subramanian, and L. Kacprzak, editors , *ASM Handbook. Vol. 3: Alloy Phase Diagrams*, 3rd ed. (ASM International, Materials Park, OH, 1992).

[125] A. Pasturel, C. Colinet, D. Nguyen Manh, A. T. Paxton, and M. Van Schilfgaarde, Phys. Rev. B **52**, 15176 (1995).

[126] D. Cluff, M. A. Gharghouri, and S. F. Corbin, Intermetallics (n.d.).

[127] F. Dyment and C. M. Libanati, J. Mater. Sci. **3**, 349 (1968).

[128] B. Peplinski, D. M. Többens, W. Kockelmann, and R. M. Ibberson, Z. Krist. Suppl. **23**, 21 (2006).

[129] Y. S. Touloukian, R. K. Kirby, R. E. Taylor, and P. D. Desai, *Thermophysical Properties of Matter Vol. 12. Thermal Expansion: Metallic Elements and Alloys* (IFI-Plenum, New York, NY, 1975).

[130] H. T. Clark Jr, Met. Trans. **185**, 588 (1949).

[131] J. Spreadborough and J. W. Christian, Proc. Phys. Soc. **74**, 609 (1959).

[132] O. N. Senkov, B. C. Chakoumakos, J. J. Jonas, and F. H. Froes, Mater. Res. Bull. **36**, 1431 (2001).

[133] E. S. Bumps and H. D. Kessler, Trans. Am. Soc. Met. **45**, 1008 (1953).

[134] B. Kohlhass, P. Dünner, and N. Schmitz-Pranghe, Zeitschrift Für Angew. Phys. **23**, 245 (1967).

[135] T. Wang, J. Zhu, R. A. Mackay, L. Chen, and Z.-K. Liu, Metall. Mater. Trans. A **35**, 2313 (2004).

[136] P. Duwez and J. L. Taylor, Trans. AIME **188**, 1173 (1950).

[137] M. H. Mueller and H. W. Knott, Trans. Metall. Soc. AIME **227**, 674 (1963).

[138] W. Rostoker, Trans. AIME **194**, 209 (1952).

[139] J. Khalil Allafi, W. W. Schmahl, M. Wagner, H. Sitepu, D. M. Toebbens, and G. Eggeler, Mater. Sci. Eng. A **378**, 161 (2004).

[140] J. L. Glimois, P. Forey, R. Guillen, and J. L. Feron, J. Less Common- Met. **134**, 221 (1987).

[141] D. M. Poole and W. Hume-Rothery, J. Inst. Met. **83**, 473 (1954).

APPENDIX A
LATTICE PARAMETER
DATA

α-Ti

Temperature (°C)	a (Å)	s.u.	c (Å)	s.u.	Temperature (°C)	a (Å)	s.u.	c (Å)	s.u.
El Ni/El Ti					*95 Ti/5 Ni*				
38	2.9576	0.0005	4.693	0.001	26	2.9541	0.0003	4.6906	0.0007
504	2.9726	0.0003	4.717	0.001	505	2.9692	0.0003	4.7135	0.0005
518	2.9723	0.0004	4.719	0.001	519	2.9697	0.0005	4.713	0.001
534	2.9734	0.0005	4.717	0.001	539	2.9704	0.0005	4.714	0.001
551	2.9732	0.0005	4.718	0.001	561	2.9708	0.0005	4.717	0.001
568	2.9736	0.0005	4.722	0.001	583	2.9715	0.0005	4.719	0.001
586	2.9745	0.0005	4.720	0.001	605	2.9719	0.0005	4.719	0.001
603	2.9740	0.0005	4.720	0.001	626	2.9717	0.0005	4.720	0.001
620	2.9753	0.0005	4.723	0.001	648	2.9735	0.0005	4.722	0.001
636	2.9751	0.0005	4.725	0.001	670	2.9737	0.0005	4.723	0.001
653	2.9750	0.0005	4.727	0.001	691	2.9732	0.0006	4.723	0.001
669	2.9761	0.0005	4.726	0.001	711	2.9739	0.0005	4.726	0.001
686	2.9769	0.0005	4.728	0.001	732	2.9744	0.0006	4.727	0.001
702	2.9772	0.0006	4.727	0.002	753	2.9741	0.0006	4.727	0.001
719	2.9769	0.0005	4.730	0.001					
735	2.9780	0.0005	4.732	0.001					
752	2.9780	0.0005	4.732	0.001					
769	2.9782	0.0005	4.734	0.001					
785	2.9794	0.0005	4.735	0.001					
801	2.9792	0.0005	4.736	0.001					
817	2.9797	0.0006	4.738	0.002					
833	2.9802	0.0006	4.741	0.001					
849	2.9806	0.0005	4.741	0.001					
864	2.9812	0.0003	4.742	0.001					
871	2.9811	0.0007	4.741	0.002					
878	2.9818	0.0007	4.742	0.002					
886	2.9822	0.0007	4.743	0.002					
894	2.9818	0.0009	4.745	0.002					
902	2.9805	0.0006	4.750	0.001					
903	2.9822	0.0004	4.746	0.001					
909	2.9843	0.0007	4.743	0.002					
917	2.9837	0.0007	4.744	0.002					
924	2.981	0.001	4.766	0.002					

β-Ti		
El Ni/El Ti		
Temperature (°C)	a (Å)	s.u.
890	3.316	0.002
898	3.317	0.001
906	3.3172	0.0007
914	3.3175	0.0006
922	3.3186	0.0005
938	3.3204	0.0004
954	3.3212	0.0004
958	3.3194	0.0003
969	3.3214	0.0004
974	3.3198	0.0002
985	3.3217	0.0005
989	3.3211	0.0004
1000	3.3221	0.0005

β-Ti(Ni)		
95 Ti/5 Ni		
Temperature (°C)	a (Å)	s.u.
739	3.269	0.001
756	3.2693	0.0007
759	3.270	0.001
766	3.2707	0.0005
775	3.2745	0.0009
785	3.2756	0.0005
790	3.277	0.001
798	3.278	0.001
805	3.2797	0.0004
805	3.2785	0.0004
814	3.285	0.001
819	3.280	0.001
833	3.2874	0.0008
838	3.285	0.0010
853	3.290	0.001
857	3.2890	0.0009
873	3.288	0.001
877	3.289	0.001
893	3.289	0.001
897	3.289	0.001
913	3.292	0.001
919	3.289	0.001
933	3.2911	0.0009
940	3.289	0.001
953	3.292	0.001
961	3.292	0.001
973	3.290	0.001
981	3.291	0.001
988	3.294	0.001
1000	3.2939	0.0004

Ni		
El Ni/El Ti		
Temperature (°C)	a (Å)	s.u.
38	3.5304	0.0002
504	3.5547	0.0001
518	3.5558	0.0002
534	3.5566	0.0001
551	3.5576	0.0001
568	3.5590	0.0002
586	3.5598	0.0002
603	3.5609	0.0002
620	3.5623	0.0002
636	3.5633	0.0002
653	3.5641	0.0002
669	3.5657	0.0002
686	3.5667	0.0002
702	3.5678	0.0002
719	3.5688	0.0002
735	3.5701	0.0002
752	3.5711	0.0002
769	3.5724	0.0002
785	3.5737	0.0002
801	3.5743	0.0002
817	3.5753	0.0002
833	3.5766	0.0002
849	3.5775	0.0002
864	3.5791	0.0001
871	3.5791	0.0002
878	3.5793	0.0002
886	3.5800	0.0002
894	3.5805	0.0002
903	3.5817	0.0001
909	3.5820	0.0002
958	3.5848	0.0002
974	3.5860	0.0002
989	3.5872	0.0002
1000	3.5882	0.0002

	Ti$_2$Ni			NiTi				
	Ti$_2$Ni/Ni$_3$Ti			*LP mixture (RS1200)*			*HP mixture (RS1200)*	
Temperature (°C)	a (Å)	s.u.	Temperature (°C)	a (Å)	s.u.	Temperature (°C)	a (Å)	s.u.
32	11.3409	0.0007	1199	3.0623	0.0002	1198	3.0647	0.0002
195	11.3564	0.0008	1181	3.0624	0.0003	1178	3.0641	0.0003
211	11.3575	0.0007	1152	3.0614	0.0003	1153	3.0629	0.0003
232	11.3591	0.0008	1127	3.0597	0.0003	1128	3.0617	0.0003
251	11.3624	0.0008	1102	3.0590	0.0003	1103	3.0604	0.0003
268	11.3632	0.0008	1077	3.0578	0.0003	1078	3.0601	0.0003
289	11.365	0.001	1052	3.0568	0.0003	1053	3.0588	0.0003
308	11.368	0.001	1027	3.0561	0.0003	1028	3.0571	0.0003
322	11.370	0.001	1001	3.0548	0.0003	1003	3.0567	0.0003
343	11.372	0.001	976	3.0538	0.0003	978	3.0550	0.0003
361	11.376	0.001	951	3.0522	0.0003	953	3.0541	0.0003
396	11.379	0.001	926	3.0523	0.0003	928	3.0536	0.0003
414	11.381	0.001	901	3.0512	0.0003	903	3.0526	0.0003
431	11.385	0.001	876	3.0497	0.0003	878	3.0512	0.0003
448	11.385	0.001	851	3.0491	0.0003	853	3.0506	0.0003
466	11.388	0.001	826	3.0478	0.0003	828	3.0492	0.0003
483	11.390	0.001	801	3.0470	0.0003	803	3.0483	0.0003
501	11.391	0.001	776	3.0461	0.0003	779	3.0472	0.0003
518	11.394	0.001	751	3.0455	0.0003	754	3.0462	0.0003
536	11.397	0.001	726	3.0444	0.0002	729	3.0458	0.0003
553	11.400	0.001	702	3.0435	0.0002	705	3.0446	0.0003
570	11.400	0.001	678	3.0425	0.0002	680	3.0436	0.0002
587	11.404	0.001	653	3.0417	0.0002	657	3.0426	0.0003
604	11.405	0.001	629	3.0406	0.0002	633	3.0416	0.0002
621	11.406	0.001	605	3.0399	0.0002	608	3.0413	0.0003
638	11.410	0.001	581	3.0389	0.0002	585	3.0404	0.0002
654	11.411	0.001	558	3.0382	0.0002	562	3.0396	0.0002
671	11.415	0.001	538	3.0374	0.0002	540	3.0388	0.0002
688	11.417	0.001	519	3.0369	0.0002	520	3.0380	0.0002
705	11.418	0.001	501	3.0358	0.0002	503	3.0368	0.0002
721	11.422	0.001	485	3.0354	0.0002	486	3.0366	0.0002
738	11.424	0.001	471	3.0348	0.0002	471	3.0358	0.0002
754	11.426	0.001	457	3.0337	0.0002	458	3.0347	0.0002
770	11.429	0.001	433	3.0332	0.0002	433	3.0345	0.0002
787	11.430	0.001	411	3.0325	0.0002	411	3.0336	0.0002
803	11.433	0.001	392	3.0316	0.0002	391	3.0326	0.0002
820	11.435	0.001	375	3.0310	0.0002	374	3.0319	0.0002
836	11.438	0.001	359	3.0304	0.0002	358	3.0320	0.0002
852	11.437	0.001	338	3.0297	0.0001	337	3.0312	0.0002
869	11.442	0.001	319	3.0290	0.0001	318	3.0301	0.0002
885	11.442	0.001	303	3.0283	0.0001	301	3.0294	0.0002
902	11.446	0.001	283	3.0276	0.0001	281	3.0289	0.0001
918	11.448	0.001	265	3.0271	0.0001	263	3.0283	0.0001
934	11.450	0.001	246	3.0264	0.0001	246	3.0275	0.0001
			225	3.0256	0.0001	228	3.0266	0.0001
			207	3.0248	0.0001	209	3.0258	0.0001
			192	3.0243	0.0001	187	3.0251	0.0001
			174	3.0237	0.0001	167	3.0246	0.0001
			154	3.0230	0.0001	149	3.0239	0.0001
			134	3.0223	0.0001	129	3.0233	0.0001
			114	3.0216	0.0001	123	3.0228	0.0001
			112	3.0213	0.0001	118	3.0227	0.0001

NiTi (continued)

LP mixture (RS1200)			HP mixture (RS1200)		
Temperature (°C)	a (Å)	s.u.	Temperature (°C)	a (Å)	s.u.
112	3.0213	0.0001	118	3.0227	0.0001
109	3.0212	0.0001	113	3.0226	0.0001
106	3.0212	0.0001	108	3.0223	0.0001
103	3.0209	0.0001	103	3.0222	0.0001
100	3.0209	0.0001	98	3.0220	0.0001
97	3.0208	0.0001	93	3.0217	0.0001
94	3.0206	0.0001	88	3.0213	0.0001
91	3.0206	0.0001	85	3.0213	0.0001
88	3.0205	0.0001	82	3.0212	0.0001
85	3.0203	0.0001	79	3.0215	0.0002
82	3.0201	0.0001	76	3.0209	0.0002
79	3.0202	0.0001	73	3.0204	0.0003
76	3.0200	0.0001	70	3.0189	0.0002
73	3.0199	0.0001			
70	3.0197	0.0001			
67	3.0196	0.0001			
64	3.0194	0.0001			
61	3.0192	0.0001			
58	3.0191	0.0001			
55	3.0188	0.0001			
52	3.0188	0.0001			
49	3.0185	0.0001			
46	3.0185	0.0001			
43	3.0182	0.0001			
40	3.0181	0.0001			
37	3.0177	0.0002			
34	3.0173	0.0002			
31	3.0172	0.0002			
28	3.0165	0.0002			
25	3.0163	0.0002			
22	3.0158	0.0002			

Ni$_3$Ti

Temperature (°C)	a (Å)	s.u.	c (Å)	s.u.
Ti$_2$Ni/Ni$_3$Ti				
32	5.1143	0.0003	8.3378	0.0008
195	5.1227	0.0004	8.3523	0.0008
211	5.1232	0.0003	8.3526	0.0008
232	5.1243	0.0004	8.3540	0.0009
251	5.1253	0.0004	8.3579	0.0008
268	5.1262	0.0004	8.3596	0.0009
289	5.1271	0.0004	8.360	0.001
308	5.1285	0.0004	8.364	0.001
322	5.1299	0.0004	8.366	0.001
343	5.1308	0.0004	8.367	0.001
361	5.1326	0.0004	8.369	0.001
396	5.1343	0.0004	8.373	0.001
414	5.1352	0.0004	8.376	0.001
431	5.1365	0.0004	8.380	0.001
448	5.1373	0.0004	8.381	0.001
466	5.1388	0.0004	8.382	0.001
483	5.1396	0.0004	8.385	0.001
501	5.1404	0.0004	8.386	0.001
518	5.1423	0.0004	8.387	0.001
536	5.1431	0.0004	8.390	0.001
553	5.1445	0.0004	8.393	0.001
570	5.1452	0.0004	8.394	0.001
587	5.1461	0.0004	8.399	0.001
604	5.1474	0.0004	8.401	0.001
621	5.1482	0.0004	8.401	0.001
638	5.1494	0.0004	8.404	0.001
654	5.1500	0.0004	8.406	0.001
671	5.1517	0.0004	8.408	0.001
688	5.1527	0.0004	8.411	0.001
705	5.1532	0.0004	8.413	0.001
721	5.1555	0.0004	8.416	0.001
738	5.1560	0.0004	8.418	0.001
754	5.1571	0.0004	8.421	0.001
770	5.1582	0.0004	8.423	0.001
787	5.1595	0.0004	8.425	0.001
803	5.1602	0.0004	8.427	0.001
820	5.1611	0.0004	8.429	0.001
836	5.1627	0.0004	8.434	0.001
852	5.1631	0.0004	8.434	0.001
869	5.1648	0.0004	8.437	0.001
885	5.1653	0.0005	8.439	0.001
902	5.1671	0.0004	8.440	0.001
918	5.1679	0.0004	8.442	0.001
934	5.1690	0.0004	8.445	0.001